ZIF-67-based catalysts in persulfate advanced oxidation processes (PS-AOPs) for water remediation

Xiu-Wu Zhang [a,b], Ming-Yan Lan [a,b], Fei Wang [a,b], Xiao-Hong Yi [a,b], Chong-Chen Wang [a,b,*]

[a] Beijing Key Laboratory of Functional Materials for Building Structure and Environment Remediation, Beijing University of Civil Engineering and Architecture, Beijing 100044, China
[b] Beijing Energy Conservation & Sustainable Urban and Rural Development Provincial and Ministry Co-construction Collaboration Innovation Center, Beijing University of Civil Engineering and Architecture, Beijing 100044, China

ARTICLE INFO

ABSTRACT

Zeolitic imidazolate framework-67 (ZIF-67), which consists of metal ions Co^{2+} and 2-methylimidazole ligand, is a kind of typical MOF material. As an emerging multifunctional material, ZIF-67-based materials have attracted increasing interest in the synthesis and applications due to their exceptionally high surface area, tunable porosity, and excellent thermal & chemical stability. In this paper, we focus on its developments in the field of persulfate advanced oxidation processes (PS-AOPs) for water purification. This review summarizes the latest enhanced strategies of ZIF-67-based catalysts for PS-AOPs, like the construction of immobilized ZIF-67, the functional group combination, metal ion doping, and calcination or sulfuration to produce corresponding derivatives. Finally, we attempt to provide the mechanistic insight for the applications of ZIF-67-based materials in organic wastewater treatment by PS-AOPs and to present the future direction for the application in PS-AOPs of ZIF-67-based materials.

1. Introduction

With the continuous development of the economy and industrialization, water pollution and water environment safety have become urgent problems for human beings [1,2]. Most of the organic pollutants like organic dyes, pharmaceuticals and personal care products (PPCPs), and pesticides are difficult to biodegrade due to their high stability [3,4]. To date, various technologies including but not limited to adsorption [5,6], coagulation [7,8], and catalysis [9] have been applied to achieve wastewater remediation. Among all technologies, advanced oxidation processes (AOPs) like photocatalysis [10], Fenton and Fenton-like oxidation [11,12], ozone oxidation [13,14] electrocatalysis [15,16] and persulfate -based advanced oxidation processes (PS-AOPs) [17,18] can generate a large number of reactive oxidized species (ROSs) to decompose the highly toxic organic pollutants into lowly toxic or innocuous small molecule compounds (e.g. CO_2 and H_2O), which are believed as promising water treatment processes.

Among all the above-mentioned AOPs, PS-AOPs have received extensive research and attention in recent years because of the some merits: (i) Sulfate radical ($SO_4^{\bullet-}$), hydroxyl radical ($\bullet OH$), superoxide anion radical ($\bullet O_2^-$) as well as nonradical ROS can be produced via energy-transfer or reductive electron-transfer processes [19]. (ii) The primarily generated $SO_4^{\bullet-}$ possesses a higher redox potential ($E^0 =$ 2.6–3.1 V) versus other ROSs ($\bullet OH$, $\bullet O_2^-$ and $^1O_2$), a wider pH working range and longer half-life (30–40 μs) [20]. (iii) Both peroxydisulfate (PDS) and peroxymonosulfate (PMS) can be activated in a variety of methods like transition metals catalysts [21], radiation, heat, alkaline, sonication, carbonaceous materials [22] and photocatalysis [23]. Several review papers outlined a series of functional catalytic materials for the activation of PDS/PMS, in which the transition metals materials including Co^{2+}, Fe^{2+}, Cu^{2+}, Ni^{2+}, Co_3O_4, Fe_3O_4, and Mn_3O_4 were widely selected as effective catalysts [24,25]. Among them, Co species especially Co^{2+} and $Co(OH)^+$ are thermodynamically easier to bind to HSO_5^- with lower Gibbs free energy values [26]. Therefore, cobalt-based materials are considered to be the most effective catalysts [26–28].

Metal-organic frameworks (MOFs), as an emerging organic-inorganic hybrid material, have exhibited great potential in many fields like adsorption [29], gas storage [30], catalysis [31], drug delivery [32,33], and sensors [34–36], considering their ultra-high surface area, tunable porosity and multiple active sites. Zeolite-like imidazole

skeleton materials (ZIFs) are a kind of MOFs with zeolite skeleton structure, which are constructed from Zn or Co as metal source and imidazole or imidazole derivatives as organic ligands [37]. ZIF-67 with sodalite topology was reported by Yaghi et al. in 2008 for the first time [38], which consisted of 2-methylimidazole (2-MIM) as the ligand and cobalt as the metal center [39]. ZIF-67 has demonstrated excellent performances in catalysis [40], separation [41], adsorption [42], and carbon capture [38]. In recent years, the applications of ZIF-67-based materials have attracted the attention of many researchers in the fields of environment and energy [43,44].

In recent years, ZIF-67-based catalysts have been extensively investigated in PS-AOPs [45–48]. The advantages of ZIF-67-based catalysts for PS-AOPs reactions mainly include the following items. (i) The abundant bivalent cobalt species are uniformly dispersed in ZIF-67 [49], which is effective for activating PDS or PMS. (ii) There are many functional groups on the surface of ZIF-67, which facilitate the preparation of immobilized catalysts. (iii) ZIF-67 possessed many unique properties, such as high porosities [50], chemical stability [51] and extraordinary ligand-metal charge transfer [52] to promote the reaction of PS-AOPs. (iv) Combining different functional materials to prepare binary and even multicomponent composites is an effective way to address the disadvantages of the individual ZIF-67, thus achieving the synergistic effect ("1 + 1 > 2") and enhancing the corresponding catalytic performance [10]. (v) The various and diverse derivatives of ZIF-67 might provide unlimited possibilities for ZIF-67-based catalysts to activate persulfate for organic pollutants degradation [37]. The reactions via the central metal (cobalt) and PDS/PMS are mainly based upon the electron transfer between the cobalt ion and the oxidants, and the corresponding activation mechanisms of radical generation reactions are shown in Eqs. (1)–(2). The overall research progress of ZIF-67-based materials was summarized in Tables 2-4. These findings indicated that ZIF-67-based materials have attracted increasing attention from scholars and have enormous potential in the field of PS-AOPs. Hence, it is necessary to present the current research situation of ZIF-67-based material in PS-AOPs and its enhanced strategies.

$$Co^{2+} + S_2O_8^{2-} \rightarrow Co^{3+} + SO_4^{\bullet-} + SO_4^{2-} \qquad (1)$$

$$Co^{2+} + HSO_5^- \rightarrow Co^{3+} + SO_4^{\bullet-} + OH^- \qquad (2)$$
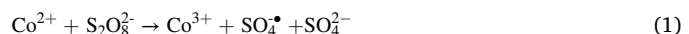
In this review, we highlighted the recent advances of ZIF-67-based materials as heterogeneous catalysts for PDS/PMS activation to degrade different organic pollutants. The primary contents of this review were illustrated in Scheme 1: (i) The advanced progress of immobilized-ZIF-67 for activating PDS/PMS; (ii) The ZIF-67 composites for activation of persulfate to enhance catalytic performance; (iii) Strategies to prepare ZIF-67 derivatives for activation of persulfate. The preparation methods, catalytic mechanism, reusability and stability are also discussed in detail. In conclusion, the prospects of ZIF-67-based materials in PS-AOPs are presented.

2. ZIF-67 based catalysts for PS-AOPs

The synthesis of ZIF-67 by the conventional solvothermal method mainly involves dissolving the reactants including cobalt sources and 2-methylimidazole in solvents like methanol and N, N'-dimethylformamide (DMF). Qian et al. reported a synthesis method to prepare ZIF-67 in pure aqueous solutions at room temperature [51]. In a typical preparation, $Co(NO_3)_2 \cdot 6H_2O$ and 2-methylimidazole were dissolved in deionized water, respectively. Those two solutions were mixed and stirred at room temperature. The purple ZIF-67 precipitates were collected by centrifugation, and finally dried under vacuum. The average particle sizes and nanostructures of ZIF-67 can be modified through adjusting experimental conditions carefully [51]. The as-prepared ZIF-67 possessed some merits like highly stable structure, adjustable pore size and strong catalytic activity [60,61]. Besides traditional solvothermal and hydrothermal methods, other methods like
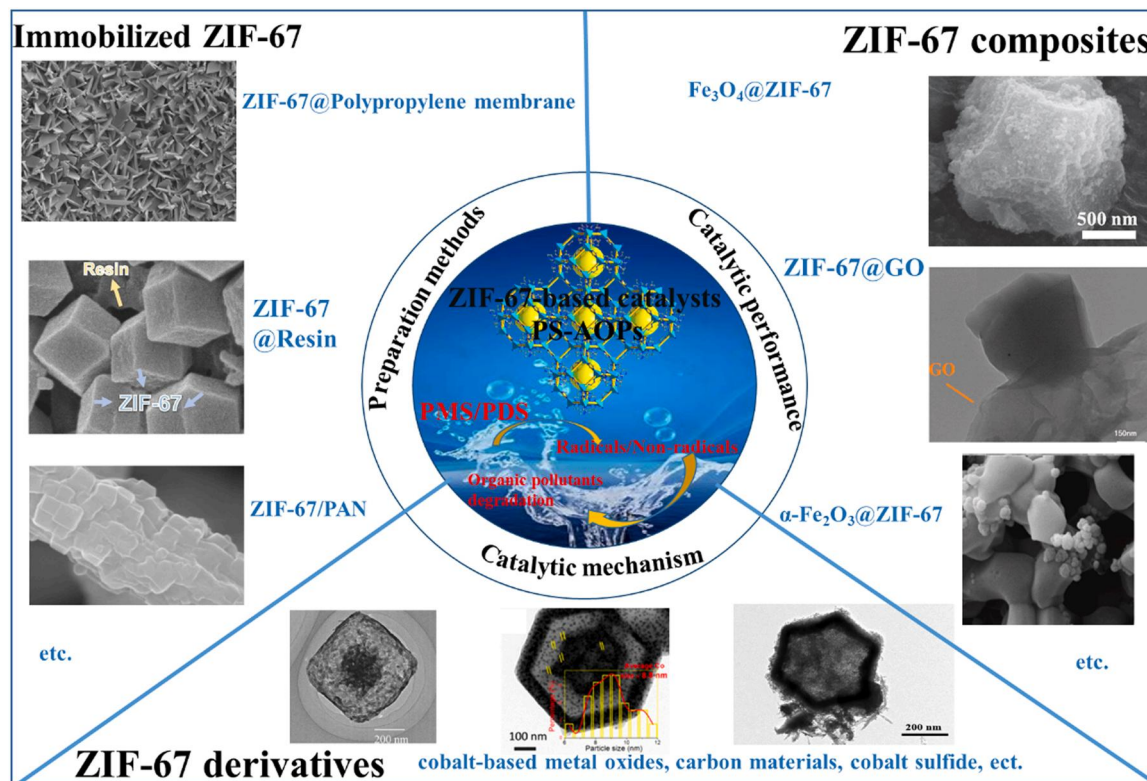
Scheme 1. Schematic diagram of ZIF-67-based materials for PS-AOPs. Reproduced with permission from Ref. [45,47,53–59]. Copyright 2019 Elsevier. Copyright 2018 Elsevier. Copyright 2017 Elsevier. Copyright 2021 Elsevier. Copyright 2021 Elsevier. Copyright 2021 Elsevier. Copyright 2021 Elsevier. Copyright 2020 American Chemical Society. Copyright 2021 Elsevier.

room-temperature synthesis [62], surfactant-assisted method [63], sol-gel method [64], electro-deposition [65], steam-assisted conversion [66], microwave/ultrasonic-assisted method [67,68] have been developed to produce ZIF-67 with different particle sizes and morphologies. The typical synthesis methods for ZIF-67 were demonstrated in Table 1.

Up to now, the powder ZIF-67 displayed good PS activation for organics degradation. However, the further practical applications of ZIF-67 are plagued by its inherent drawbacks like the difficulty to be separated and recycled from suspension after use and limited visible light utilization [47,54,71,72]. Some strategies have been adopted to enhance the PS-AOPs performance of ZIF-67, which can be divided into the construction of immobilized ZIF-67, the preparation of ZIF-67 composites and synthesis of ZIF-67 derivatives. Tables 2–4 listed the preparation methods and performance of three types of ZIF-67-based catalysts for activating PMS/PDS in water remediation.

Lin et al. [73] firstly used ZIF-67 as a heterogeneous catalyst to activate PMS for Rhodamine B (RhB) degradation in simulated wastewater. The RhB degradation induced by PMS activation over ZIF-67 could also be enhanced by increasing ZIF-67 loading, higher temperature, the UV irradiation and ultrasonication. The cobalt ions in ZIF-67 can react with PMS to generate sulfate radicals to attack RhB molecules. Based on the research of Lin et al., studies on the organic pollutants degradation in aqueous solution adopting ZIF-67-based materials as catalysts to activate persulfate have sprung up. Hence, we selected some representative ZIF-67-based catalysts in this review to highlight their preparation methods, characterizations, applications in PS-AOPs and the corresponding reaction mechanisms.

2.1. The construction of immobilized ZIF-67 for PS-AOPs

Different from the homogeneous catalysis, heterogeneous catalysis benefited from preventing secondary contamination by limiting the uncontrolled leach of catalysts to the aqueous solution and the capability to perform under different operational conditions [74]. However, because of the small size of powder catalyst and probable solubility in reaction media, it is not always easy to separate catalysts from the treated solution [75]. To overcome the above-mentioned problems, the catalysts are usually immobilized onto some solid supports [76]. The supports are mostly in the form of oxides without intrinsic catalysis activity like silica aerogels [77], silica spheres [78], hydrotalcite [79], zeolites [80] and alumina membranes [81,82], which are pre-shaped cheap solids with high surface area. Our group synthesized UiO-66-NH$_2$(Zr/Hf) membrane using α-Al$_2$O$_3$ as a substrate [83], which possessed great recyclability and stability to photocatalytically reduce highly toxic Cr(VI) into lowly toxic Cr(III). Inspired by our previous

work, we recently immobilized MIL-101(Fe)-NH$_2$ (MIL: abbreviation of Materials of Institute Lavoisier) on the α-Al$_2$O$_3$ substrate to accomplished continuous Cr(VI) reduction [82] and Fenton-like Norfloxacin degradation performance [84]. As well, we immobilized MIL-88A on cotton fibers [85] and immobilized Fe$_3$O$_4$ derived from MIL-88A on porous block substrate [76] to degrade tetracycline antibiotics. Also, the copper foam (CF) was chosen as substrate to immobilize CoS$_x$-CuS$_x$ derived from ZIF-L(Co)/CF for the sulfonamide degradation [86]. ZIF-67 benefits from the presence of numerous organic functional groups that can be immobilized on a wide range of substrates. Up to now, there are two main approaches to immobilize ZIF-67 on the suitable substrates: post-synthesis immobilization and in-situ immobilization. As displayed in Table 2, several immobilized ZIF-67 catalysts have been developed to boost the recyclability of ZIF-67 in the PS-AOPs activation reaction. The summary diagram of immobilized ZIF-67 and the corresponding substrate microscopic morphology is shown in Fig. 1. Considering the PS-AOPs mechanism of immobilized ZIF-67 is similar to powder ZIF-67, we will focus on the preparation methods, characterizations and applications of immobilized ZIF-67 catalysts for activation of persulfate in this section.

Electrospun polyacrylonitrile (PAN) technique is a universal approach for immobilization heterogeneous catalysts due to the unique merits like stable physical and chemical properties, high surface area, as well as large continuous surface areas [54,96–98]. Wang et al. used PAN as a carrier to accommodate ZIF-67 nanoparticles [54], overcoming the challenge that the highly dispersed ZIF-67 powder material is extremely challenging to separate from the aqueous system (Fig. 2a). The cubic ZIF-67 particles immobilized on the PAN fibers with a size of approximately 220 nm were visualized in the SEM (Fig. 2b) and TEM (Fig. 2c) images. The elemental mapping (Fig. 2d) revealed that the cubic ZIF-67 particles with a size of approximately 220 nm were not only immobilized on the PAN fibers (range from 800 to 900 nm) surface but also uniformly distributed throughout the whole fiber. As illustrated in Fig. 2e, acid yellow-17 (AY) with an initial concentration of 500 mg L^{-1} could be decomposed over ZIF-67/PAN/PMS system. In addition, ca. 68.3% of tetracycline (TC), 100% of bisphenol A (BPA) and 98.3% of methylene blue (MB) were degraded within 10 min by the PMS activation over ZIF-67/PAN, demonstrating that ZIF-67/PAN could be widely employed for the activation for PMS toward the degradation of organic pollutants [54]. The leaching concentrations of cobalt ions from the ZIF-67/PAN were < 0.35 mg L^{-1}, which was lower than the counterpart Co-catalysts [63]. In order to exhibit clear advantages of reusability and expand the prospects of ZIF-67/PAN in practical applications, the authors designed a ZIF-67/PAN filter (Fig. 2f) to achieve the rapid and flexible AY degradation. Being compared to the powder ZIF-67, the

Table 1
Summary of the typical synthesis methods for ZIF-67.

Method	Precursors			Synthesis conditions			Ref.
	Metal salt	linker	Metal: linker ratio	Medium	Temp. (°C)	Time	
Solvothermal	Co(NO$_3$)$_2$.6H$_2$O	2-nitroimidazole	1:1	DMF/DEF	100	72 h	[38]
	Co(NO$_3$)$_2$.6H$_2$O	2-methylimidazole	1:6	Methanol	r. t.	24 h	[49]
	Co(NO$_3$)$_2$.6H$_2$O	2-methylimidazole	1:58	Deionized water	r. t.	6 h	[51]
	Co(NO$_3$)$_2$.6H$_2$O	2-methylimidazole	1:8	Methanol	60	4 h	[69]
ultrasound-assisted	Co(NO$_3$)$_2$.6H$_2$O	2-methylimidazole	1:40	Deionized water	r. t.	5 h	[70]
Microwave-assisted	Co(NO$_3$)$_2$.6H$_2$O	2-methylimidazole	1:4	ethanol and methanol (1:1 in v/v)	–	40 min	[68]
electrochemical deposition	cobalt sheet (4 cm × 2 cm)	2-methylimidazole	–	Ethanol, hexadecyl trimethyl ammonium bromide	–	4 h	[65]
steam-assisted conversion	Co(OAc)$_2$.4H$_2$O	2-methylimidazole	1;10	Deionized water	120	24 h	[66]

Note: DMF, N,N-dimethylformamide; DEF, N,N-diethylformamide; "-" means not mentioned in the literatures.

Table 2

Summary of ZIF-67 and immobilized ZIF-67 materials for PS-AOPs.

Catalysts	Substrate	Synthesis method	Organic pollutants	Conditions	Degradation efficiency/time	Mechanisms	Ref.
Pristine ZIF-67	–	Coprecipitation method	RhB	RhB, 50 mg L^{-1} (500 mL); catalyst, 10 mg L^{-1}; PMS, 150 mg L^{-1}; nature pH; 20 °C	80 %, 60 min	SO$_4^{\bullet-}$	[73]
ZIF-67/PAN	Electrospun polyacrylonitrile (PAN) Nanofibers	Electrospinning immobilization technique	Acid yellow-17 (AY)	AY, 500 mg L^{-1} (100 mL); catalyst, 100 mg L^{-1}; PMS, 150 mg L^{-1}; pH, 3.2; room temperature	95.1 %, 10 min	SO$_4^{\bullet-}$, •OH	[54]
ZIF@R	ion exchange resins	Self-assembly method	RhB	RhB, 10 mg L^{-1} (200 mL); catalyst, 50 mg L^{-1}; Oxone, 50 mg L^{-1}; pH, 7; 30 °C	100 %, 60 min	SO$_4^{\bullet-}$	[53]
NF/ZIF-67	Nickel foam (NF)	In situ growth method	RhB	RhB, 100 mg L^{-1} (200 mL); catalyst, a piece of NF/ZIF-67 (3 cm × 3 cm); PMS, 150 mg L^{-1}; pH, 7; 25 °C	99 %, 30 min	SO$_4^{\bullet-}$, •OH	[87]
PDA/ZIF-67@PP	Polypropylene membrane	In-situ synthesis of ZIF-67 catalyst on PDA-coated PP membrane surface	Methylene blue (MB), Methyl orange (MO)	MB or MO, 20 mg L^{-1} (flow through); catalyst, a piece of catalytic membrane; PMS, 0.3 mM; nature pH; room temperature	MB: 92.3 % MO: 99.5 %	SO$_4^{\bullet-}$, •OH, •O$_2^-$ and h$^+$	[88]
ZIF-67/PAN filters	Polyacrylonitrile fibers	In situ growth method	AY	AY, 500 mg L^{-1} (200 mL); catalyst, 100 mg L^{-1}; PMS, 500 mg L^{-1}; nature pH; room temperature	94.9 %, 10 min	SO$_4^{\bullet-}$, •OH	[47]
ZIF-67@CA	Cellulose aerogel	ZIF-67 doped in cellulose hydrogel and freeze-dry	Tetracycline (TC), p-nitrophenol (PNP)	TC, 30 mg L^{-1} (50 mL) and PNP 20 mg L^{-1} (50 mL); catalyst, 600 mg L^{-1}; PMS, 600 mg L^{-1}; nature pH; room temperature	80 % of PNP and 95 % of TC, 30 min	SO$_4^{\bullet-}$, •OH	[89]
ZIF-67/cellulose hybrid membrane	Cellulose membrane	In situ growth method	MB, RhB	MB/RhB, 10 mg L^{-1} (100 mL); catalyst, 50 mg L^{-1}; Oxone, 50 mg L^{-1}; nature pH; room temperature.	100 %, 60 min	SO$_4^{\bullet-}$, •OH	[90]
Co-ZIF@GEL Composite Aerogel	Sugarcane bagasse aerogels	In situ growth and freeze-dry	PNP	PNP, 10 mg L^{-1} (- mL); catalyst, 100 mg L^{-1}; PMS, 1 mM; pH, 6.8; 25 °C	98.5 %, 70 min	SO$_4^{\bullet-}$, •OH	[91]
MOF-MMC	polymer mixed-matrix coating	3D printing	RhB	RhB, 5 mg L^{-1} (flow through); catalyst, 200 mg L^{-1}; PMS, 200 mg L^{-1}; nature pH; room temperature	100 %, 10 min	–	[92]
Zn/Co-ZIF@GEL	sugarcane bagasse aerogel	Doping method	RhB	RhB, 50 mg L^{-1} (- mL); catalyst, 150 mg L^{-1}; PMS, 0.4 mM; pH, 6.8; 25 °C	100 %, 10 min	SO$_4^{\bullet-}$, •OH, •O$_2^-$ and ^{1}O$_2$	[94]
ZIF-67@PVDF ultrafiltration membrane	PVDF mixed-matrix ultrafiltration membrane	Nonsolvent-induced phase separation technique	orange II (AO7)	AO7, 20 mg L^{-1} (50 mL); catalyst, a piece of ZIF-67 @PVDF membrane with an effective area (3 cm × 3 cm); PMS, 1.0 g L^{-1}; pH, 11; room temperature	98,9 %. 30 min	SO$_4^{\bullet-}$, •OH	[95]
ZIF-67@SC	sugarcane	In situ growth method	MB	MB, 30 mg L^{-1} (flow through); catalyst, a piece of as-prepared ZIF-67 @SC sponge catalytic filter; PMS, 1.0 g L^{-1}; nature pH; room temperature	88,86 %, -	SO$_4^{\bullet-}$, •OH	[93]

Notes: "-" means not mentioned in the literatures; PAN, polyacrylonitrile; R, resin; NF, Nickel foam; PDA, polydopamine; PP, polypropylene; CA, cellulose aerogel; GEL, aerogels; MMC, mixed-matrix coating; 3D, three-dimensional; PVDF, polyvinylidene fluoride; SC, sugarcane.

as-prepared ZIF-67/PAN sacrificed the catalytic activity to some extent. However, its easy separation/recovery and long-term operation possibility provided a new approach to achieve PS-AOPs for practical wastewater remediation.

Inspired by the previous work [54], ZIF-67/PAN filter had further been designed by Wang et al. [47], in which the ZIF-67/PAN filter was prepared by an in-situ growth approach (Fig. 3a). Firstly, the Co (acac)$_2$/PAN fibers were synthesized by the electrospinning technique. Then, the obtained Co(acac)$_2$/PAN fibers were immersed in the 2-MIM solution overnight to harvest ZIF-67/PAN filters. According to SEM observation (Fig. 3b), the ZIF-67 NPs immobilized on PAN fibrous filter demonstrated dodecahedron morphology. It is well-known that the surface areas and porous structure exerted great influence on the catalytic performance [99,100]. The as-prepared ZIF-67/PAN filters exhibited a relatively large specific surface area (595.2 m^2 g^{-1}) compared to other MOF-based filters [54,101], which could be attributed to the high loading (50 wt%) of porous ZIF-67 resulting from the in-situ fabrication strategy. The ZIF-67/PAN filters exhibited an

excellent catalytic ability in reacting with PMS to produce SO$_4^{\bullet-}$ for the complete decomposition of AY within 10 min (Fig. 3c), which was a good solution to the problem of immobilized catalysts being less catalytically active than the powder catalysts in the previous work [54]. After 5 cycles, the catalytic degradation efficiency only decreased by 1.2%, demonstrating that the obtained ZIF-67/PAN filter could be used for long-term operation. Especially, the ZIF-67/PAN fibrous filter exhibited good flexibility, which could be immobilized in a swinnex syringe filter holder to avoid the cumbersome recovery step and realize the continuous degradation toward pollutants (Fig. 3d). Basically, the approach of loading ZIF-67 on PAN with excellent stability as well as strong processability exhibited the potential large-scale applications of ZIF-67-based catalyst in PS-AOPs.

Nowadays, developing substrate-immobilized MOFs on large supports for PS-AOPs is another potential solution for solving the recovery problem [76,81,102]. Wu et al. proposed a self-assembly strategy to anchor ZIF-67 on the resin (R) surface (Fig. 4a) [53], which not only preserved porous structures and metal coordination of ZIF-67 but also

Table 3

Summary of ZIF-67 composites materials for PS-AOPs.

ZIF-67 composites	Component	Synthesis method	Organic pollutant/ amount	Conditions	Degradation efficiency/ time	Mechanisms	Ref.
Fe_3O_4-MnO_2-ZIF-67	ZIF-67, Fe_3O_4, MnO_2	Solvothermal and hydrothermal	Carbamazepine (CBZ)	CBZ, 20 mg L^{-1} (100 mL); catalyst, 500 mg L^{-1}; PMS, 2 g L^{-1}; nature pH; room temperature	81 %, 2.5 min	$SO_4^{\bullet-}$, $\bullet OH$	[133]
Fe_3O_4@ZIF-67	ZIF-67, Fe_3O_4	Ultrasonic-assisted reverse co-precipitation method and homogeneous method	tetrabromobisphenol A (TBBPA)	TBBPA, 40 mg L^{-1} (50 mL); catalyst, 100 mg L^{-1}; PMS, 100 mg L^{-1}; nature pH; room temperature	100 %, 3 min	$SO_4^{\bullet-}$, $\bullet OH$ and $^1O_2$	[55]
Fe_3O_4-PVP@ZIF-67	ZIF-67, Fe_3O_4, PVP	Microwave-assisted method	Bisphenol F (BPF)	BPF, 20 mg L^{-1} (100 mL); catalyst, 150 mg L^{-1}; PMS, 0.3 mM; nature pH; room temperature	99.8 %, 60 min	$SO_4^{\bullet-}$, $\bullet OH$	[134]
α-Fe_2O_3@ZIF-67	ZIF-67, α-Fe_2O_3	Surfactant-assisted reflux method, hydrothermal method and ultrasonic irradiation	Ciprofloxacin (CIP)	CIP, 20 mg L^{-1} (100 mL); catalyst, 100 mg L^{-1}; PMS, 200 mg L^{-1}; nature pH; room temperature	100 %, 30 min	$SO_4^{\bullet-}$, $\bullet OH$ and $^1O_2$	[56]
Ag/ZIF-67@GO	ZIF-67, α-Fe_2O_3, Ag	Homogeneous method and $NaBH_4$ reduction method	Phenol and *E. coli*	Phenol, 20 mg L^{-1} (50 mL); catalyst, 50 mg L^{-1}; PMS, 300 mg L^{-1}; pH, 7; room temperature *E. coli*, 10^6 CFU mL^{-1}; catalyst, 1 mg L^{-1}; PMS, 10 mg L^{-1}; nature pH; 37 °C	Phenol: 100 %, 30 min *E. coli*: 100 %, 15 min	$SO_4^{\bullet-}$, $\bullet OH$ $\bullet O_2^-$ and h^+	[45]
ZIF-67/Fe_3O_4	ZIF-67, Fe_3O_4	Sol-gel method	CIP	CIP, 0.05 mM (100 mL); catalyst, 400 mg L^{-1}; PMS, 10 mg L^{-1}; nature pH; 25 °C	100 %, 48 min	$SO_4^{\bullet-}$, $\bullet OH$	[135]
HAnW@CoMOF	ZIF-67, Fe_3O_4	In-situ growing method	TC	TC, 15 mg L^{-1} (50 mL); catalyst, 300 mg L^{-1}; PMS, 0.1 mol L^{-1}; pH, 6.5; room temperature	97 %, 15 min	$^1O_2$, $\bullet O_2^-$, $\bullet OH$ and $SO_4^{\bullet-}$	[136]
$CuFe_2O_4$@ZIF-67	ZIF-67, $CuFe_2O_4$	In-situ growing method and heat treatment	MB	MB, 20 mg L^{-1} (50 mL); catalyst, 75 mg L^{-1}; PMS, 125 mg L^{-1}; pH, 6.4; 20 °C	98.9 %, 30 min	$SO_4^{\bullet-}$, $^1O_2$ and $\bullet OH$	[137]
ZIF-67/VTM	ZIF-67, vanadium-titanium magnetite	Solvothermal method	Levofloxacin (LVF)	LVF, 10 mg L^{-1} (100 mL); catalyst, 100 mg L^{-1}; PMS, 75 mg L^{-1}; pH, 6.4; 8 °C	93.3 %, 60 min	$SO_4^{\bullet-}$, $\bullet OH$ and $^1O_2$	[138]
FeCo-LDH	FeCo-LDH	Method for stirring ZIF-67 and $Fe(NO_3)_3.9H_2O$ in ethanol	TC	TC, 30 mg L^{-1} (100 mL); catalyst, 200 mg L^{-1}; PMS, 250 mg L^{-1}; nature pH; room temperature	94 %, 30 min	$SO_4^{\bullet-}$, $\bullet O_2^-$	[139]

Notes: PVP, polyvinyl pyrrolidone; GO, graphene oxide HAnW, Hydroxyapatite nanowires VTM, vanadium-titanium magnetite; LDH, layered double hydroxides.

retained the convenient features of resins. The morphologies of the as-prepared ZIF-67 @R illustrated that ZIF-67 with a shape of rhombic dodecahedron was loaded on the surface of the resin (Fig. 4b–e). It was found that the traditional peaks of ZIF-67 appeared in the XRD pattern of ZIF-67 @R [103], confirming the successful fabrication of immobilized catalyst. After self-assembling modification, ZIF@R was identified to activate Oxone (potassium peroxymonosulfate) for complete removal of RhB (Fig. 4f), which exhibited convenient recyclability, high efficiency and outstanding stability for the degradation of organic pollutants by aqueous chemical oxidation reactions. The fabrication of durable and re-usable ZIF-67 @R provided an approach to prepare effective PS-AOPs catalyst with enhanced stability for persulfate activation to decompose the organic pollutants.

The membrane-based technology for wastewater purification benefited from higher effluent quality and smaller occupied areas has gained increasing attentions [104–106]. Nevertheless, membrane fouling has become the main limitation for its further application [107–109]. Introducing membrane technology into catalytic oxidation processes is an approach of "killing two birds with one stone", which can develop the self-cleaning membrane and overcome the shortcoming of agglomeration and difficult recycling of powder catalysts [110,111]. Poly-dopamine (PDA) can form strong covalent or non-covalent bonding interactions, which can polymerize and adhere to the surface of any organic and inorganic substances [112–114]. Thus, PDA can act as a molecular binder to cement the MOF particles to the substrate surface

for fabricating MOF membrane. Li et al. [88] obtained a novel visible-light biomimetic PDA and ZIF-67 decorated polypropylene (PDA/ZIF-67 @PP) system to activate the PMS for the elimination of organic dye pollutants (Fig. 5a). The preparation of the catalytic membrane was divided into two steps. (i) Poly-dopamine (PDA) was coated on the surface of polypropylene (PP) through self-polymerization to enhance the adhesion of the membrane. (ii) ZIF-67 was decorated into PP membrane by in-situ synthesis. The successfully fabricated PDA/-ZIF-67 @PP membrane, which was confirmed by SEM (Fig. 5b), and elemental mapping (Fig. 5c), improved the pure water flux owing to the improvement of hydrophilicity. The highest MB and methyl orange (MO) decomposition efficiency as well as TOC removal efficiency were accomplished over the PDA/ZIF-67 @PP/PMS system under the irradiation of visible light. As depicted in Fig. 5d, the as-prepared membrane could still achieve 73.3% and 82.0% TOC removal efficiencies after five runs' operation. In addition, the newly-designed PDA/ZIF-67 @PP membrane demonstrated excellent anti-fouling performance in the presence of simultaneous visible light and PMS for the wastewater purification, which could be observed from the research of anti-fouling property of the prepared membrane. From the investigation of the flux recovery, it could be found that the membrane foulants could be removed effectively over PMS/visible light/ PDA/ZIF-67 @PP membrane system, showing excellent self-cleaning performance of the prepared membrane. This work provided an example to couple PS-AOPs with the membrane processes, which addressed the bottleneck of

Table 4

Summary of ZIF-67 derivatives for PS-AOPs.

Catalysts	Precursors	Composition	Derivative method	Organic pollutant	Conditions	Degradation efficiency/time	Mechanisms	Ref.
The cobalt-based metal oxides derived from ZIF-67 and their hybrid materials for PS-AOPs								
Co_3O_4	ZIF-67	Co_3O_4	1st: N_2, 650 °C, 5 h; 2nd: Air, 550 °C, 1 h	RhB	RhB, 0.1 mM (200 mL); catalyst, 50 mg L^{-1}; oxone, 1.0 mM; pH, 7.03; 25 °C	100 %, 90 min	$SO_4^{\bullet-}$	[46]
Hollow Co_3O_4/C	Hollow ZIF-67	Co_3O_4, C	1st: N_2, 500 °C, 3 h; 2nd: Air, 220 °C, 4 h	BPA	BPA, 87.6 μM (50 mL); catalyst, 100 mg L^{-1}; PMS, 325.3 μM; nature pH; 25 °C	97 %, 4 min	$SO_4^{\bullet-}$, •OH	[168]
Co_3O_4/CNTs	Core-shell Zn/Co MOFs	Co_3O_4, CNTs	1st: N_2, 920 °C, 2 h; 2nd: Air, 350 °C, 2 h	oxytetracycline (OTC)	OTC, 20 mg L^{-1} (38 mL); catalyst, 526 mg L^{-1}; PMS,1 mg mL^{-1}; pH, 7; 25 °C	93.6 %, 80 min	$SO_4^{\bullet-}$, •OH	[169]
$CoAl_2O_4$@AP	ZIF-67@γ-Al_2O_3	$CoAl_2O_4$	Air, 450 °C, 3 h	metronidazole (MNZ)	MNZ, 20 mg L^{-1} (80 mL); catalyst, 20 g L^{-1}; PMS, 1.0 mM; pH, 6.48; 35 ± 1 °C	97 %, 100 min	$SO_4^{\bullet-}$, •OH, •O_2^- and $^1O_2$	[161]
Co_3O_4/$NiCo_2O_4$	ZIF-67/Ni-Co LDH	Co_3O_4, $NiCo_2O_4$	Air, 350 °C, 2 h	BPA	BPA, 8 mg L^{-1} (50 mL); catalyst, 0.1 g L^{-1}; PDS, 74 μM; pH, 6.8; 25 ± 1 °C	76.7 %, 18 min	Electron transfer	[57]
$ZnCoO_x$	Zn doped ZIF-67	Co_3O_4, ZnO	Air, 400 °C, 2 h	RhB	RhB, 50 mg L^{-1} (100 mL); catalyst, 200 mg L^{-1}; PMS, 100 mg L^{-1}; pH, 7; 25 °C	100 %, 10 min	$^1O_2$, $SO_4^{\bullet-}$	[170]
Co_3O_4@NCNTs	g-C_3N_4/ZIF-67	Co_3O_4, N-doped carbon nanotube	1st: N_2, 800 °C, 1 h; 2nd: Air, 350 °C, 4 h	sulfamethoxazole (SMX)	SMX, 10 mg L^{-1} (100 mL); catalyst, 10 mg L^{-1}; PMS, 200 mg L^{-1}; nature pH; 25 ± 1 °C	100 %, 20 min	$^1O_2$, $SO_4^{\bullet-}$ and •OH	[171]
Co_2AlO_4/ $CoAl_2O_4$@Al_2O_3	ZIF-67@γ-Al_2O_3	Co_2AlO_4	Air, 350 °C, 4 h	MNZ	MNZ, 20 mg L^{-1} (80 mL); catalyst, 20 g L^{-1}; PMS, 1.0 mM; pH, 6.42; 25 ± 1 °C	99.6 %, 90 min	•OH, $SO_4^{\bullet-}$ •O_2^- and $^1O_2$	[172]
ZnO-Co_3O_4/N-C	ZIF-8/ZIF-67 Hollow Cage	Co_3O_4, ZnO, amorphous carbon and N	Air, 330 °C, 2 h	BPA	BPA, 25 mg L^{-1} (40 mL); catalyst, 250 mg L^{-1}; PMS, 25 mM; nature pH; 30 °C	93 %, 10 min	•OH, $SO_4^{\bullet-}$	[173]
Mo/Co HHBONs	PMA@ZIF-67	Mo doped Co_3O_4	Air, 500 °C, 2 h	Levofloxacin (Lev)	Lev, 10 mg L^{-1} (50 mL); catalyst, 100 mg L^{-1}; PMS, 1.0 mM; pH, 7; 25 °C	85 %, 4 min	$SO_4^{\bullet-}$, •OH, •O_2^- and $^1O_2$	[174]
PdO_x/Co_3O_4	Pd(acac)$_2$/ZIF-67	PdO_x, Co_3O_4	Air, 500 °C, 2 h	BPA	BPA, 12.5 mg L^{-1} (40 mL); catalyst, 250 mg L^{-1}; PMS, 250 mg L^{-1}; nature pH; 30 °C	96 %, 30 min	$SO_4^{\bullet-}$, •OH	[175]
Biochar	ZIF-67/BC	Co_3O_4/C, BC	Air, 350 °C, 2 h	BPA	BPA, 20 mg L^{-1} (50 mL); catalyst, 100 mg L^{-1}; PMS, 10 mM; nature pH; 30 °C	100 %, 30 min	$SO_4^{\bullet-}$, •OH	[176]
CoZnO-PC	PVP assisted Co-Zn bimetal based ZIFs	$ZnCo_2O_4$, graphitic porous carbon, N	1st: N_2, 600 °C, 3 h; 2nd: air, 450 °C, 3 h	BPA	BPA, 0.02 mM (90 mL); catalyst, 100 mg L^{-1}; PMS, 2.0 mM; nature pH; room temperature	100 %, 20 min	$^1O_2$, •OH	[177]
Co/CoO_x@NC	Co-Zn-ZIF modified by graphene oxide	Co, CoO, Co_3O_4, graphitic carbon,	N_2, 950 °C, 2 h	Phenol	Phenol, 20 mg L^{-1} (100 mL); catalyst, 100 mg L^{-1}; PMS, 500 mg L^{-1}; pH, 6.8; 25 °C	97.1 %, 10 min	Electron transfer pathway, $SO_4^{\bullet-}$, •OH and $^1O_2$	[178]
Co_xO_y@CCNM	ZIF-67@PAN membranes	CoO, Co_3O_4	–	TC	TC, 30 mg L^{-1} (flow through); catalyst, 200 mg L^{-1}; PMS, 4 mM; pH, 7; room temperature	100 %, 20 min	$^1O_2$, •O_2^-, $SO_4^{\bullet-}$ and •OH	[179]
Cage-like Co_3O_4/N–C composite and nest-like Co_3O_4	ZIF-67	Co_3O_4	Air, 430 °C, 2 h (cage-like Co_3O_4/N–C);	BPA	BPA, 12.5 mg L^{-1} (80 mL); catalyst, 125 mg L^{-1}; PS, 20 mM; nature pH; 30 °C	85 %, -	$SO_4^{\bullet-}$, •OH	[180]

Table 4 (*continued*)

Catalysts	Precursors	Composition	Derivative method	Organic pollutant	Conditions	Degradation efficiency/time	Mechanisms	Ref.
CoP/CoO$_x$	ZIF-67	CoP, CoO, Co$_3$O$_4$	Air, 500 °C, 2 h (Co$_3$O$_4$) 1st: air, 350 °C, 2 h; 2nd: N$_2$ (NaH$_2$PO$_2$), 350 °C, 3 h	TC	TC, 20 mg L^{-1} (100 mL); catalyst, 30 mg L^{-1}; PMS, 300 mg L^{-1}; pH, 6.7; 25 °C	97.8 %, 15 min	SO$_4^{\bullet-}$, •OH and •O$_2^-$	[181]
Co$_3$O$_4$@NPC/rGO	Zn-Co-ZIFs/GO	Co$_3$O$_4$, graphitic carbon, GO, N	1st: N$_2$, 800 °C, 2 h; 2nd: air, 200 °C, 1 h	SMX	SMX, 25 mg L^{-1} (100 mL); catalyst, 15 mg L^{-1}; PMS, 0.2 mM; pH, 7; 25 °C	100 %, 5 min	SO$_4^{\bullet-}$, •OH, •O$_2^-$,^{1}O$_2$ and direct electron transfer	[182]
Co-O@CN	gC$_3$N$_4$@ZIF-67	Co$_3$O$_4$, Co	1st: Ar, 600 °C, 2 h; 2nd: air, 250 °C, 8 h	Ofloxacin (OFX)	OFX, 10 mg L^{-1} (100 mL); catalyst, 100 mg L^{-1}; PMS, 0.01 mg L^{-1}; pH, 6.5; room temperature	100 %, 20 min	SO$_4^{\bullet-}$, •OH, •O$_2^-$ and^{1}O$_2$	[183]
Co$_3$O$_4$-C@CoSiO$_x$	ZIF-67@SiO$_2$	Co$_3$O$_4$-C, CoSiO$_x$	1st: Ar, 600 °C, 2 h; 2nd: Ar, 200 °C, 2 h	CIP	CIP, 30 mg L^{-1} (100 mL); catalyst, 500 mg L^{-1}; PMS, 20 mg L^{-1}; nature pH; room temperature	98.2 %, 17 min	SO$_4^{\bullet-}$, •OH, •O$_2^-$,^{1}O$_2$ and direct electron transfer	[184]
Co-N/C	ZIF-67	Co, graphitic carbon, N	Ar, 900 °C, 2 h; sulfur acid etching	TC	TC, 40 μmol L^{-1} (100 mL); catalyst, 100 mg L^{-1}; PMS, 0.2 mmol L^{-1}; pH, 7; 30 °C	85.4 %, 15 min	^{1}O$_2$	[185]
Co$_3$O$_4$@N-rGO	SA@GO@ZIF-67	Co$_3$O$_4$, N-doped graphene	N$_2$, 450 °C, 4 h	SMX	SMX, 30 mg L^{-1} (100 mL); catalyst, 20 mg L^{-1}; PMS, 300 mg L^{-1}; nature pH; 25 °C	100 %, 10 min	^{1}O$_2$, SO$_4^{\bullet-}$, •OH and •O$_2^-$	[186]
ZIF-67 derived carbon materials and their hybrid materials for PS-AOPs								
CCN	ZIF-67	Co, C	N$_2$, 600 °C, 4 h	Caffeine	Caffeine, 20 mg L^{-1} (200 mL); catalyst, 50 mg L^{-1}; Oxone, 250 mg L$^-$; pH, 3.5; 20 °C^1	100 %, 120 min	SO$_4^{\bullet-}$	[52]
NPSC	ZIF-67@PZS	C, N, O, P, S, and Co	N$_2$, 700 °C, 4 h; sulfur acid etching	BPA	BPA, 25 mg L^{-1} (- mL); catalyst, 60 mg L^{-1}; PMS, 400 mg L^{-1}; nature pH; 20 °C	90.1 %, 30 min	•OH, SO$_4^{\bullet-}$ and •O$_2^-$	[143]
NCNTFs	ZIF-67	N doped carbon nanotubes, Co nanoparticles	1st: N$_2$/H$_2$(95/5), 350 °C, 1.5 h; 2nd: N$_2$/H$_2$(95/5), 800 °C, 3.5 h; sulfur acid etching	BPA	BPA, 25 mg L^{-1} (50 mL); catalyst, 50 mg L^{-1}; PMS, 400 mg L^{-1}; nature pH; 20 °C	97.3 %, 30 min	^{1}O$_2$ and SO$_4^{\bullet-}$	[146]
Co@N-C	ZIF-67/Urea	Co@N-C	Ar, 600 °C, 2 h; sulfur acid etching	BPA	BPA, 10 mg L^{-1} (100 mL); catalyst, 100 mg L^{-1}; PMS, 0.25 mM; nature pH; room temperature	100 %, 30 min	^{1}O$_2$	[187]
Co@NC	ZIF-67	Co@NC	Ar, 900 °C, 3 h; sulfur acid etching	P-Chloroaniline (PCA)	PCA, 0.15 mM (100 mL); catalyst, 150 mg L^{-1}; PS, 2.5 mM; pH, 7.5; 25 °C	97.3 %, 60 min	SO$_4^{\bullet-}$, •OH and non-radical oxidation processes	[188]
NDHC	ZIF-67@AF	N-doped hierarchical carbon	N$_2$, 900 °C, 5 h; acid etching	BPA	BPA, 20 mg L^{-1} (50 mL); catalyst, 150 mg L^{-1}; PMS, 200 mg L^{-1}; nature pH; room temperature	98 %, 5 min	^{1}O$_2$, SO$_4^{\bullet-}$, •OH and •O$_2^-$	[189]
CoN/NC@SiO$_2$	ZIF-67@SiO$_2$	CoN, N doped carbon layers, SiO$_2$	NH$_3$, 500 °C, 2 h	TC	TC, 50 mg L^{-1} (100 mL); catalyst, 100 mg L^{-1}; PMS, 25 mg L^{-1}; nature pH; room temperature	98.6 %, 30 min	•O$_2^-$, •OH, SO$_4^{\bullet-}$ and ^{1}O$_2$	[190]
Cu-Co/NC	copper-doped PS@ZIF-67	Cu, Co, N, hollow carbon	1st: Ar, 200 °C, 2 h; 2nd: Ar, 700 °C, 2 h	4-nitrophenol (4-NP)	4-NP, 25 mg L^{-1} (60 mL); catalyst, 100 mg L^{-1}; PMS, 1000 mg L^{-1}; nature pH; 30 °C	90 %, 60 min	SO$_4^{\bullet-}$, •OH and •O$_2^-$	[191]
YSCCNs	Yolk-shell ZIF-67	C, Co, N	tannic acid etching, N$_2$, 600 °C, 2 h	BPA	BPA, 20 mg L^{-1} (50 mL); catalyst, 100 mg L^{-1}; PMS, 150 mg L^{-1}; pH, 8.23; 20 °C	100 %, 15 min	SO$_4^{\bullet-}$, •OH	[58]

Table 4 (*continued*)

Catalysts	Precursors	Composition	Derivative method	Organic pollutant	Conditions	Degradation efficiency/time	Mechanisms	Ref.
CFNC-30 NPs	ZIF-67/ CoFe₂O₄	Co⁰, CoFe alloy, graphitic carbon, N	N₂, 900 °C, 3 h	4-CP	4-CP, 50 mg L⁻¹ (200 mL); catalyst, 89 mg L⁻¹; PMS, 1110 mg L⁻¹; pH, 6.6; 30 ± 1 °C	99.1 %, 30 min	SO₄•⁻, •OH and ¹O₂	[192]
CZIF-67@SiO₂	yolk-shell ZIFs@SiO₂	SiO₂, Co, C	Ar, 700 °C, 3 h	RhB	RhB, 50 mg L⁻¹ (250 mL); catalyst, 40 mg L⁻¹; PMS, 250 mg L⁻¹; nature pH; 20 °C	100 %, 40 min	¹O₂, •O₂ and SO₄•⁻	[193]
Co@NC-800	ZIF-67	Co, C, N	1st: N₂, 300 °C, 1 h; 2nd: N₂, 800 °C, 2 h	TC	TC, 30 mg L⁻¹ (100 mL); catalyst, 200 mg L⁻¹; PMS, 200 mg L⁻¹; nature pH; room temperature	90.1 %, 3 min	¹O₂, SO₄•⁻ and •O₂	[194]
CoNC/CNTs	Core-shell ZIF-67/ ZIF-8	Co, CNTs, N	N₂, 920 °C, 3 h	SMX	SMX, 25 mg L⁻¹ (50 mL); catalyst, 50 mg L⁻¹; PMS, 100 mg L⁻¹; nature pH; 25 ± 1 °C	96.4 %, 45 min	SO₄•⁻, •OH and ¹O₂	[195]
Co@N-C-2	Core-Shell ZIF-8@ZIF-67	Co, CNTs, N	N₂, 900 °C, 3 h	Orange II and RhB; phenol, BPA, SMX and methylparaben (MeP)	Orange II and RhB, 80 mg L⁻¹ (200 mL); phenol, BPA, SMX and MeP, 20 mg L⁻¹; catalyst, 100 mg L⁻¹; PMS, 300 mg L⁻¹; 15 min; pH, 7.5 ± 1; 25 °C	Orange II (98.1 %), BPA (98.6%), phenol (98.0 %), RhB (100 %), SMX (99.5 %), and MeP (98.8 %)	¹O₂, electron transformation	[196]
CoCN	ZIF-67/melamine	Co, gC₃N₄	N₂, 600 °C, 5 h	BPA	BPA, 20 mg L⁻¹ (50 mL); catalyst, 200 mg L⁻¹; PMS, 200 mg L⁻¹; pH, 7; 25 °C	100 %, 10 min	SO₄•⁻, •OH •O₂, ¹O₂ and h⁺	[197]
Co@N-C	ZIF-67	Co, C, N	1st: Ar/H₂ (90 %/10 %), 350 °C, 1.5 h; 2nd: Ar/H₂ (9 0%/10 %), 750 °C, 3.5 h sulfur acid etching	4-CP	4-CP, 0.1 mM (50 mL); catalyst, 50 mg L⁻¹; P PMS, 0.25 mM; PDS, 0.1 mM; pH, 7; room temperature	100 %, 48 min	SO₄•⁻ (Co@N-C-750/PMS); mediated electron transfer (Co@N-C-750/PDS)	[198]
CC@CNCo-x	Cot@ZIF-67	Co, C, N, O	N₂, 900 °C,	BPA	BPA, 20 mg L⁻¹ (50 mL); catalyst, 100 mg L⁻¹; PMS, 140 mg L⁻¹; pH, 9.09; room temperature	100 %, 15 min	SO₄•⁻, •OH	[199]
NCoHCP	Core–shell ZIF-8@ZIF67	Co, C, N	Ar, 920 °C, 3 h	BPA	BPA, 0.1 mM (30 mL); catalyst, 200 mg L⁻¹; PMS, 4 mM; pH, 6.7; 30 °C	100 %, 45 s	SO₄•⁻, •OH and ¹O₂	[200]
Co@NG	ZIF-67	Co, C, N	1st: Ar, 500 °C, 1 h; 2nd: Ar, 900 °C, 2 h	Phenol	Phenol, 1 mM (50 mL); catalyst, 50 mg L⁻¹; PMS, 3 mM; pH, 7.2; 25 °C	100 %, 12 min	Electron transfer	[201]
FeCo₂O₄-N-C	Fe-Co-ZIF	N, C doped FeCo₂O₄	1st: N₂, 400 °C, 0.5 h; 2nd: air, 400 °C, 0.5 h	MB	MB, 50 mg L⁻¹ (50 mL); catalyst, 200 mg L⁻¹; PMS, 500 mg L⁻¹; nature pH; 30 °C	100 %, 40 min	SO₄•⁻, •OH	[202]
Co₃Fe₇ and Co⁰ embedded in N-doped porous carbons	CoFe₂O₄/gᵥ-C₃N₄/ZIF-67	Graphite carbon, Co⁰, and Co₃Fe₇ alloy	N₂, 900 °C, 3 h	4-chlorophenol (4-CP)	4-CP, 50 mg L⁻¹ (200 mL); catalyst, 150 mg L⁻¹; PMS, 750 mg L⁻¹; pH, 6.6; 25 ± 1 °C	100 %, 30 min	¹O₂, SO₄•⁻, and •OH	[203]
HCoNC	ZIF-67	Co, CoO, N-containing carbon	tannic acid etching, N₂, 600 °C, 1 h	bis(4-hydroxyphenyl) ketone (BHK)	BHK, 5 mg L⁻¹ (- mL); catalyst, 100 mg L⁻¹; PMS, 150 mg L⁻¹; pH, 7; 30 °C	100 %, 30 min	SO₄•⁻, •OH and ¹O₂	[204]
Co/N/S-doped yolk-shell carbon	ZIF-67@TCA	Co, Co₉S₈, graphite carbon, N	Air, 800 °C, 1 h	4-Nitrophenol (4-NP)	4-NP, 60 mg L⁻¹ (- mL); catalyst, 10 mg; PMS, 200 mg L⁻¹; pH, 7; 30 °C	100 %, 20 min	SO₄•⁻, •OH and ¹O₂	[205]
Co/NC	Co/Zn ZIFs	Co SAs, graphite carbon, N	N₂, 900 °C, 3 h, sulfur acid etching	BPA	BPA, 10 mg L⁻¹ (200 mL); catalyst, 100 mg L⁻¹; PMS, 1 mM; pH, 6.8; 25 °C	95 %, 30 min	¹O₂, high valent cobalt	[206]
Co@N-PC	ZIF-67@PS	Co, graphite carbon	Air, 700 °C, 5 h	MB	MB, 30 mg L⁻¹ (100 mL); catalyst, 133 mg L⁻¹; PMS, 100 mg L⁻¹; pH, 6.3; 25 °C	100 %, 30 min	SO₄•⁻, •OH	[207]
Co-HPNC	SiO₂@ZIF-67			AO7		98.1 % 10 min	¹O₂, SO₄•⁻ and •OH	[208]

8

Table 4 (*continued*)

Catalysts	Precursors	Composition	Derivative method	Organic pollutant	Conditions	Degradation efficiency/time	Mechanisms	Ref.
		Nitrogen-doped graphene, Co	Air, 500–900 °C, 2 h, sulfur acid etching, NaOH etching		AO7, 0.1 mM (100 mL); catalyst, 50 mg L^{-1}; PMS, 1 mM; nature pH; room temperature			
B-NC	ZIF-67	Graphite carbon, N, B	1st: N_2, 950 °C, 2 h 2nd: NC and boracic acid doping 3rd: -, 1100 °C, 2 h	TC	TC, 20 mg L^{-1} (150 mL); catalyst, 100 mg L^{-1}; PMS, 25 mg L^{-1}; nature pH; 25 °C	94 % 60 min	$^1O_2$, electron transfer	[209]
HYSCN	Hollow ZIFs	Co, graphitic carbon	N_2, 700–1000 °C, 3 h	CBZ	CBZ, 5 mg L^{-1} (100 mL); catalyst, 60 mg L^{-1}; PMS, 0.4 mM; nature pH; room temperature	100 % 30 min	$SO_4^{\bullet-}$, •OH and •O_2^-	[210]
ZIF-67 derived cobalt sulfide and their hybrid materials for PS-AOPs								
CoS@GN	ZIF-67@GN	CoS, graphene nanoshee	1st: TAA sulfuration, 120 °C, 4 h; 2nd: N_2, 600 °C, 2 h	BPA	BPA, 20 mg L^{-1} (50 mL); catalyst, 100 mg L^{-1}; PMS, 100 mg L^{-1}; pH, 6.65; 25 °C	92 %, 8 min	$SO_4^{\bullet-}$	[211]
Amorphous CoS_x cages	ZIF-67	Amorphous CoS_x	TAA sulfuration, 120 °C, 5 h	TC	TC, 30 mg L^{-1} (100 mL); catalyst, 200 mg L^{-1}; PMS, 300 mg L^{-1}; pH, 5; 25 °C	100 %, 20 min	$SO_4^{\bullet-}$, •OH and •O_2^-	[59]
CoS_x@SiO_2 nanocages	ZIF-67@SiO_2	CoS_x @SiO_2	TAA sulfuration, 120 °C, 5 h	SMX	SMX, 5 mg L^{-1}; catalyst, 200 mg L^{-1}; PMS, 0.2 mM	100 %, 6 min	$SO_4^{\bullet-}$ and $^1O_2$	[48]

Notes: "-" means not mentioned in the literatures; CNTs, carbon nanotubes; AP, Al_2O_3 pellet; NCNTs, doped carbon nanotube composites; HHBONs, hollow bimetal oxides nanocages; BC, biochar; PC, porous carbon; PVP, polyvinyl pyrrolidone; NC, nitrogen-doped porous carbon; NPC, N-doped porous carbon; rGO, reduced graphene oxide; N-rGO, nitrogen-doped graphene; SA, sodium alginate; NC, nitrogen-doped porous carbon; CCNM, carbon catalytic nanofibrous membrane; CCN, carbon nanocomposite; NPSC, N, P, and S tri-doped hollow carbon shells; NCNTFs, Nitrogen-doped carbon nanotubes frameworks; N-C, N-doped carbons; Co@NC, nitrogen-doped porous Co@C nanoboxes; NDHC, N-doped hierarchical carbon; NC, doped carbon nanotube composites; Cu-Co/NC, Cu-Co/N-doped hollow carbon spheres; YSCCNs, Yolk-shell Co/C nanoreactors; CFNC NPs, containing carbon (N-C) nanoparticles; CZIF-67 @SiO_2, Carbonized yolk-shell ZIFs@SiO_2; Co@NC, N-doped porous carbon encapsulated magnetic Co; CoNC/CNTs, Co/N co-doped carbon nanotube; Co@N-C, Co/N co-doped polyhedron carbonaceous; CoCN, Co sites embedded in carbon nitride; Co@N-C, Cobalt/N-doped carbon composites; CC@CNCo, Cot@ZIF-67 derived carbon/Co materials; NCoHCP, Nitrogen-coordinated cobalt embedded in hollow carbon polyhedron; Co@NG, Co nanoparticles encapsulated in nitrogen (N)-doped graphene; $FeCo_2O_4$-N-C, Nitrogen-containing carbon/$FeCo_2O_4$ composites; $FCCN_V$, HCoNC, hollow N-containing carbon nanocube; TCA, trithiocyanuric acid; SAs, single atoms; PS, poplar sawdust; HPNC, carbon-nitrogen doped composite catalyst with honeycomb porous structure; HYSCN, hollow yolk-shell nanoreactor with shell confined Co species; CoS@GN, graphene nanosheet-immobilized hollow cobalt sulfide nanocrystals; TAA, thioacetamide.
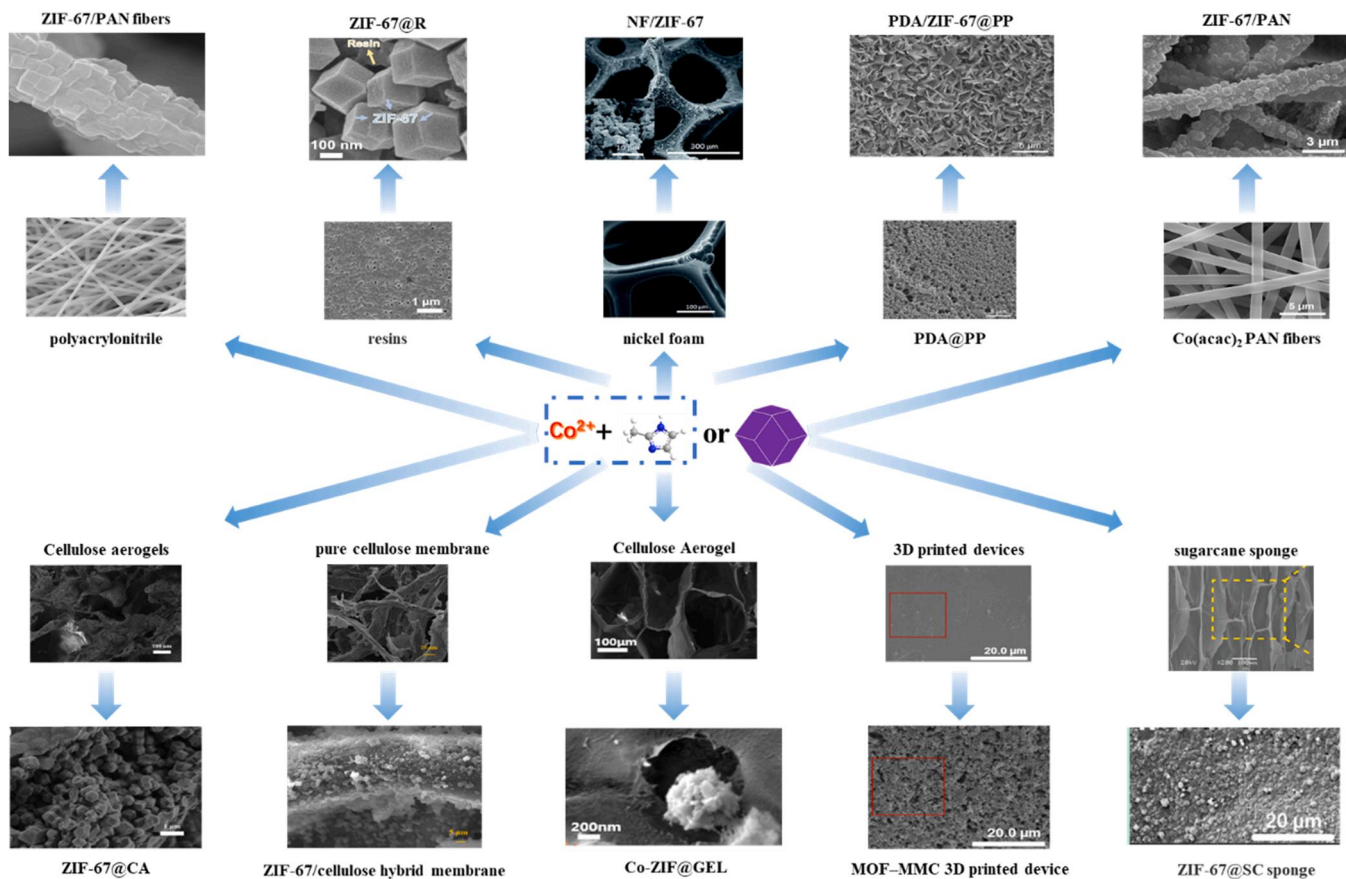
Fig. 1. The SEM illustration of the immobilized ZIF-67 and the corresponding substrates. Reproduced with permission from Ref. [47,53,54,87–93]. Copyright 2017 Elsevier. Copyright 2018 Elsevier. Copyright 2018 Royal Society of Chemistry. Copyright 2019 Elsevier. Copyright 2020 Elsevier. Copyright 2020 Elsevier. Copyright 2021 Springer Nature. Copyright 2021 Multidisciplinary Digital Publishing Institute. Copyright 2019 Elsevier. Copyright 2022 Elsevier.

membrane fouling during the operation.

2.2. ZIF-67 composites for PS-AOPs

Novel multifunctional composites can be formed through the controllable integration of ZIF-67 and functional materials. These as-prepared composites exhibit better properties like higher recycling rates, more catalytic active sites, and faster electron transfer rates, than the individual components, which have attracted widespread attentions [115]. To improve catalytic performance of MOFs materials, our research group has prepared different composites based on MOFs, such as MIL family: MIL-100(Fe)/g-C$_3$N$_4$ [81], MIL-100(Fe)/PANI [116], Ag/Ag$_3$PO$_4$/MIL-125-NH$_2$ [117], WO$_3$/MIL-100(Fe) [118], Bi$_{12}$O$_{17}$-Cl$_2$/MIL-100(Fe) [119], PANI/MIL-88A(Fe) [120], MIL-53 (Fe)/Bi$_{12}$O$_{17}$Cl$_2$ [121], PDINH/MIL-88A(Fe) [9], MIL-100(Fe)/CoS [122]; UiO (Abbreviation of University of Oslo) family: g-C$_3$N$_4$/UiO-66 [123], UiO-66-NH$_2$/Ag$_2$CO$_3$ [124], S-TiO$_2$/UiO-66-NH$_2$ [125], NH$_2$-UiO-66/PTCDA [126], and Bi$_5$O$_7$I/UiO-66-NH$_2$ [127]; BUC (Beijing University of Civil Engineering and Architecture) family: BUC-21/Bi$_{24}$O$_{31}$Br$_{10}$ [128], BUC-21/N-K$_2$Ti$_4$O$_9$ [129], BUC-21/Cd$_{0.5}$Zn$_{0.5}$S [130], BUC-21/g-C$_3$N$_4$ [131], BUC-21/Titanate Nanotube [132]. All of these composite catalysts greatly improved the catalytic performance and achieved the effect of "1 + 1 > 2". To enhance the PS-AOPs performance of single-component ZIF-67, some new multifunctional composites can be prepared through the controllable integration of ZIF- 67 and functional materials, which exhibited superior properties to the individual ZIF-67 through the collective behavior of each functional unit. The ZIF-67 composites can be divided into two classes like magnetic and non-magnetic material (Fig. 6). As

shown in Table 3, we summarized the application and development of ZIF-67 composites in the field of PS-AOPs. In this section, we highlighted the recent progress of ZIF-67 composites as emerging catalysts for PS-AOPs.

The single-component powder ZIF-67-based catalyst suffered from the difficult recyclability from the treated aqueous solution. As well, the immobilized ZIF-67 catalyst might sacrifice the catalytic activities to some extent. Hence, it's crucial and essential to enhance the catalytic performance and endow the recycling property simultaneously. To this end, the design and synthesis of nanocomposites encompassing magnetic have captivated attention amongst the scientific community [140–142]. The composites of ZIF-67 and magnetic materials like Fe$_3$O$_4$ demonstrated some merits. (i) The transition metal ions originated from both ZIF-67 and magnetic metallic material can activate persulfate simultaneously and effectively for the generation of SO$_4^{\bullet-}$. (ii) The controllable atomic ratio of metals can accelerate Co(II) cycling and substantially increase the catalytic rate. (iii) Its separation can be easily performed through the application of external magnetic fields, thus obtaining more efficient, economic and environmentally friendly water purification processes. Cui et al. [134] obtained Fe$_3$O$_4$-PVP@ZIF-67 by rapid microwave synthesis, which reduced the synthesis time greatly. In this system, polyvinyl pyrrolidone (PVP) was an amphiphilic non-ionic polymer to optimize ZIF-67 crystal and functionalize Fe$_3$O$_4$ nanoparticles [143,144]. The SEM images indicated (Fig. 7a) that ZIF-67 exhibited regular dodecahedron morphologies with smooth surface, and the Fe$_3$O$_4$ grew as a round shape with a mean diameter of about 200–300 nm on the surface of ZIF-67. It was noteworthy that saturation magnetization value of Fe$_3$O$_4$-PVP@ZIF-67 (44.4 emu g^{-1}) was much high than that of Co$_3$O$_4$ (9.8 emu g^{-1}), which allowed for easily
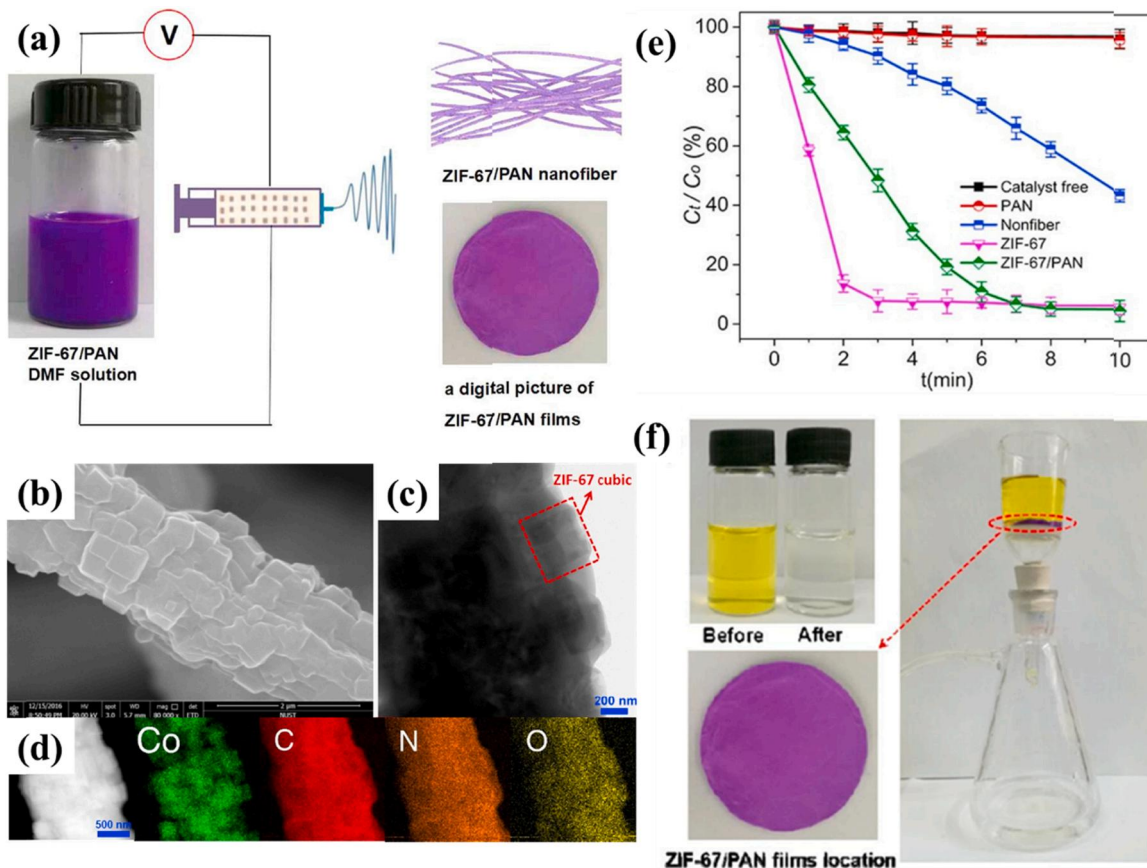
Fig. 2. (a) Illustration of the synthesis route of the ZIF-67/PAN fiber; (b) SEM image and (c) TEM image of ZIF-67/PAN; (d) The elemental mapping of the as-prepared ZIF-67/PAN fiber; (e) The AY degradation efficiencies over different catalysts; (f) Schematic diagram of AY dynamic decolorization over ZIF-67/PAN filters. Reproduced with permission from Ref. [54]. Copyright 2017 Elsevier.

magnetic separation of the material [145]. During the PMS activation reaction process, Fe$_3$O$_4$-PVP@ZIF-67 demonstrated improved degradation performance toward BPF (Bisphenol F) (Fig. 7b). The magnetic Fe$_3$O$_4$-PVP@ZIF-67 catalyst can achieve 85.5% removal efficiency toward BPF up to 4 cycles, which showed the application potential in industrial wastewater[134]. Chen et al. [55] reported an ultrasonic-assisted reverse co-precipitation method to prepare magnetic Fe$_3$O$_4$ @ZIF-67 (Fig. 6c), which was used as a highly efficient PMS activator for TBBPA (tetrabromobisphenol A) degradation. The TBBPA degradation and the TOC removal over the different catalysts in the presence of PMS were illustrated in Fig. 7d and e. It could be observed that the TBBPA degradation efficiency could achieve 100% in ca. 3 min, and a very high TOC removal efficiency (82.5%) was achieved in the Fe$_3$O$_4$ @ZIF-67/PMS system. From the EPR and active substances quenching experiments, a variety of ROSs including SO$_4^{\bullet-}$, •OH and ^{1}O$_2$ were contributed to the degradation in the Fe$_3$O$_4$ @ZIF-67/PMS system, in which the non-radical ^{1}O$_2$ was the dominant one [146–148]. XPS analysis further provided theoretical insights into the diatomic metal sites toward PMS activation [149,150]. The electron-donating capacity of Fe(II) in Fe$_3$O$_4$ for improved the Co(II)/Co(III) transfer, which was responsible for the enhanced catalytic PMS activation performance for producing more ROSs to achieve the TBBPA degradation. Based upon the above discussion, the synergistic effect mechanism was proposed in Fig. 7f. The synergistic catalytic mechanism could be divided into ^{1}O$_2$-dominated non-free radical pathway and radical pathway originated from other active substances. It was expected that the preparation of magnetic materials/ZIF-67 would provide a broader application prospect to recovery catalysts in practical wastewater treatment. In the future research, it is essential to carry out in-depth investigation on the corresponding reaction mechanism and reactor apparatus.

Numerous studies have shown that ternary composites could further improve the catalytic efficiency by providing more effective redox reaction sites, reducing feasible charge recombination, and diminishing reaction activation energy [151,152]. As mentioned above, ZIF-67 is an effective visible light catalyst with a suitable band gap (E_g = 1.90 eV) [153], which could experience the Co(II)/Co(III) redox cycles to activate persulfate to generate SO$_4^{\bullet-}$ [73]. It is well known that graphene oxide (GO) is a two-dimensional star material, which is widely known in different fields due to its unique properties and structures [154,155]. It not only has the function of stabilizing catalyst, but also possesses the oxygen functional groups, which can generate SO$_4^{\bullet-}$ by the activation of persulfate [156]. In addition, Ag nanoparticles (NPs) are considered as the promising potential catalyst candidates because of the high conductivity, antibacterial properties and low cost-effectiveness [117,157]. What will happen after the combination of ZIF-67, GO and Ag NPs spark in PS-AOPs? Kohantorabi et al. [45] proposed an approach to fabricate a novel ternary Ag/ZIF-67 @GO nano-catalyst. ZIF-67 @GO was fabricated by stirring method, and Ag/ZIF-67 @GO was synthesized continuously by decorating Ag NPs on ZIF-67 @GO composite through a simple reduction with sodium borohydride (NaBH$_4$). ZIF-67 was synthesized with a typical rhomboid dodecahedron shape (Fig. 8a) and graphene oxide with abundant functional groups like hydroxyl and carboxyl [158] was coated on ZIF-67 @GO in the form of a thin layer (Fig. 8b). The interplanar spacing of Ag NPs can be visualized by the HR-TEM image as reflected in Fig. 8c. The band gap energy value of Ag/ZIF-67 @GO was just 1.64 eV, lower than those of ZIF-67 (1.91 eV) and ZIF-67 @GO (1.79 eV), which determined the contribution of GO, and Ag NPs on optical properties of ZIF-67 and its capability in the photocatalytic processes [159]. A series of controlled experiments showed that the Ag/ZIF-67 @GO with improved optical properties
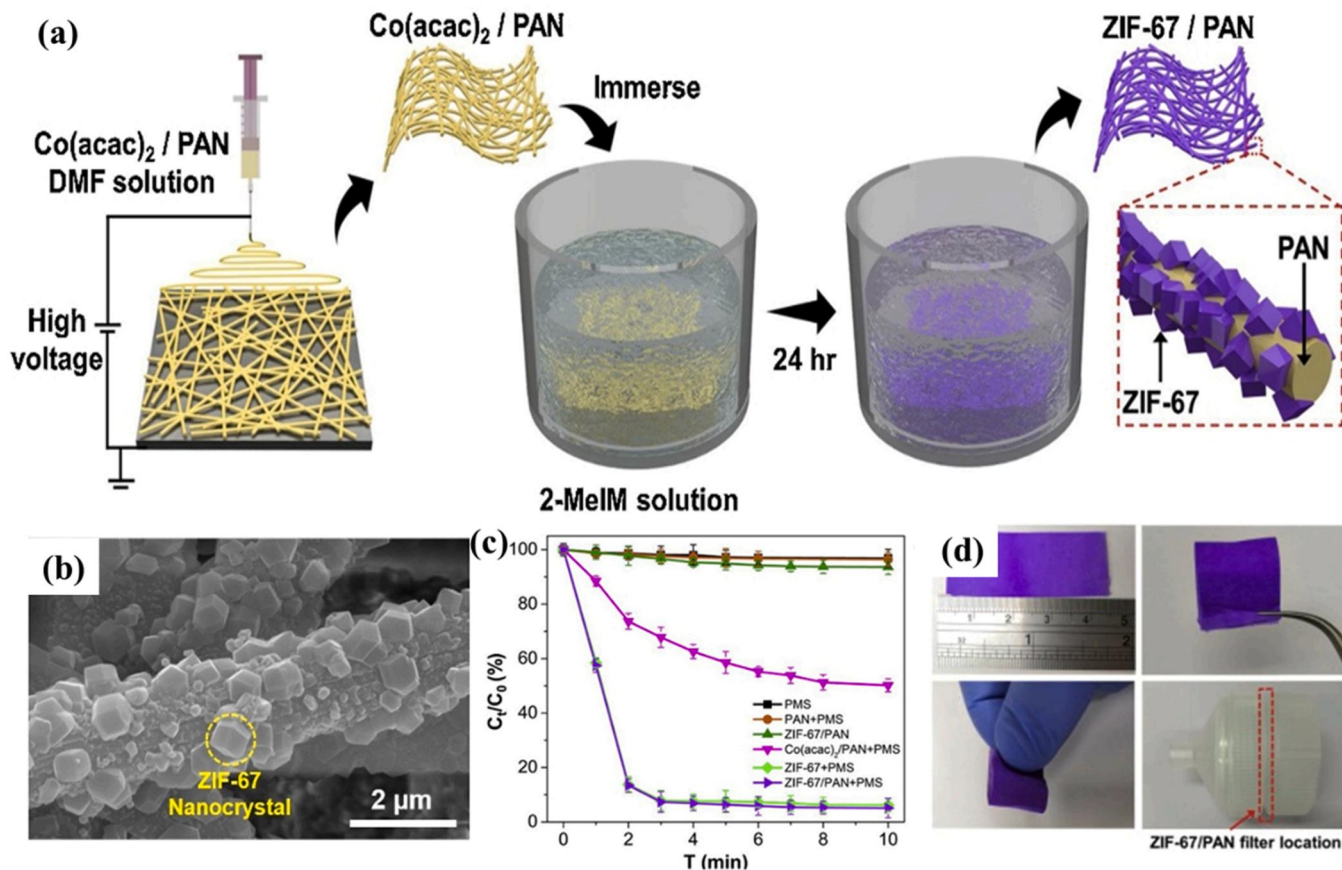
Fig. 3. (a) The schematic illustration of in situ preparation of ZIF-67/PAN filters. (b) The SEM image of ZIF-67/PAN; (c) The AY degradation efficiencies over different catalysts; (d) The images of ZIF-67/PAN filters and Swinnex syringe filter holder. Reproduced with permission from Ref. [47]. Copyright 2020 Elsevier.
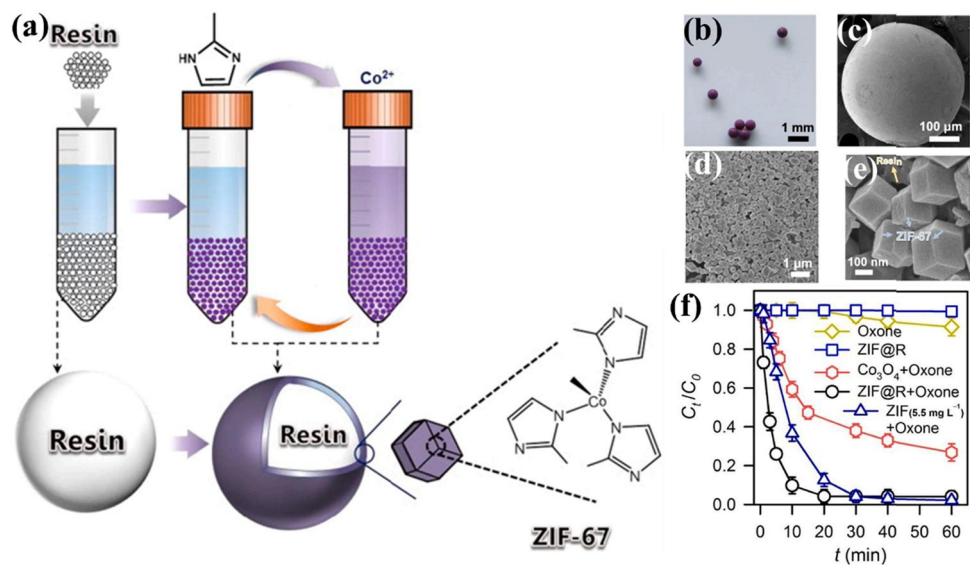

Fig. 4. (a) The synthesis route of macrosphere-immobilized ZIF-67 (ZIF@R) through self-assembly.; (b) The images of ZIF@R; (c), (d) and (e) SEM images of ZIF@R at different magnifications; (f) The RhB removal efficiencies over different conditions. Reproduced with permission from Ref. [53]. Copyright 2018 Elsevier.

provided excellent conditions to achieve enhanced photocatalytic performance toward phenol removal and *E. coli* inactivation in the presence of visible light and PMS (Fig. 8d–e). Upon the irradiation of visible light, PMS could be activated to generate a variety of free radicals [160,161]. More importantly, the light leaded to the generation electrons/holes (e/h$^+$) pairs, and plasmon excited states of Ag NPs [117]. The proposed

mechanism of phenol degradation (Fig. 8f) and *E. coli* inactivation (Fig. 8g) was summarized. (i) The presence of Co(II)/Co(III) circular reaction could accelerate the PMS activation to generate the increasing ROSs. (ii) The introduction of GO enhanced the catalytic activity and boosted the production of radical species. (iii) The construction of heterojunction with AgO and ZIF-67 could facilitate the charge separation
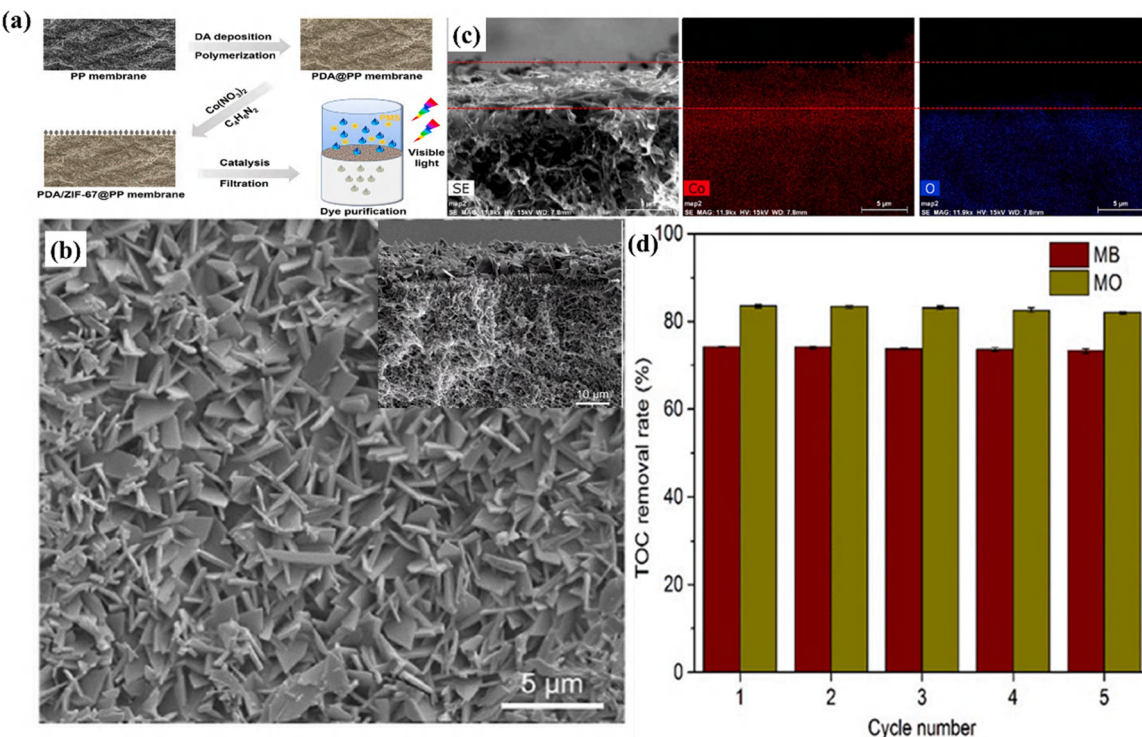
Fig. 5. (a) Preparation and application of PDA/ZIF-67 @PP membrane in dyestuff wastewater treatment; (b) SEM image of PDA/ZIF-67 @PP membrane surface (inset: SEM image of corresponding cross-section). (c) The SEM image of cross-section of PDA/ZIF-67 @PP membrane and corresponding elemental mapping. (f) The TOC removal efficiency of dye wastewater with continuous filtration over visible-light PDA/ZIF-67 @PP/PMS system. Reproduced with permission from Ref. [88]. Copyright 2019 Elsevier.
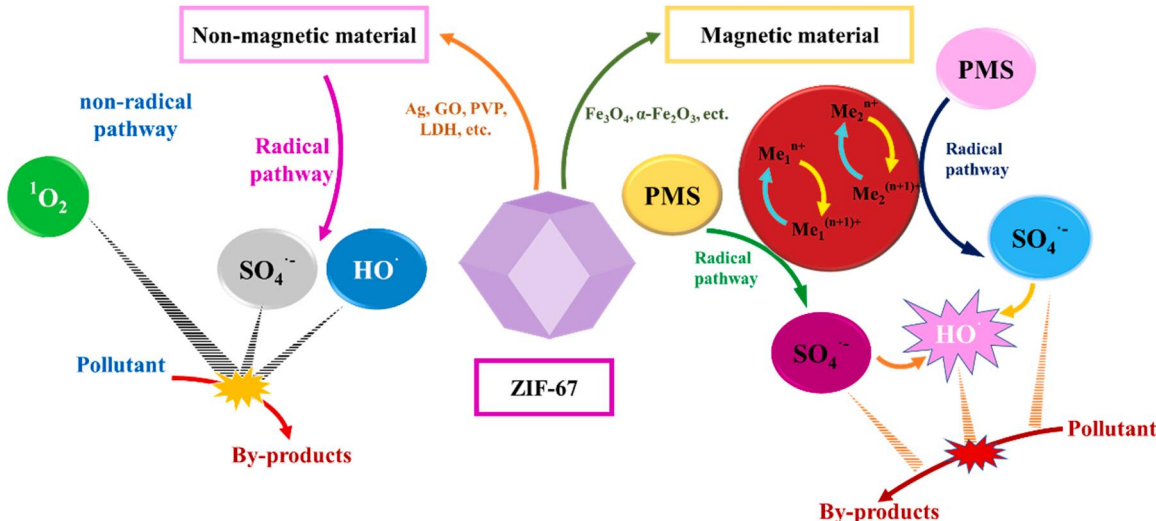
Fig. 6. Schematic diagram of the degradation of contaminants by ZIF-67 composites.

of photo-induced e/h^+. (iv) The photocatalytic activity of the as-prepared catalysts could be enhanced by Ag NPs due to the improved electron transfer capability. It was believed that •OH, $SO_4^{•-}$, h^+, $•O_2^-$, and Ag worked together on the *E. coli* inactivation. This work afforded an approach for enhancing the photocatalytic activation persulfate performance via the rational combination of ZIF-67, GO and Ag NPs. In addition, this research provided a sample that ZIF-67-based composites could accomplish both organic pollutant and bacteria degradation and afford the detailed mechanistic investigations for the primary reaction pathways from PMS activation.

2.3. ZIF-67 derivatives for PS-AOPs

In recent years, the booming development of MOFs-derived materials with improved stability, conductivity, and well-inherited characteristics has also opened new opportunities and possibilities for MOFs-based materials in water treatment applications. The approaches for the preparation of MOF derivatives are multitudinous, which can be classified as (i) direct one-step pyrolysis, (ii) staged heat treatment method, (iii) pyrolysis combined pre-treatment/post-treatment method, (iv) vulcanization and (v) phosphating. Our group has also fabricated a range of MOFs-derived materials for sewage treatment, such as ZnS
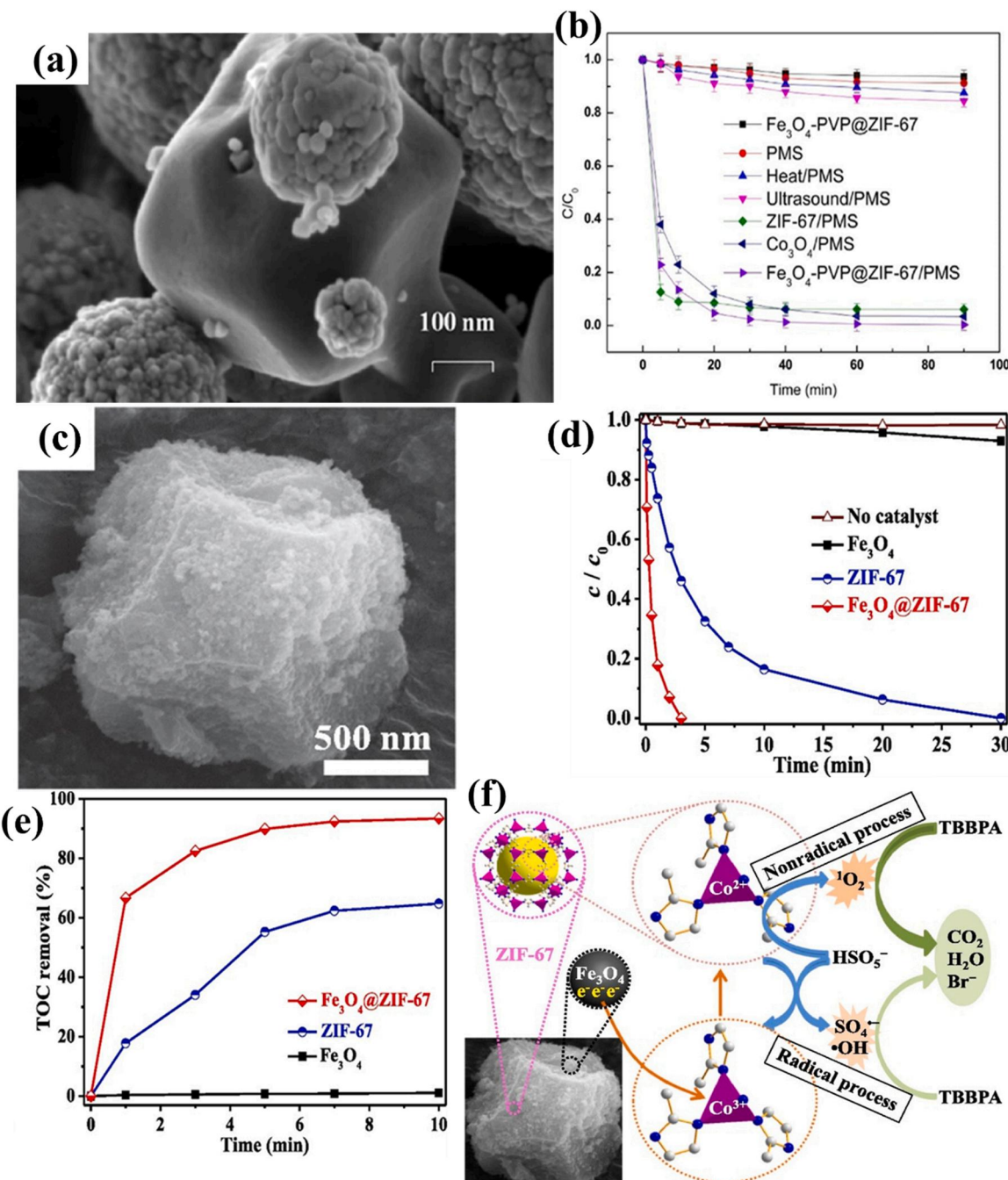
Fig. 7. (a) The SEM image of as-prepared Fe_3O_4-PVP@ZIF-67; (b) The BPF degradation efficiency over different catalytic system. [134] Copyright 2021 Elsevier. (c) SEM images of Fe_3O_4@ZIF-67; (d) The TBBPA degradation over No catalyst, Fe_3O_4, ZIF-67 and Fe_3O_4@ZIF-67 by the activation of PMS; (e) The TOC removal efficiency during the TBBPA decomposition process; (f) Synergistic catalytic mechanism over Fe_3O_4@ZIF-67-PMS system for the TBBPA removal. Reproduced with permission from Ref. [55]. Copyright 2021 Elsevier.

obtained from rod-like ZIF-L [162], $Cd_{0.5}Zn_{0.5}S$ obtained from ZIF-8 [163], In_2S_3 derived from MIL-68 [164], TiO_2/MIL-125 Core-Shell composite derived from MIL-125 [165], immobilized Fe_3O_4 derived from MIL-88A(Fe) [76], CoS_x@SiO_2 nanocages obtained from ZIF-67@SiO_2 [48] and Fe_3S_4 derived from MIL-100(Fe) [145], which all exhibited excellent water stability, electrical conductivity and contaminant degradation properties. Compared with ZIF-67, most ZIF-67 derived materials possess the characteristics of the larger number of active sites, the faster contaminants mass transfer rate, and the faster Co (II)/Co(III) cycle efficiency [166,167]. Thanks to these properties, research focusing on the synthesis and PS-AOPs application of ZIF-67 derivatives have sprung up. Therefore, as shown in Table 4, the

derivatives of ZIF-67 have been extensively studied as catalysts for heterogeneous PS-AOPs reactions with certain modifications. In this section, we introduced ZIF-67-derived cobalt-based metal oxides and their hybrid materials, cobalt-carbon and their hybrid materials, cobalt sulfide and their hybrid materials for PS-AOPs, respectively (Fig. 9).

2.3.1. Cobalt-based metal oxides and their hybrid materials

Direct calcination in air can reduce the cost of catalysts preparation, which is used conveniently and economically to develop valuable metal oxides hybrids [212]. Pu et al. [46] used three Co-MOFs as templates to synthesis three kinds of Co_3O_4 for RhB degradation via PMS activation. These three Co_3O_4 catalysts were prepared by two-step heat treatment,
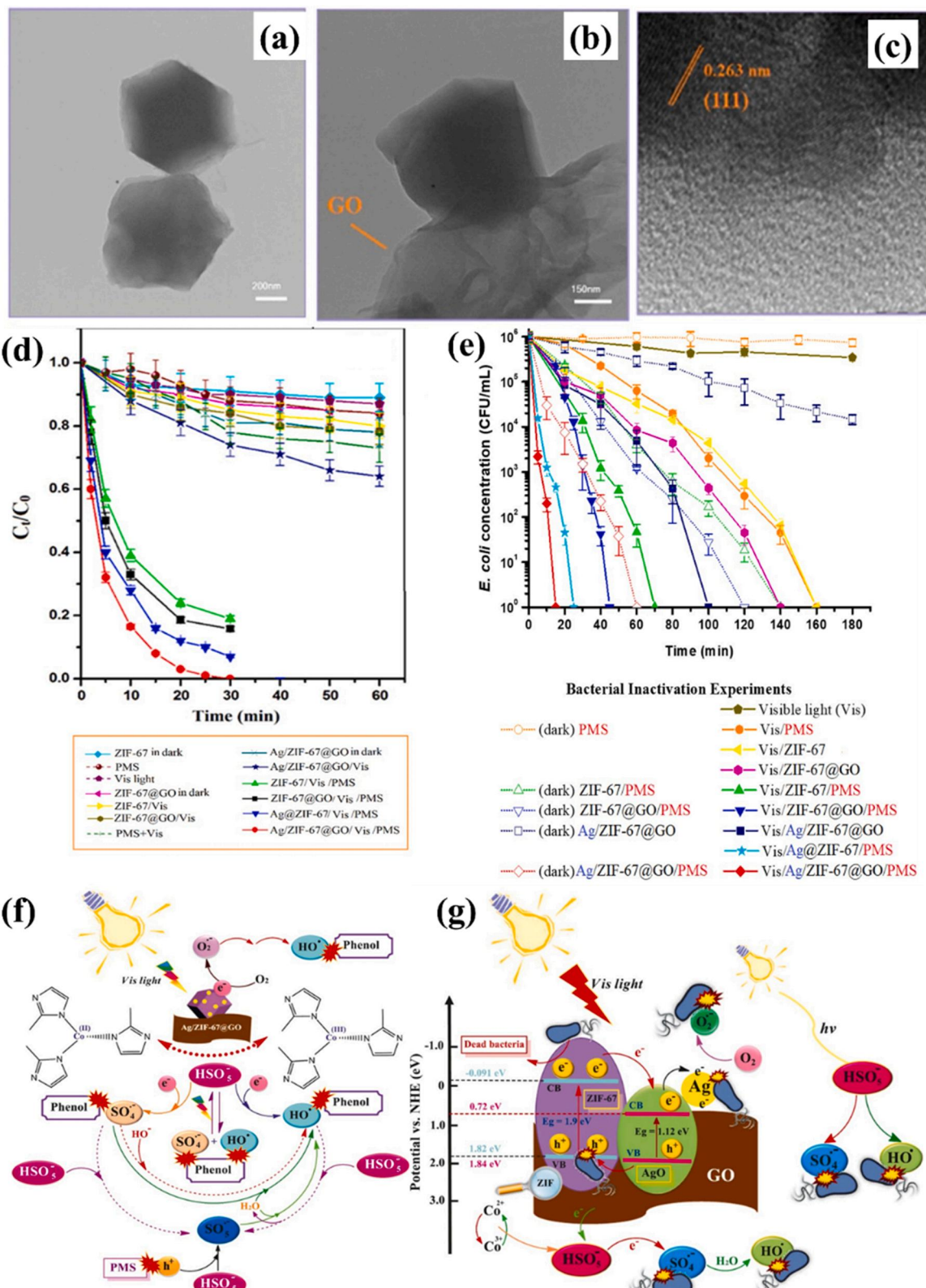
Fig. 8. TEM of ZIF-67 (a) and ZIF-67 @GO (b); HR-TEM image of Ag/ZIF-67 @GO (c); (d) Phenol degradation in the presence of different catalytic conditions under dark or visible light irradiation; (e) Photo-catalytic *E. coli* inactivation by using the different synthesized nanocomposites; (f) The proposed mechanism of phenol decomposition in the presence of Ag/ZIF-67 @GO catalyst using PMS as oxidant under Vis-light irradiation; (g) Proposed mechanism of *E. coli* inactivation in the presence of Ag/ZIF-67 @GO nanocomposite and PMS as oxidant under visible light irradiation. Reproduced with permission from Ref [45]. Copyright 2021 Elsevier.
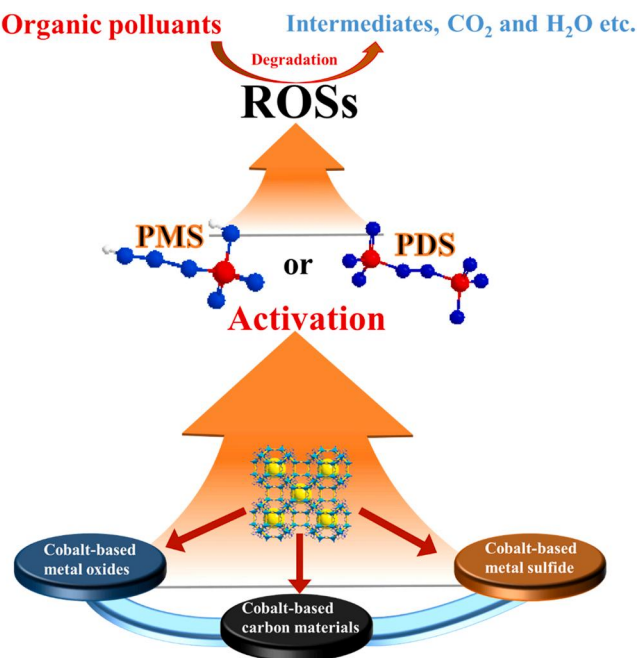
Fig. 9. Schematic diagram summarizing the main contents of ZIF-67 derivatives for PS-AOPs.

in which the ZIF-67 derived Co_3O_4 displayed the optimal RhB degradation efficiency with very low cobalt ion dissolution. The metal oxides nano-catalyst performance typically relies on its specific surface area, morphology, and structure [213]. Muhammad et al. [168] reported a tannic acid etching method to synthesize hollow ZIF-67 (HZIF-67), which was used as the precursor for the preparation of hollow Co_3O_4/C (HCo_3O_4/C) as depicted in Fig. 10a. The enhanced PMS activation performance for bisphenol A (BPA) degradation was observed on HCo_3O_4/C (Fig. 10b), which was attributed to its unique hollow structure (Fig. 10c–d) with a large surface area and abundant active sites. The optimized structure of 3D HCo_3O_4 nanoparticles with a diameter ca. 6–12 nm were well dispersed in supporting hollow carbon derived from ZIF-67 (Fig. 10d). In addition, the hollow structure can favor the mass transfer driving as well as speeding up the chemical reaction. The degradation is driven by $SO_4^{\bullet-}$ and the potential mechanism is shown in Fig. 10e. This work provided a new prospect to deeply optimize the structure of ZIF-67 derivatives for the purpose of improving the catalytic efficiency.

The adjustment of the types of ROSs generated in persulfate activation could be an effective method to further improve the performance of catalysts [214,215]. Singlet oxygen ($^1O_2$) with much stronger oxidation ability than ground state oxygen, has attracted considerable interests in recent decades as a result of its significance in the oxidation removal of contaminants. The preference $^1O_2$ for electrophilic addition or electron-withdrawal reactions with unsaturated organic molecules suggested that the enhanced catalytic property might be improved from the target-selectivity of $^1O_2$ [216–218]. It has been reported that the generation of singlet oxygen can be positively promoted by the existence of oxygen vacancies (O_V) [219]. The decoration of heteroatoms is a
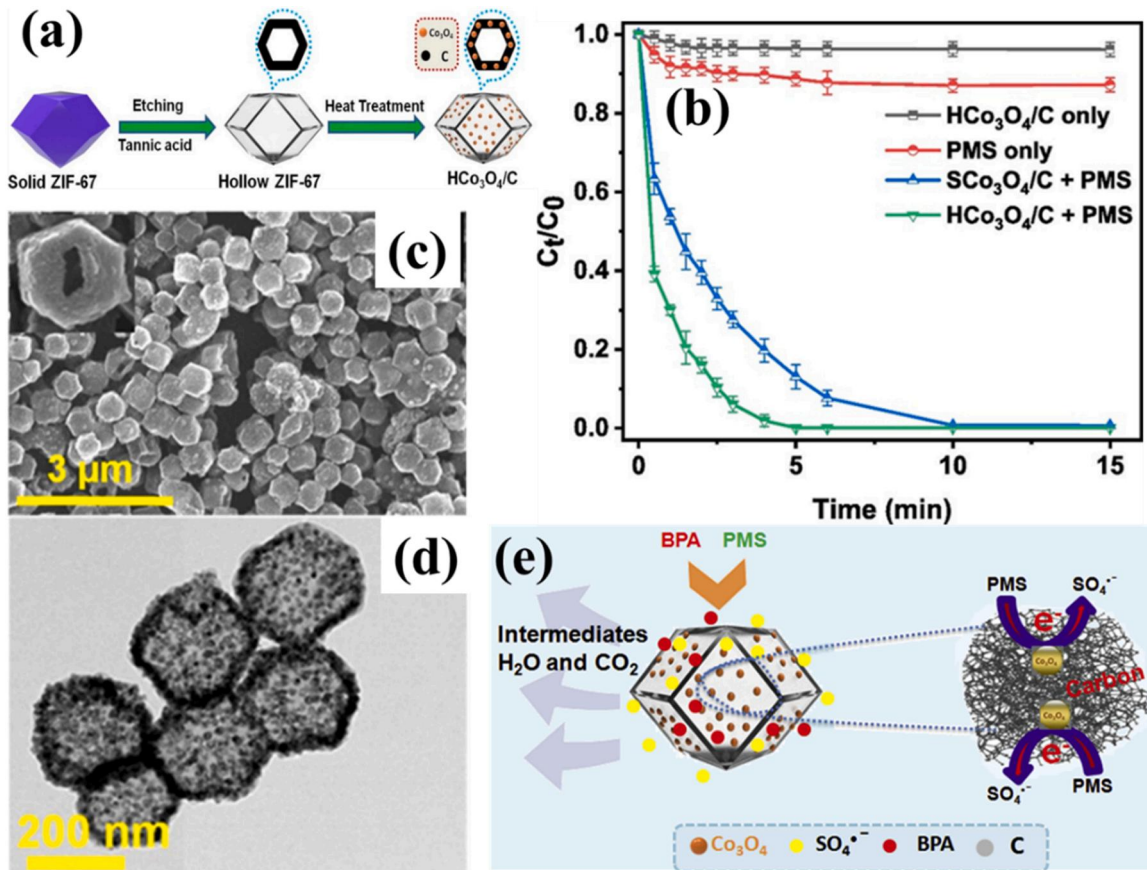
Fig. 10. (a) The schematic illustration of the preparation route of the ZIF-67, Hollow ZIF-67, and HCo_3O_4/C; (b) BPA degradation efficiency under different reaction systems within 15 min. SEM and TEM images of HCo_3O_4/C (c) and HCo_3O_4/C (d); (e) The possible degradation mechanisms of BPA in HCo_3O_4/C. Reproduced with permission from Ref. [168]. Copyright 2019 Elsevier.

useful strategy to adjust the electronic structure of materials and contribute to the appearance of O_V [220,221]. As a representative sample of cobalt-based MOFs, the cobalt atom in ZIF-67 could be substituted by Zn atom without affecting its crystal structure, allowing the convenient preparation of Zn-doped ZIF-67 [222]. Zn-doped ZIF-67 can be readily converted into porous Zn-doped Co_3O_4 by calcination and remarkably change the types of oxygen atoms in Co_3O_4 [223]. Zhao et al. [170] prepared porous $ZnCoO_x$ nanoparticles (Fig. 11a) by calcining Zn-doped ZIF-67 to drive a PMS activation for catalytic degradation of RhB. The results revealed that the as-prepared $ZnCoO_x$ samples presented improved catalytic performance than the CoO_x-ZD (ZIF-67 derived). The optimal $ZnCoO_x$-2 could achieve superior RhB removal efficiency (100 %) within 10 min to CoO_x-ZD (32.1%) (Fig. 11b), indicating that the introduce of Zn could significantly enhance the catalytic performance for PMS activation. The generation of $^1O_2$ might come from the O_2 being activated by O_V. The catalytic property of $ZnCoO_x$ samples was related to the level of O_V and the O_V of $ZnCoO_x$ could be changed by adjusting Zn doping content. In this work, the XPS results revealed that Zn doping could improve the amounts of O_V in $ZnCoO_x$ samples. As well, the BET surface area of $ZnCoO_x$ is much larger than that of CoO_x, which might support more catalytic active sites. By quenching experiments and electron paramagnetic resonance (EPR) measurements verified that both $^1O_2$ as the primary ROS and $SO_4^{\bullet-}$ contributes to organic pollutants degradation. The O 1 s spectrum belonged to $ZnCoO_x$-2 (Fig. 11c) showed that the content of oxygen in the lattice (O_L) declined from 25.4% to 16.3% meanwhile the level of O_V raised from 54.9% to 67.9% after the reaction, indicating the oxygen

atoms in $ZnCoO_x$-2 participate in the PMS activation. Based on the above-mentioned discussion, the degradation mechanism dominated by singlet oxygen is revealed in Fig. 11d. This work suggested that the rational decoration of O_V could improve the properties of heterogeneous catalysts for persulfate activation, which will bring new insights to the research and development of metal ion-doped materials as persulfate activators.

In recent years, the mediated electron transfer mechanism was investigated in persulfate activation systems [224]. There are many advantages of the mediated electron transfer mechanism systems, such as the adaptability to diverse initial organics and inorganics in the environmental background [225], the full utilization of oxidizing capacity of oxidizer and the avoidance of self-quenching of free radicals caused by propagation reaction. However, the researches on non-radical oxidation are mainly focused on carbon materials [226]. The applications of metal oxides in non-radical oxidation are still relatively few. Wang et al. [57] designed a $Co_3O_4/NiCo_2O_4$ double-shelled nanocage catalyst derived from ZIF-67 to decompose BPA through PDS-catalyst composite by mediated electron transfer mechanism. It was observed that $Co_3O_4/NiCo_2O_4$ DSNCs possessed a special box-in-box structure with hollow core (Figs. 12a–b), and the elements of Co and O enhanced apparently in the center, whereas Ni was only distributed in the outer shell layer (Figs. 12c–f). During the catalysis reaction process, both the $NiCo_2O_4$ of outer shell and the Co_3O_4 of inner shell were involved in the activation reaction of PDS, which notably accelerated the removal of BPA (Fig. 12g). The results of radical quenching experiments revealed that no obvious $SO_4^{\bullet-}$ or $\bullet OH$ was generated during activation of PDS by
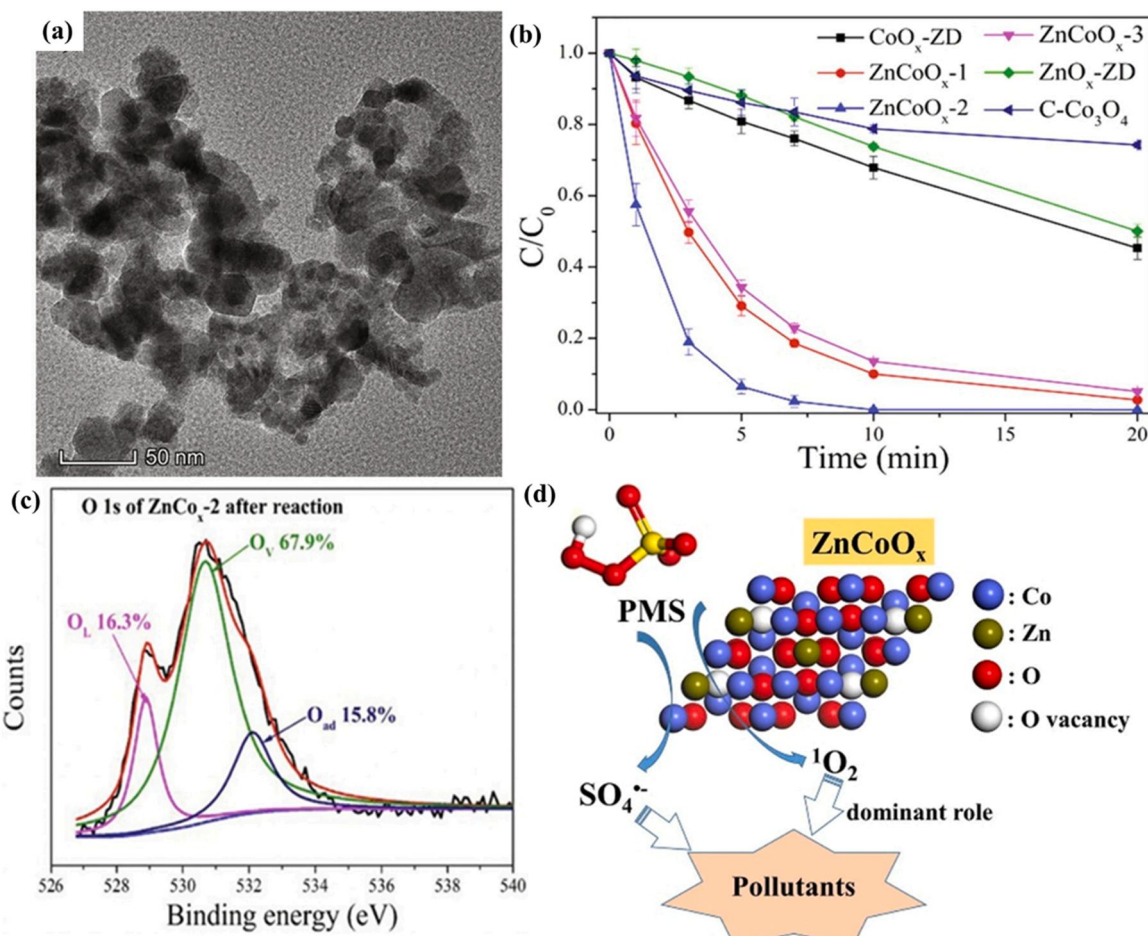

Fig. 11. (a) The TEM images of $ZnCoO_x$-2; (b) The RhB degradation by the activation of PMS over different catalysts (CoO_x-ZD, $ZnCoO_x$-1, $ZnCoO_x$-2, $ZnCoO_x$-3, ZnO_x-ZD, and C-Co_3O_4); (c) O 1 s spectrum of $ZnCoO_x$-2 after the reaction. (d) The proposed mechanism for degradation toward RhB over $ZnCoO_x$/PMS system. Reproduced with permission from Ref. [170]. Copyright 2021 Elsevier.
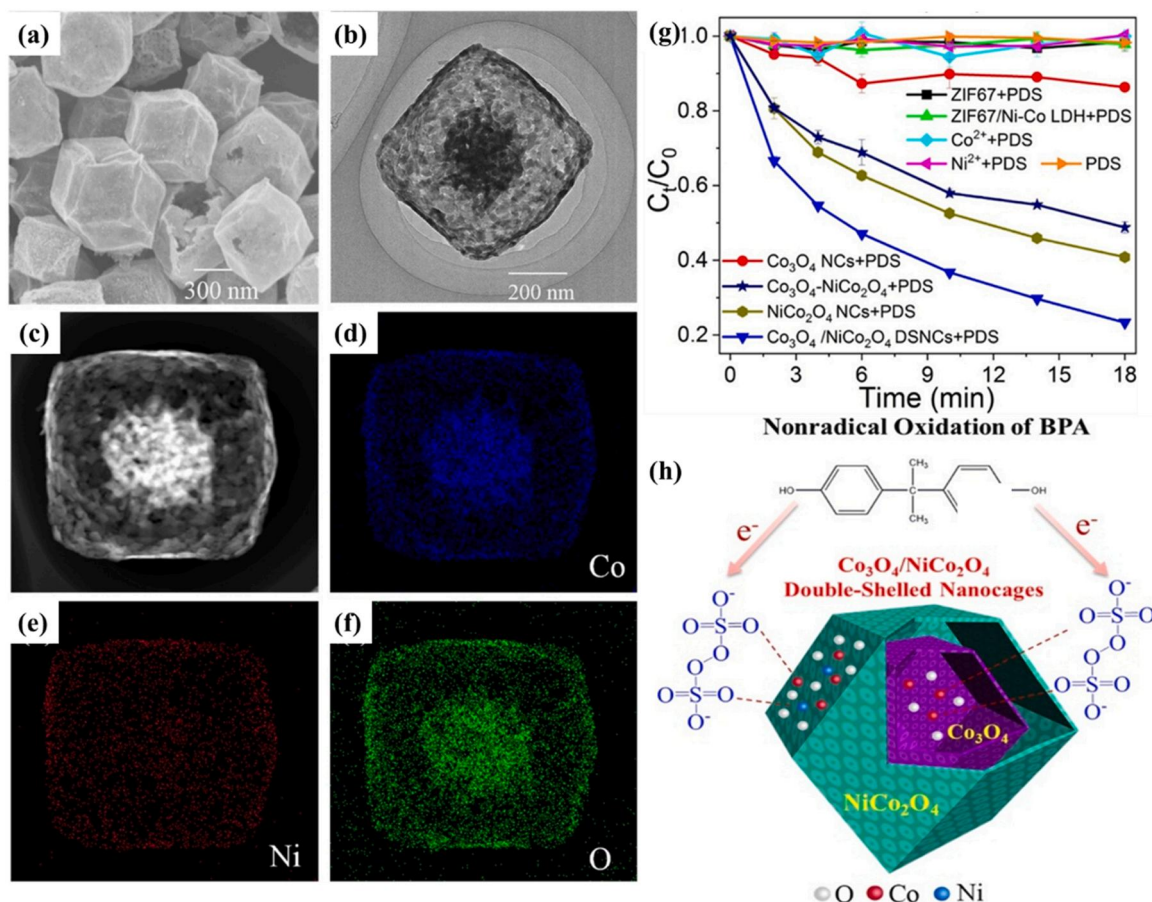
Fig. 12. (a) SEM image of $Co_3O_4/NiCo_2O_4$ DSNCs; (b, c) TEM images of $Co_3O_4/NiCo_2O_4$ DSNCs; and elemental mapping of (d) Co; (e) Ni and (f) O; (g) The degradation efficiency of BPA over different catalytic system; (h) Schematic illustration of catalytic mechanism for degradation of BPA over $Co_3O_4/NiCo_2O_4$ DSNCs + PDS system. Reproduced with permission from Ref. [57]. Copyright 2021 Elsevier.

the as-prepared $Co_3O_4/NiCo_2O_4$ DSNCs. The EPR spectra proved the oxidants formed by the $Co_3O_4/NiCo_2O_4$ DSNCs and PDS, instead of $SO_4^{\bullet -}$, $\bullet OH$ or $^1O_2$, drove the BPA degradation. The mediated electron transfer mechanism was further evidenced by the in-situ Raman spectroscopy, electrochemical impedance spectroscopy (EIS) and liner sweep voltammetry (LSV) results. [227,228]. The unaltered chemical states of Co and Ni reflected from the fresh and used catalysts' XPS spectrum also demonstrated proposed electron transfer oxidation mechanisms. As expected, the mechanism for BPA degradation over $Co_3O_4/NiCo_2O_4$ DSNCs and PDS system was illustrated in Fig. 12h. The PDS-catalyst composites were generated in shells of the inner and outer of $Co_3O_4/NiCo_2O_4$ DSNCs. The formed compound on the inner and outer shells had a robust electronic extraction property and withdrew electrons from BPA. The BPA molecular was rapidly decomposed, and the PDS was transformed to SO_4^{2-} and released from the compound. This study prepared an innovative PDS system for non-radical oxidation, shedding light on the development of ZIF-67-based PS-AOPs technology.

2.3.2. Carbon materials and their hybrid materials

Although PDS/PMS can be efficiently activated by metal-based materials via the way of one-electron reduction, there are still many limitations in the popularization of practical application, such as the toxicity of leaching metal, the decline of catalytic efficiency because of nanoparticles' aggregation and the highly pH-dependency [63,229]. Carbon materials as emerging and green catalysts have received great concern in the field of PS-AOPs [230]. Especially in lately years, various carbon materials like nanodiamonds [231], nanotubes [232], biochar [233], GO [234] and Carbon-based single atom catalyst [235] have been

explored as effective and green catalysts for activating persulfate. ZIF-67 as a genetic template can be derived into different carbon materials, heteroatom-doped carbon materials and carbon materials with Co particles, which exhibited outstanding performance for PDS/PMS activation.

As one of the most remarkable families of materials, carbon nanotube (CNT) with sp^2 hybrid carbon configuration [236], abundant and regular tubular microstructure and superior electronic conductivity have generated great interest in energy storage and conversion as well as environmental catalysis [237]. Recently, there have been many studies using CNT as an effective catalyst for the activation of persulfate [238, 239]. Moreover, the N-doped CNT showed the enhanced catalytic performance [240]. Recent research indicated that calcination of ZIF-67 in the atmosphere of H_2 was an effective approach to synthesis CNT, which had the characteristics of high graphitic degree and be favorable for electron transfer [50]. Ma et al. [146] prepared N-doped carbon nanotubes frameworks (NCNTFs) through the method of in-situ calcination of ZIF-67 in the presence of N_2/H_2 and etched in H_2SO_4 (Fig. 13a). In the process of preparation, cobalt could act as an effective catalyst for the generation of CNTs. Compared to traditional nitrogen-doped carbon materials derived from metal-organic frameworks, the emergence of intertwined carbon nanotubes exhibited an optimized mesoporous structure affirmed from SEM (Fig. 13b) and TEM figures (Fig. 13c), which facilitated the diffusion of reactants and mass transfer. The HR-TEM (Figs. 13d–g) showed that the as-prepared NCNTFs with remaining Co nanoparticles were wrapped tightly by a successive graphitic carbon layer. Small cobalt nanoparticles were encapsulated by abundant fluffy mesopores and a large number carbon nanotubes root,
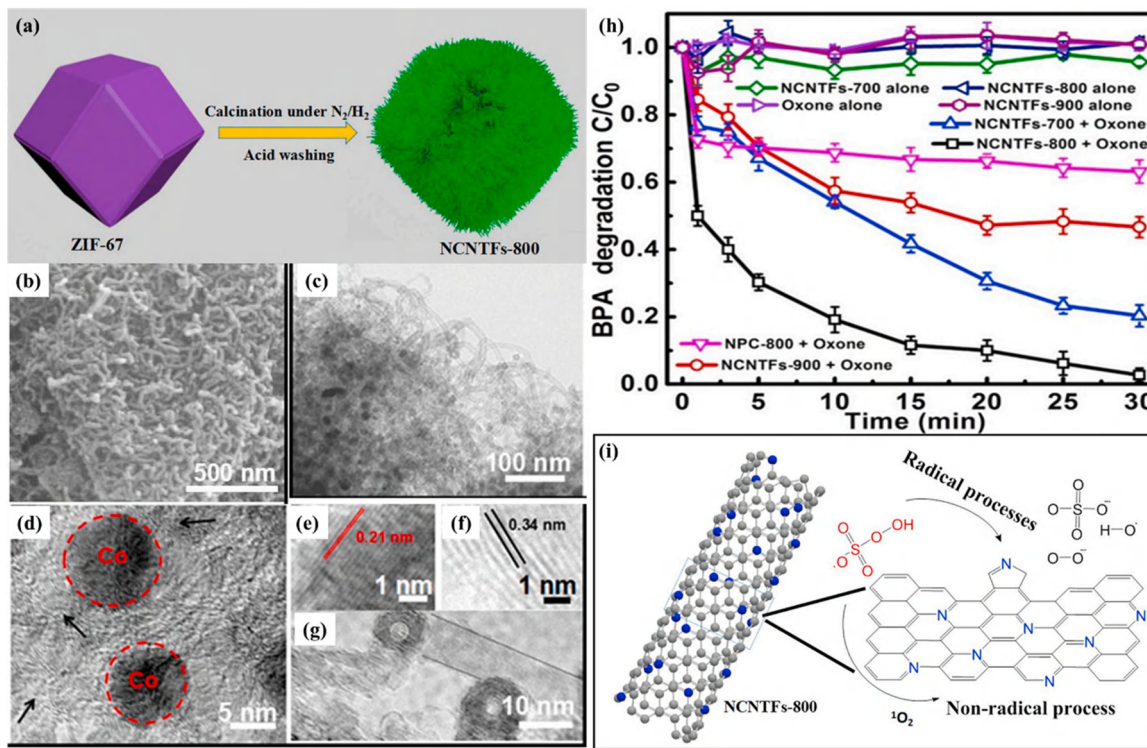
Fig. 13. (a) The schematic synthesis procedures of NCNTFs-800. (b) The SEM image of NCNTFs-800; (c) TEM and (d, e, f and g) HRTEM of NCNTFs-800. (h) Degradation of BPA by different catalysts by the activation of Oxone; (i) The non-radical and radical degradation mechanisms in PMS activation over NCNTFs-800. Reproduced with permission from Ref. [146]. Copyright 2018 Elsevier.

which could inhibit the leaching of cobalt ions [241]. And more catalytic active sites could be produced due to the formation of intimate bonds such as CoN$_x$ and Co-N-C in the result of the interaction of residual Co with neighboring nitrogen, carbon or oxygen atoms [242]. The authors applied it to BPA degradation with the aid of PMS. The experimental results illustrated that NCNTFs-800 was the optimal catalyst to achieve 97.3% degradation of BPA (Figs. 13h) and 62.9% of TOC removal efficiency, which could be attributed to its optimized balance between graphitization degree and graphitic nitrogen content (total nitrogen content × graphitic N proportion). The results of radical quenching experiments manifested that BPA molecular decomposition mainly depended on the engagement of $^1O_2$ in the non-radical reaction pathway. Nevertheless, the conventional $SO_4^{\bullet-}$, $\bullet OH$ and $\bullet O_2^-$ only played the auxiliary functions in the sulfate radical-advanced oxidation process (SR-AOPs), which could also be verified by electron paramagnetic resonance (EPR). In addition, to demonstrate the role of non-free radicals in the process of BPA oxidation, the activation of H_2O_2 and PDS by NCNTFs-800 were performed. As it turned out, the degradation efficiencies of NCNTFs-800 coupled with H_2O_2 or PDS were inferior to NCNTFs-800/PMS system. The density functional theory (DFT) calculations suggested that the PMS absorbed on sp^2-conjugated carbon network was inclined to arouse non-radical oxidation reaction [243]. Therefore, as shown in Fig. 13i, the catalysis mechanism could be ascribed to the cooperative effect of the active substance oxidative and electron-conductive properties, which accelerates the degradation of BPA. Based on the above discussion, CNTs-based materials become a desirable activator to promote the decomposition of organic contaminants in the PS-AOPs.

Recently, yolk-shell nanoparticles (YSNs), similar to the biological structures of the cell wall and cell membrane, have been considered as an ideal material for sensor, energy-storage, adsorption and catalysis [244–247]. As the sacrifice template of core/yolk-shell nanoparticle, ZIF-67 has great potential in selective removing of organic pollutants. Zhang et al. [58] prepared yolk-shell carbon/cobalt nanoreactors

(YSCCN) derived from ZIF-67, in which the size exclusion and confinement effect of YSCCN were focused studied. During the preparation of the material, YSCCN was synthesized by a simple and ingenious method of calcination after controlled etching (Fig. 14a), in which tannic acid (TA) was an etching agent. Solid Co/C nanoparticles (SCCNs) and hollow Co/C nanoparticles (HCCNs) were synthesized by no etching and etching for longer periods of time. The SEM and TEM characterizations affirmed that the perfect yolk-shell structure was maintained well (Fig. 14b–d). The elemental mapping with line scan, the enlarged TEM image and HR-TEM images are illustrated in Figs. 14e–g, which further demonstrated the existence of C (graphitic carbon), Co and N elements and the lots of favorable pores for emergence of active sites and mass transfer [143]. During the testing of catalytic performance, the strong catalytic selectivity was shown in YSCCNs + PMS system. It was worth to highlighting that YSCCNs preserved the outstanding degradation capability with the introduction of humic acid (HA) (Fig. 14h), one of the ubiquitous natural organic matters (NOMs) that could severely block the active sites on the catalyst and thus reduce the catalytic performance [248]. Whereas, the catalytic performance decreased dramatically when HA was added both in SCCNs + PMS and HCCNs + PMS systems (Figs. 14i–j). The differences in degradation efficiency could be accounted for the unique core/yolk-shell of YSCCNs, where the NOMs and target pollutant were insulated into two independent regions. This phenomenon could be described as a size-exclusion effect, in which the macromolecules were intercepted and the small molecules can traverse. It was significant implication for the selective degradation of organic pollutants [249]. The confinement effect was also confirmed via the degradation of phenol and 4-chlorophenol (4-CP), the size of which is less than the pore dimension on the shell of YSCCNs. To investigate the degradation mechanism, the quenching experiments, EPR experiments and aromatic hydroxylation of benzoic acid were carried out. The detailed degradation mechanism in Fig. 14k suggested that radicals played the dominated role in the degradation progress. In summary, this work provided a new perspective for the selective degradation complex
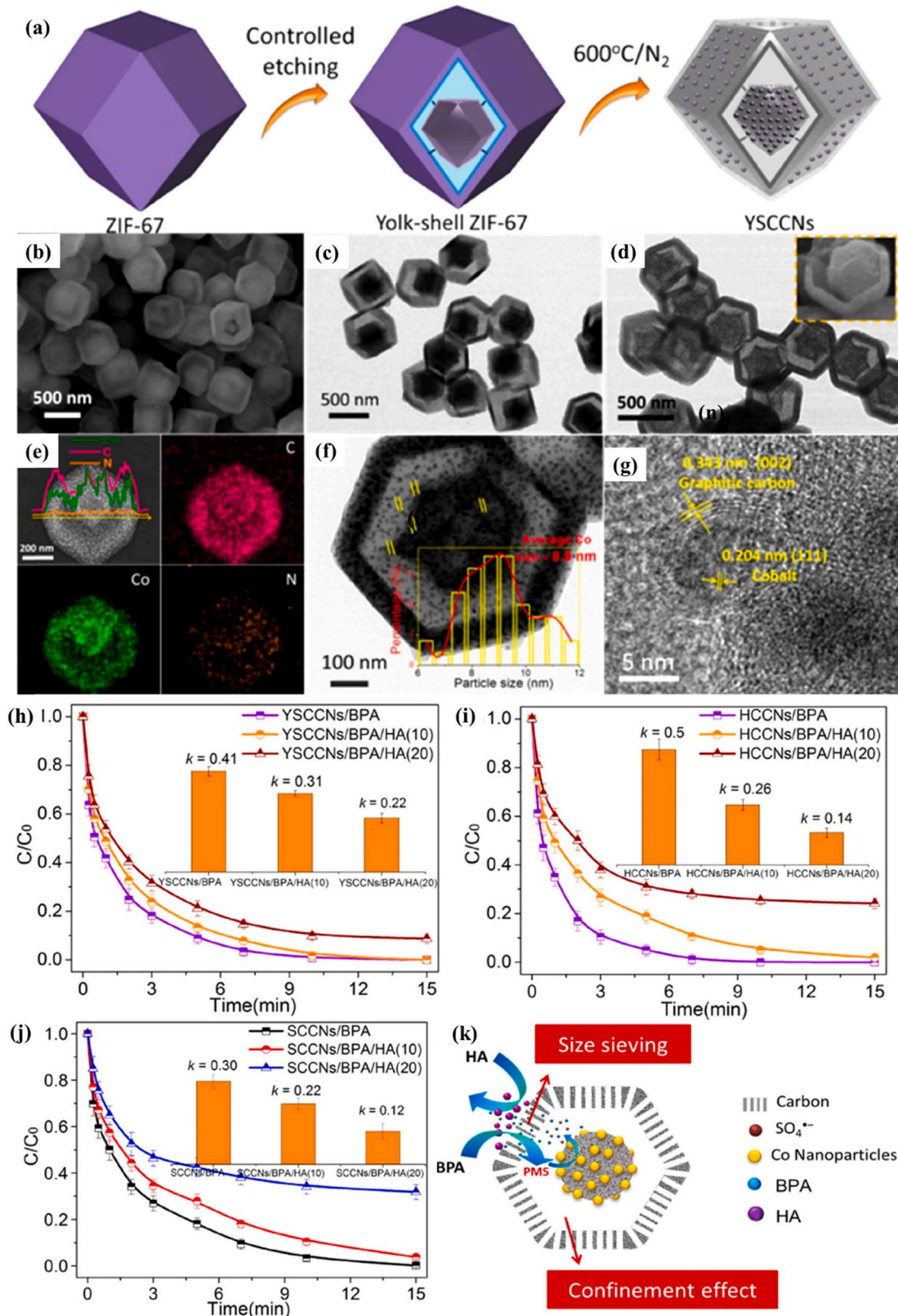
Fig. 14. (a) The schematic synthesis procedures of the YSCCNs; (b) SEM image and (c) TEM image of yolk–shell ZIF-67; (d) TEM image of YSCCNs and top-right inset in (d) the SEM image of broken structure of YSCCNs; (e) the line scan and element mapping of YSCCNs; (f) the enlarged TEM image and the size distribution profile of Co nanoparticles; (g) high-resolution TEM image of YSCCNs; The BPA degradation efficiency of YSCCNs (h), HCCNs (i), and SCCNs (j) in HA system and without HA system, respectively; (k) Schematic illustration of selective removal mechanism of YSCCNs. Reproduced with permission from Ref. [58]. Copyright 2020 American Chemical Society.

and refractory organic pollutants in water remediation.

2.3.3. Cobalt sulfide and their hybrid materials

Cobalt sulfide is an important semiconductor material, which had been widely studied in the fields of lithium-ion batteries, water decomposition electrocatalysts and supercapacitors [250–252]. Their effective recycling of Co^{3+}/Co^{2+} and S^{2-}/S_2^{2-} achieved them to be greatly potential in AOPs field [253]. ZIF-67 can be derived from cobalt sulfide by adding sulfur sources like thioacetamide and thiourea [254]. Zhu et al. [211] prepared novel graphene-immobilized cobalt sulfide nano-catalysts (CoS@GN) via a ZIF-67-templated ligand exchange route and used it to degradation BPA by activating PMS. As illustrated in Fig. 15a, the synthesis process was mainly divided into three steps: (i) preparation of ZIF-67 @GN; (ii) preparation of Co_3S_4 @GN-x (x = 10–60 in accordance to the graphene oxide weight); and (iii) preparation of CoS@GN-x by the thermally induced phase conversion of Co_3S_4 @GN-x. The graphene nanosheet (GN) was served as the support since it could (i) inhibit excessive MOF self-assembly and supply abundant sites for the growth of highly dispersed cobalt sulfide nanoparticles [255–257], (ii) enrich BPA from bulk aqueous solution by providing adsorption regions through π-π interaction, resulting in a high local concentration of reacting substance [258], (iii) ensure the efficient electron transport between $SO_4^{\bullet-}$ and adsorbed BPA molecules to improve the reaction efficiency [259]. The SEM images confirmed that Co_3S_4 and CoS nanoparticles were homogeneously immobilized on graphene surfaces (Fig. 15b–c). The degradation results revealed that the BPA removal rate was 1–2 orders of magnitude higher than the majority of reports (Fig. 15d). To investigate the potential contribution of the conductivity of GN, the EIS was performed and the semicircle of Nyquist plots radius of CoS@GN-based electrodes was relatively smaller than that of CoS and Co_3S_4 @GN, manifesting that the charge transfer efficiency of CoS was increased after the addition of graphene and pyrolysis treatment. The radical species quenching experiments revealed that surface-bound sulfate radicals played a primary role in the BPA degradation. Whereas, no ·OH was involved, which was also evidenced by electron paramagnetic resonance (EPR) tests, potentiometric titration and density functional theory (DFT) calculation. Based on the above analyses, the mechanism was presented in Fig. 15e. Firstly, the generation vast $SO_4^{\bullet-}$ was through the activation of PMS. Secondly, the $SO_4^{\bullet-}$ conjugated to the CoS surface by electrostatic force and then quickly decomposed BPA molecules with graphene as the conductor. To test the recycling ability, the authors constructed a membrane reactor (Fig. 15f) to achieve the high degradation efficiency in three runs (Fig. 15g), indicating the satisfied recyclability of CoS@GN-60. In all, the graphene-immobilized cobalt sulfide nano-catalysts could produce surface-bound radicals for the quick degradation of BPA, which could be considered as a promising candidate for wastewater remediation due to its excellent catalytic properties and reliable reusability.

To prevent the Co leaching and maintain the original shape of MOFs after derivatization, Wang et al. [48] reported that the amorphous CoS_x @SiO_2 nanoparticles were hydrothermally prepared through sulfurizing ZIF-67 @SiO_2 with the aid of thioacetamide (TAA) (Fig. 16a). In the process of synthesis, the presence of SiO_2 shell in the catalyst not only could inhibit the cobalt leaching to enhance the stability but also could maintain the original shape of MOFs after derivatization. Compared with the conventional metal sulfide materials derived from metal-organic frameworks, the amorphous CoS_x @SiO_2 nanocages possessed a two-shelled hollow nanocages structure which was favorable for the diffusion of organic pollutants revealed from SEM, TEM and EDS elemental mapping figures (Fig. 16b–f). The BET test showed that the as-prepared CoS_x @SiO_2 exhibited a considerable specific surface area and mesoporous structure, which could provide more reaction active sites to degrade organic pollutants. Besides, sulfamethoxazole (SMX) was chosen as a contaminant model to evaluate the catalytic property in the presence of both CoS_x @SiO_2 and PMS. The control experiments illustrated that 100% SMX was degraded within 6 min over

CoS_x @SiO_2/PMS system (Fig. 16g) accompanied by 63% TOC removal efficiency within 60 min. The reason for efficient SMX removal can be attributed to the regeneration of Co^{2+} by surficial sulfur species like S^{2-}/S_2^{2-}. In addition, the quantitative determination of the $SO_4^{\bullet-}$ and residual PMS were conducted. The quantification generation tests of $SO_4^{\bullet-}$ which attained to 26 μM indicated that it was the main ROS that involved in the degradation reactions. In all, as shown in Fig. 16h, the catalysis mechanisms could be attributed to the synergistic contribution of non-radical ($^1O_2$) and radical ($SO_4^{\bullet-}$) processes verified by ESR measurements and ROS quench tests. This work manifested that the cobalt sulfide with different morphologies can be rationally modified through the morphologies of the ZIF-67 precursors, which could possess improved catalytic organic pollutants degradation performance.

3. Conclusions and outlooks

In summary, we provided a review of the advancement of research in PS-AOPs for the application of wastewater treatment over ZIF-67-based catalysts. Besides the pristine ZIF-67, ZIF-67-based materials for PS-AOPs can be classified into three types. (i) ZIF-67 can be immobilized on some substrates like microscale resin, nickel foam, knitted fabrics and electrospinning fabrics to overcome the difficult separation of the powder ZIF-67-based catalysts and achieve the satisfied reusability. (ii) The binary or multiple ZIF-67 composite systems were constructed to boost the catalytic performance, in which the construction of magnetic ZIF-67 complexes can greatly improve recyclability. (iii) ZIF-67 was adopted as precursors or sacrificial templates to prepare powerful derivatives with high porosity, flexible structure as well as abundant catalytic active sites.

Although the remarkable progresses have been accomplished in the investigations of ZIF-67-based materials as efficient PS-AOPs catalysts, there are several key issues, challenges as well as opportunities to be considered in the future.

(i) As the most popular method for ZIF-67 synthesis, the solvothermal synthesis and room temperature incubation method displayed some weaknesses like long preparation time (hours or even days), low production, huge input of organic solvents and high cost. Hence, the novel high throughput and low-cost synthesis techniques of ZIF-67 free of the expensive or toxic solvents, were urgently needed.

(ii) It is of great importance to consider the stability (such as chemical, thermal, watery and mechanical stability) of ZIF-67-based materials when operating in PS-AOPs or under harsh conditions like pharmaceutical wastewater, aquaculture wastewater and industrial wastewater. To this end, the methods including post-synthetic modification, hydrophobic surface treatment, and composite fabrication could be used to enhance the stability of ZIF-67.

(iii) The issues of difficulty to reuse can be solved by shaping the ZIF-67-based material into a monolithic state. However, the catalytic performance would be sacrificed inevitably to some extent. Therefore, it is critical to establish a balance between post-recycling availability and the degradation properties of the ZIF-67-based catalyst. For this purpose, the development of immobilized ZIF-67 composites and immobilized ZIF-67 derivatives with excellent properties are promising candidates for practical applications.

(iv) The leakage of toxic cobalt ions has been a major challenge limiting the further application of ZIF-67-based materials in PS-AOPs. New catalysts and operation techniques, for example, core-shell structure catalysts, heterogeneous catalysts associated with membrane reactors or fixed-bed reactors and catalyst pretreatment technologies can effectively inhibit the dissolution of cobalt ions.
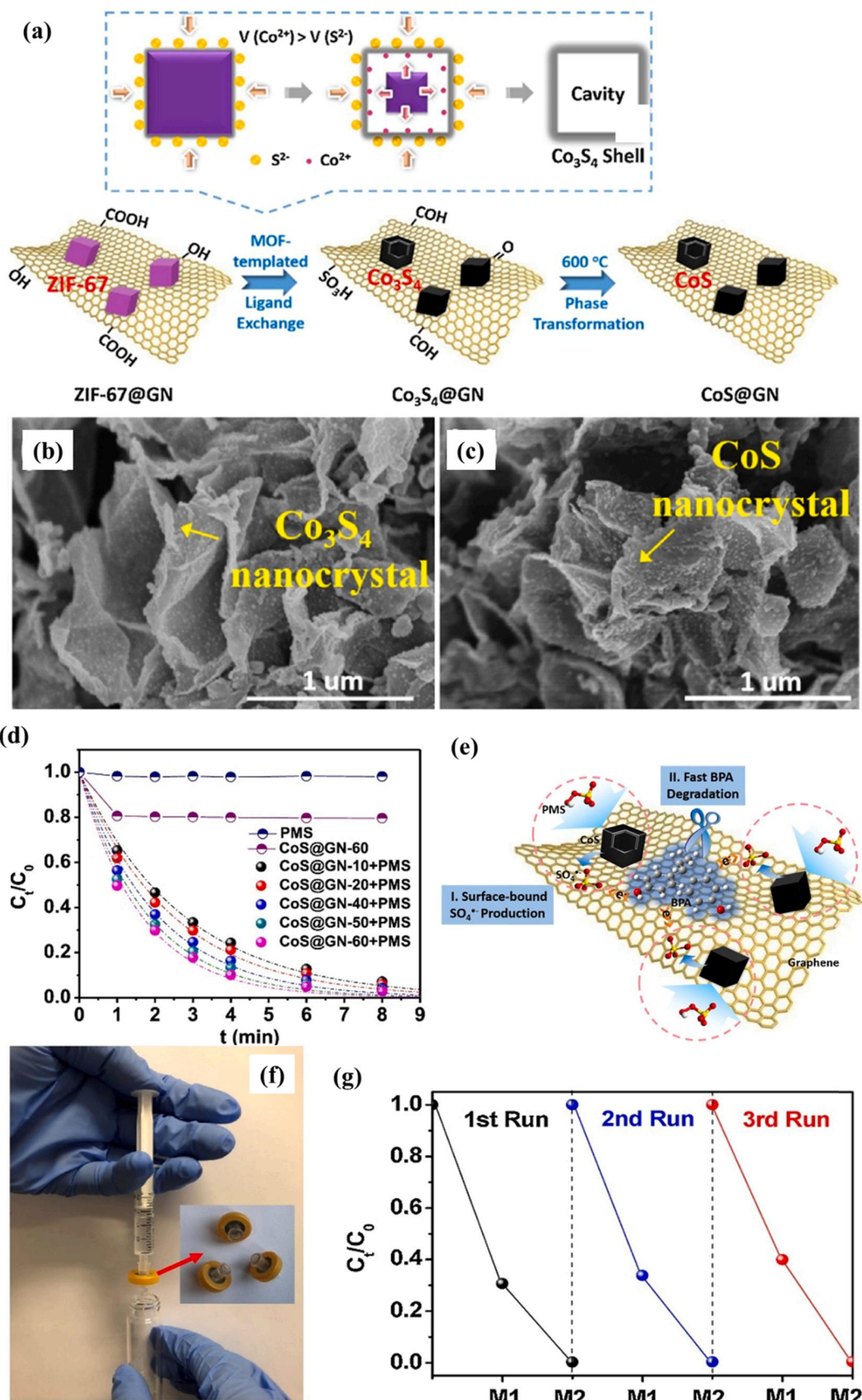
Fig. 15. (a) Schematic diagram for the preparation procedures of CoS@GN nanocrystals; SEM images of (b) Co_3S_4@GN-60, (c) CoS@GN-60; (d) Removal efficiency of BPA in different reaction systems. (e) The proposed mechanisms for surface-bound $SO_4^{\bullet-}$ production and BPA degradation. (f) Photograph of the CoS@GN-60-coated membrane reactor. (g) BPA removal efficiency over a two-grade CoS@GN-60-coated membrane reactor system in successive 3 cycles. Reproduced with permission from Ref. [211]. Copyright 2019 Elsevier.
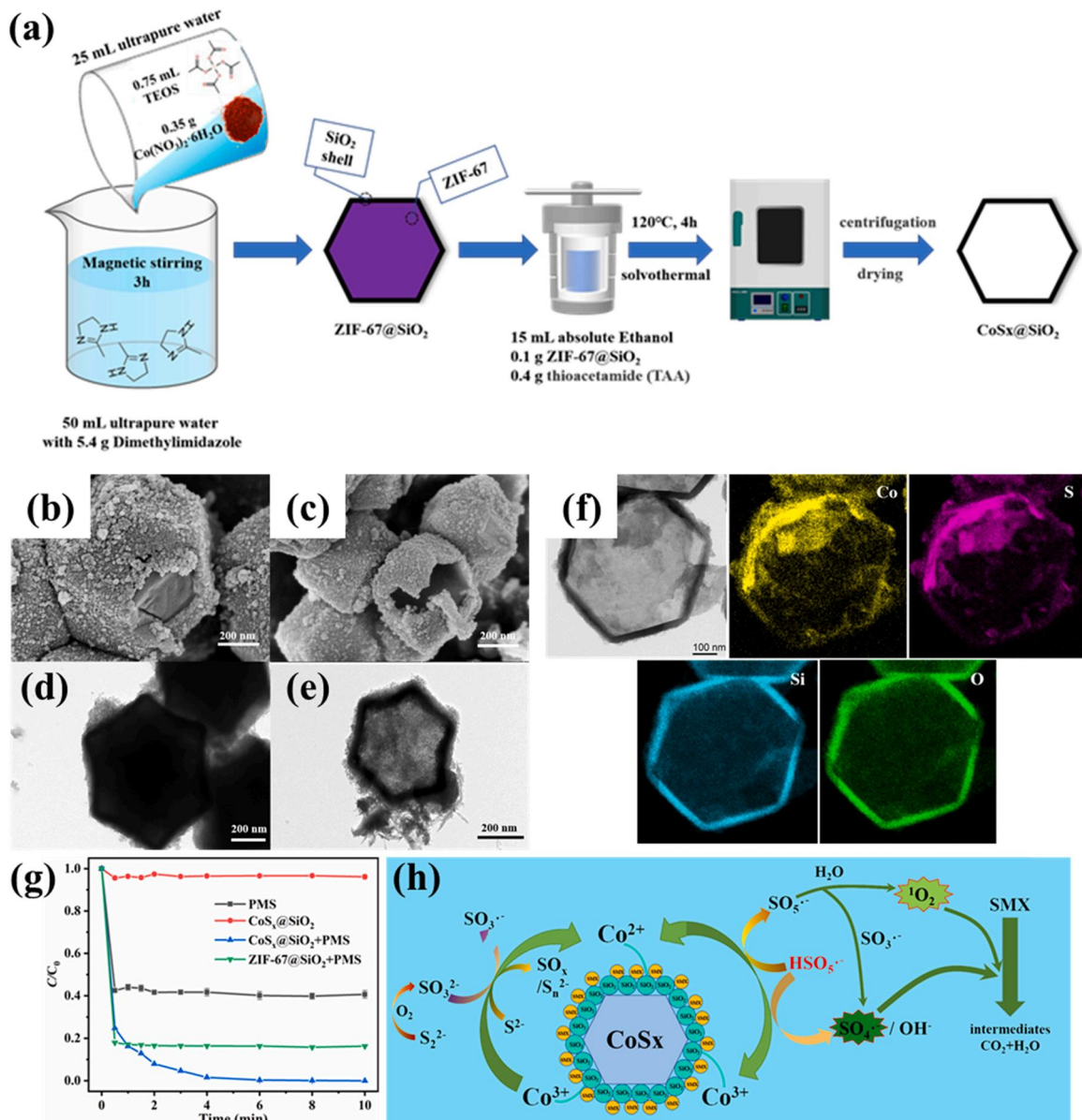
Fig. 16. (a) Synthetic preparation routes illustration of CoS$_x$ @SiO$_2$; The SEM images and TEM images of (b, d) ZIF-67 @SiO$_2$ and (c, e) CoS$_x$ @SiO$_2$. (f) The HRTEM image of CoS$_x$ @SiO$_2$ and corresponding EDS elemental mapping images of CoS$_x$ @SiO$_2$. (g) SMX degradation efficiency over different catalysts. (h) Proposed catalyst mechanism for SMX degradation over CoSx@SiO$_2$/PMS system. Reproduced with permission from Ref. [48]. Copyright 2022 Elsevier.

(v) The poor penetration of reactive oxygen species in PS-AOPs leads to poor mineralization toward organic pollutants, which might produce a large number of intermediate products even with higher toxicity. Hence, PS-AOPs can be used as a pretreatment process for oxidation of refractory macromolecules organic pollutants for detoxification, which can promote the improvement of biodegradability (BOD/COD ratio) and enhance the efficiency of subsequent biological treatment.

(vi) It is supposed to recognize that ZIF-67 with excellent adsorption properties can selectively enrich trace amounts of organic pollutants before coupling PS-AOPs to oxidatively degrade organic contaminations, which can achieve selective removal and deep degradation of trace pollutants in wastewater.

(vii) The introduction of light can not only activate PS directly, but also promote the electron transfer reactions through photo-assisted catalyst activation, which can significantly improve the catalytic degradation efficiency and the mineralization of pollutants. However, there are relatively few photo-PS systems based

on ZIF-67. As an excellent photocatalytic material, ZIF-67 can be attempted to combine with other organic/inorganic photocatalysts (perylenetetracarboxylic dianhydride, TiO$_2$, WO$_3$, etc.) to boost the development of ZIF-67 composites in PS-AOPs.

In conclusion, the reported preparation strategies, organic pollutants degradation performances and proposed mechanisms of PS-AOPs, as well as the current challenges for ZIF-67-based catalysts have been emphasized in this paper, which can deliver intensive insight in further investigation and exploitation of ZIF-67-based materials for contaminants elimination in water remediation for the sake of environmental sustainability and friendliness.

CRediT authorship contribution statement

Xiu-Wu Zhang: Conceptualization, Methodology, Formal analysis, Writing – original draft, Visualization. **Ming-Yan Lan:** Methodology, Software, Drawing. **Fei Wang:** Methodology, Software. **Xiao-Hong Yi:**

Conceptualization, Analyzing. **Chong-Chen Wang:** Conceptualization, Funding acquisition, Supervision, Project administration, Writing – review & editing.

Declaration of Competing Interest

The authors declare that they have no known competing financial interests or personal relationships that could have appeared to influence the work reported in this paper.

Acknowledgements

References

[1] A. Dominguez-Chicas, M.D. Scrimshaw, Hazard and risk assessment for indirect potable reuse schemes: an approach for use in developing water safety plans, Water Res. 44 (2010) 6115–6123.

[2] M.K. Yadav, D. Saidulu, A.K. Gupta, P.S. Ghosal, A. Mukherjee, Status and management of arsenic pollution in groundwater: a comprehensive appraisal of recent global scenario, human health impacts, sustainable field-scale treatment technologies, J. Environ. Chem. Eng. 9 (2021), 105203.

[3] K.C. Jones, P. De Voogt, Persistent organic pollutants (POPs): state of the science, Environ. Pollut. 100 (1999) 209–221.

[4] R. Kishor, D. Purchase, G.D. Saratale, R.G. Saratale, L.F.R. Ferreira, M. Bilal, R. Chandra, R.N. Bharagava, Ecotoxicological and health concerns of persistent coloring pollutants of textile industry wastewater and treatment approaches for environmental safety, J. Environ. Chem. Eng. 9 (2021) 105012.

[5] J. Ma, C.-C. Wang, Z.-X. Zhao, P. Wang, J.-J. Li, F.-X. Wang, Adsorptive capture of perrhenate (ReO$_4^-$) from simulated wastewater by cationic 2D-MOF BUC-17, Polyhedron 202 (2021) 115218.

[6] D. Pang, C.-C. Wang, P. Wang, W. Liu, H. Fu, C. Zhao, Superior removal of inorganic and organic arsenic pollutants from water with MIL-88A (Fe) decorated on cotton fibers, Chemosphere 254 (2020) 126829.

[7] F. Xiao, M.F. Simcik, J.S. Gulliver, Mechanisms for removal of perfluorooctane sulfonate (PFOS) and perfluorooctanoate (PFOA) from drinking water by conventional and enhanced coagulation, Water Res. 47 (2013) 49–56.

[8] Y. Zhang, G. Zhou, J. Yue, X. Xing, Z. Yang, X. Wang, Q. Wang, J. Zhang, Enhanced removal of polyethylene terephthalate microplastics through polyaluminum chloride coagulation with three typical coagulant aids, Sci. Total Environ. 800 (2021) 149589.

[9] X.-H. Yi, H. Ji, C.-C. Wang, Y. Li, Y.-H. Li, C. Zhao, A. Wang, H. Fu, P. Wang, X. Zhao, Photocatalysis-activated SR-AOP over PDINH/MIL-88A(Fe) composites for boosted chloroquine phosphate degradation: performance, mechanism, pathway and DFT calculations, Appl. Catal. B Environ. 293 (2021) 120229.

[10] C.-C. Wang, X.-H. Yi, P. Wang, Powerful combination of MOFs and C$_3$N$_4$ for enhanced photocatalytic performance, Appl. Catal. B Environ. 247 (2019) 24–48.

[11] X. Du, S. Wang, F. Ye, Q. Zhang, Derivatives of metal-organic frameworks for heterogeneous Fenton-like processes: from preparation to performance and mechanisms in wastewater purification—a mini review, Environ. Res. 206 (2021), 112414.

[12] F.-X. Wang, C.-C. Wang, X. Du, Y. Li, F. Wang, P. Wang, Efficient removal of emerging organic contaminants via photo-Fenton process over micron-sized Fe-MOF sheet, Chem. Eng. J. 429 (2021), 132495.

[13] Y. Song, C. Zhao, T. Wang, Z. Kong, L. Zheng, H. Ding, Y. Liu, H. Zheng, Simultaneously promoted reactive manganese species and hydroxyl radical generation by electro-permanganate with low additive ozone, Water Res. 189 (2021), 116623.

[14] W. Yang, M. Bunian, X. Chen, S. Heald, L. Yu, J. Wen, Y. Lei, T. Wu, Plasmon-enhanced catalytic ozonation for efficient removal of recalcitrant water pollutants, ACS EST Eng. 1 (5) (2021) 874–883.

[15] X. Du, W. Fu, P. Su, Q. Zhang, M. Zhou, S-doped MIL-53 as efficient heterogeneous electro-Fenton catalyst for degradation of sulfamethazine at circumneutral pH, J. Hazard. Mater. 424 (2022) 127674.

[16] X. Du, M.A. Oturan, M. Zhou, N. Belkessa, P. Su, J. Cai, C. Trellu, E. Mousset, Nanostructured electrodes for electrocatalytic advanced oxidation processes: from materials preparation to mechanisms understanding and wastewater treatment applications, Appl. Catal. B Environ. 296 (2021) 120332.

[17] X. Du, M. Zhou, Strategies to enhance catalytic performance of metal–organic frameworks in sulfate radical-based advanced oxidation processes for organic pollutants removal, Chem. Eng. J. 403 (2021) 126346.

[18] S. Giannakis, K.-Y.A. Lin, F. Ghanbari, A review of the recent advances on the treatment of industrial wastewaters by sulfate radical-based advanced oxidation processes (SR-AOPs), Chem. Eng. J. 406 (2021), 127083.

[19] J. Qi, J. Liu, F. Sun, T. Huang, J. Duan, W. Liu, High active amorphous Co(OH)$_2$ nanocages as peroxymonosulfate activator for boosting acetaminophen degradation and DFT calculation, Chin. Chem. Lett. 32 (5) (2021) 1814–1818.

[20] H. Wu, X. Xu, L. Shi, Y. Yin, L.-C. Zhang, Z. Wu, X. Duan, S. Wang, H. Sun, Manganese oxide integrated catalytic ceramic membrane for degradation of organic pollutants using sulfate radicals, Water Res. 167 (2019), 115110.

[21] H. Zhou, J. Peng, J. Li, J. You, L. Lai, R. Liu, Z. Ao, G. Yao, B. Lai, Metal-free black-red phosphorus as an efficient heterogeneous reductant to boost Fe^{3+}/Fe^{2+} cycle for peroxymonosulfate activation, Water Res. 188 (2021), 116529.

[22] W. Zheng, Y. Liu, W. Liu, H. Ji, F. Li, C. Shen, X. Fang, X. Li, X. Duan, A novel electrocatalytic filtration system with carbon nanotube supported nanoscale zerovalent copper toward ultrafast oxidation of organic pollutants, Water Res. 194 (2021), 116961.

[23] R. Yin, Y. Chen, J. Hu, S. Jin, W. Guo, M. Zhu, Peroxydisulfate bridged photocatalysis of covalent triazine framework for carbamazepine degradation, Chem. Eng. J. 427 (2022), 131613.

[24] Z. Li, S. Luo, Y. Yang, J. Chen, Highly efficient degradation of trichloroethylene in groundwater based on peroxymonosulfate activation by bentonite supported Fe/Ni bimetallic nanoparticle, Chemosphere 216 (2019) 499–506.

[25] E. Saputra, S. Muhammad, H. Sun, H.-M. Ang, M.O. Tadé, S. Wang, Manganese oxides at different oxidation states for heterogeneous activation of peroxymonosulfate for phenol degradation in aqueous solutions, Appl. Catal. B Environ. 142 (2013) 729–735.

[26] L. Chen, H. Ji, J. Qi, T. Huang, C.-C. Wang, W. Liu, Degradation of acetaminophen by activated peroxymonosulfate using Co(OH)$_2$ hollow microsphere supported titanate nanotubes: insights into sulfate radical production pathway through CoOH$^+$ activation, Chem. Eng. J. 406 (2021), 126877.

[27] J. Hou, X. He, S. Zhang, J. Yu, M. Feng, X. Li, Recent advances in cobalt-activated sulfate radical-based advanced oxidation processes for water remediation: a review, Sci. Total Environ. (2021), 145311.

[28] P. Hu, M. Long, Cobalt-catalyzed sulfate radical-based advanced oxidation: a review on heterogeneous catalysts and applications, Appl. Catal. B Environ. 181 (2016) 103–117.

[29] E. Jin, S. Lee, E. Kang, Y. Kim, W. Choe, Metal-organic frameworks as advanced adsorbents for pharmaceutical and personal care products, Coord. Chem. Rev. 425 (2020), 213526.

[30] N. Kundu, S. Sarkar, Porous organic frameworks for carbon dioxide capture and storage, J. Environ. Chem. Eng. 9 (2021), 105090.

[31] C.-C. Wang, J.-R. Li, X.-L. Lv, Y.-Q. Zhang, G. Guo, Photocatalytic organic pollutants degradation in metal–organic frameworks, Energy Environ. Sci. 7 (2014) 2831–2867.

[32] J. Cao, X. Li, H. Tian, Metal-organic framework (MOF)-based drug delivery, Curr. Med. Chem. 27 (2020) 5949–5969.

[33] K. Suresh, A.J. Matzger, Enhanced drug delivery by dissolution of amorphous drug encapsulated in a water unstable metal–organic framework(MOF), Angew. Chem. Int. Ed. 58 (2019) 16790–16794.

[34] S.A. Hira, D. Annas, S. Nagappan, Y.A. Kumar, S. Song, H.-J. Kim, S. Park, K. H. Park, Electrochemical sensor based on nitrogen-enriched metal–organic framework for selective and sensitive detection of hydrazine and hydrogen peroxide, J. Environ. Chem. Eng. 9 (2021) 105182.

[35] C.-Y. Wang, C.-C. Wang, X.-W. Zhang, X.-Y. Ren, B. Yu, P. Wang, Z.-X. Zhao, H. Fu, A new Eu-MOF for ratiometrically fluorescent detection toward quinolone antibiotics and selective detection toward tetracycline antibiotics, Chin. Chem. Lett. 33 (2022) 1353–1357.

[36] Y. Zhang, S. Yuan, G. Day, X. Wang, X. Yang, H.-C. Zhou, Luminescent sensors based on metal-organic frameworks, Coord. Chem. Rev. 354 (2018) 28–45.

[37] G. Zhong, D. Liu, J. Zhang, The application of ZIF-67 and its derivatives: adsorption, separation, electrochemistry and catalysts, J. Mater. Chem. A 6 (2018) 1887–1899.

[38] R. Banerjee, A. Phan, B. Wang, C. Knobler, H. Furukawa, M. O'Keeffe, O. M. Yaghi, High-throughput synthesis of zeolitic imidazolate frameworks and application to CO$_2$ capture, Science 319 (2008) 939–943.

[39] K.-Y.A. Lin, B.-C. Chen, Efficient elimination of caffeine from water using Oxone activated by a magnetic and recyclable cobalt/carbon nanocomposite derived from ZIF-67, Dalton Trans. 45 (2016) 3541–3551.

[40] R.M. Abdelhameed, M. Abu-Elghait, M. El-Shahat, Hybrid three MOFs composites (ZIF-67@ZIF-8@MIL-125-NH$_2$): enhancement the biological and visible-light photocatalytic activity, J. Environ. Chem. Eng. 8 (2020), 104107.

[41] X. Wu, W. Liu, H. Wu, X. Zong, L. Yang, Y. Wu, Y. Ren, C. Shi, S. Wang, Z. Jiang, Nanoporous ZIF-67 embedded polymers of intrinsic microporosity membranes with enhanced gas separation performance, J. Membr. Sci. 548 (2018) 309–318.

[42] Q. Yang, S. Ren, Q. Zhao, R. Lu, C. Hang, Z. Chen, H. Zheng, Selective separation of methyl orange from water using magnetic ZIF-67 composites, Chem. Eng. J. 333 (2018) 49–57.

[43] C. Duan, Y. Yu, H. Hu, Recent progress on synthesis of ZIF-67-based materials and their application to heterogeneous catalysis, Green Energy Environ. 7 (2022) 3–15.

[44] Y. Li, Z. Jin, T. Zhao, Performance of ZIF-67–Derived fold polyhedrons for enhanced photocatalytic hydrogen evolution, Chem. Eng. J. 382 (2020) 123051.

[45] M. Kohantorabi, S. Giannakis, G. Moussavi, M. Bensimon, M.R. Gholami, C. Pulgarin, An innovative, highly stable Ag/ZIF-67@GO nanocomposite with exceptional peroxymonosulfate (PMS) activation efficacy, for the destruction of chemical and microbiological contaminants under visible light, J. Hazard. Mater. 413 (2021), 125308.

[46] J.-y Pu, J.-q Wan, Y. Wang, Y.-w Ma, Different Co-based MOFs templated synthesis of Co₃O₄ nanoparticles to degrade RhB by activation of oxone, RSC Adv. 6 (94) (2016) 91791–91797.

[47] C. Wang, P. Cheng, Y. Yao, Y. Yamauchi, X. Yan, J. Li, J. Na, In-situ fabrication of nanoarchitectured MOF filter for water purification, J. Hazard. Mater. 392 (2020), 122164.

[48] F. Wang, H. Fu, F.-X. Wang, X.-W. Zhang, P. Wang, C. Zhao, C.-C. Wang, Enhanced catalytic sulfamethoxazole degradation via peroxymonosulfate activation over amorphous CoSₓ@SiO₂ nanocages derived from ZIF-67, J. Hazard. Mater. 423 (2022), 126998.

[49] J. Qin, S. Wang, X. Wang, Visible-light reduction CO₂ with dodecahedral zeolitic imidazolate framework ZIF-67 as an efficient co-catalyst, Appl. Catal. B Environ. 209 (2017) 476–482.

[50] K.-Y.A. Lin, F.-K. Hsu, W.-D. Lee, Magnetic cobalt–graphene nanocomposite derived from self-assembly of MOFs with graphene oxide as an activator for peroxymonosulfate, J. Mater. Chem. A 3 (18) (2015) 9480–9490.

[51] J. Qian, F. Sun, L. Qin, Hydrothermal synthesis of zeolitic imidazolate framework-67(ZIF-67) nanocrystals, Mater. Lett. 82 (2012) 220–223.

[52] S. Rojas, P. Horcajada, Metal–organic frameworks for the removal of emerging organic contaminants in water, Chem. Rev. 120 (16) (2020) 8378–8415.

[53] C.-H. Wu, W.-C. Yun, T. Wi-Afedzi, K.-Y.A. Lin, ZIF-67 supported on marcoscale resin as an efficient and convenient heterogeneous catalyst for Oxone activation, J. Colloid Interface Sci. 514 (2018) 262–271.

[54] C. Wang, H. Wang, R. Luo, C. Liu, J. Li, X. Sun, J. Shen, W. Han, L. Wang, Metal-organic framework one-dimensional fibers as efficient catalysts for activating peroxymonosulfate, Chem. Eng. J. 330 (2017) 262–271.

[55] M. Chen, N. Wang, X. Wang, Y. Zhou, L. Zhu, Enhanced degradation of tetrabromobisphenol A by magnetic Fe₃O₄@ZIF-67 composites as a heterogeneous Fenton-like catalyst, Chem. Eng. J. 413 (2021), 127539.

[56] B. Hashemzadeh, H. Alamgholiloo, N.N. Pesyan, E. Asgari, A. Sheikhmohammadi, J. Yeganeh, H. Hashemzadeh, Degradation of ciprofloxacin using hematite/MOF nanocomposite as a heterogeneous Fenton-like Catalyst: a comparison of composite and core−shell structures, Chemosphere 281 (2021), 130970.

[57] M. Wang, Y. Cui, H. Cao, P. Wei, C. Chen, X. Li, J. Xu, G. Sheng, Activating peroxydisulfate with Co₃O₄/NiCo₂O₄ double-shelled nanocages to selectively degrade bisphenol A–A nonradical oxidation process, Appl. Catal. B Environ. 282 (2021), 119585.

[58] M. Zhang, C. Xiao, X. Yan, S. Chen, C. Wang, R. Luo, J. Qi, X. Sun, L. Wang, J. Li, Efficient removal of organic pollutants by metal–organic framework derived Co/C yolk–shell nanoreactors: size-exclusion and confinement effect, Environ. Sci. Technol. 54 (16) (2020) 10289–10300.

[59] X. Wu, W. Zhao, Y. Huang, G. Zhang, A mechanistic study of amorphous CoSx cages as advanced oxidation catalysts for excellent peroxymonosulfate activation towards antibiotics degradation, Chem. Eng. J. 381 (2020), 122768.

[60] X. Ma, Y.-X. Zhou, H. Liu, Y. Li, H.-L. Jiang, A MOF-derived, Co–CoO@N-doped porous carbon for efficient tandem catalysis: dehydrogenation of ammonia borane and hydrogenation of nitro compounds, Chem. Commun. 52 (49) (2016) 7719–7722.

[61] L. Zhang, A. Wu, M. Tian, Y. Xiao, X. Shi, H. Yan, C. Tian, H. Fu, 2-D porous Ni₃N–Co₃N hybrids derived from ZIF-67/Ni (OH)₂ sheets as a magnetically separable catalyst for hydrogenation reactions, Chem. Commun. 54 (79) (2018) 11088–11091.

[62] Z. Jiang, Z. Li, Z. Qin, H. Sun, X. Jiao, D. Chen, LDH nanocages synthesized with MOF templates and their high performance as supercapacitors, Nanoscale 5 (23) (2013) 11770–11775.

[63] C. Duan, F. Li, M. Yang, H. Zhang, Y. Wu, H. Xi, Rapid synthesis of hierarchically structured multifunctional metal–organic zeolites with enhanced volatile organic compounds adsorption capacity, Ind. Eng. Chem. Res. 57 (45) (2018) 15385–15394.

[64] Q. Yang, R. Lu, S. Ren, C. Chen, Z. Chen, X. Yang, Three dimensional reduced graphene oxide/ZIF-67 aerogel: effective removal cationic and anionic dyes from water, Chem. Eng. J. 348 (2018) 202–211.

[65] X.-D. Du, C.-C. Wang, J.-G. Liu, X.-D. Zhao, J. Zhong, Y.-X. Li, J. Li, P. Wang, Extensive and selective adsorption of ZIF-67 towards organic dyes: performance and mechanism, J. Colloid Interface Sci. 506 (2017) 437–441.

[66] Q. Shi, Z. Chen, Z. Song, J. Li, J. Dong, Synthesis of ZIF-8 and ZIF-67 by steam-assisted conversion and an investigation of their tribological behaviors, Angew. Chem. 123 (2011) 698–701.

[67] F. Hillman, J.M. Zimmerman, S.-M. Paek, M.R. Hamid, W.T. Lim, H.-K. Jeong, Rapid microwave-assisted synthesis of hybrid zeolitic-imidazolate frameworks with mixed metals and mixed linkers, J. Mater. Chem. A 5 (13) (2017) 6090–6099.

[68] N.T.T. Tu, P.C. Sy, T.V. Thien, T.T.T. Toan, N.H. Phong, H.T. Long, D.Q. Khieu, Microwave-assisted synthesis and simultaneous electrochemical determination of dopamine and paracetamol using ZIF-67-modified electrode, J. Mater. Sci. 54 (17) (2019) 11654–11670.

[69] J. Ethiraj, S. Palla, H. Reinsch, Insights into high pressure gas adsorption properties of ZIF-67: experimental and theoretical studies, Microporous Mesoporous Mater. 294 (2020), 109867.

[70] N.M. Mahmoodi, M. Taghizadeh, A. Taghizadeh, J. Abdi, B. Hayati, A. A. Shekarchi, Bio-based magnetic metal-organic framework nanocomposite: Ultrasound-assisted synthesis and pollutant (heavy metal and dye) removal from aqueous media, Appl. Surf. Sci. 480 (2019) 288–299.

[71] H. Wang, D. Wu, C. Yang, H. Lu, Z. Gao, F. Xu, K. Jiang, Multi-functional amorphous TiO₂ layer on ZIF-67 for enhanced CO₂ photoreduction performances under visible light, J. CO2 Util. 34 (2019) 411–421.

[72] H. Zhou, M. Zheng, H. Tang, B. Xu, Y. Tang, H. Pang, Amorphous intermediate derivative from ZIF-67 and its outstanding electrocatalytic activity, Small 16 (2) (2020) 1904252.

[73] K.-Y.A. Lin, H.-A. Chang, Zeolitic Imidazole Framework-67 (ZIF-67) as a heterogeneous catalyst to activate peroxymonosulfate for degradation of Rhodamine B in water, J. Taiwan Inst. Chem. Eng. 53 (2015) 40–45.

[74] X. Hu, Y. Ye, Y. Chen, M. Liu, W. Zhang, M. Zhu, The synergistic interactions of reaction parameters in heterogeneous peroxymonosulfate oxidation: reaction kinetic and catalytic mechanism, J. Hazard. Mater. 421 (2022), 126841.

[75] S. Guo, H. Tang, L. You, H. Zhang, J. Li, K. Zhou, Combustion synthesis of mesoporous CoAl₂O₄ for peroxymonosulfate activation to degrade organic pollutants, Chin. Chem. Lett. 32 (2021) 2828–2832.

[76] X.-W. Zhang, F. Wang, C.-C. Wang, P. Wang, H. Fu, C. Zhao, Photocatalysis activation of peroxodisulfate over the supported Fe₃O₄ catalyst derived from MIL-88A(Fe) for efficient tetracycline hydrochloride degradation, Chem. Eng. J. 426 (2021), 131927.

[77] J.L. Gurav, I.-K. Jung, H.-H. Park, E.S. Kang, D.Y. Nadargi, Silica aerogel: synthesis and applications, J. Nanomater 2010 (2010), 409310.

[78] Z.-J. Jiang, C.-Y. Liu, L.-W. Sun, Catalytic properties of silver nanoparticles supported on silica spheres, J. Phys. Chem. B 109 (5) (2005) 1730–1735.

[79] C. Ge, X. Sang, W. Yao, L. Zhang, D. Wang, Unsymmetrical indazolyl-pyridinyl-triazole ligand-promoted highly active iridium complexes supported on hydrotalcite and its catalytic application in water, Green Chem. 20 (8) (2018) 1805–1812.

[80] Q. Shao, H. Dong, J. Zhang, B. Xu, Y. Wu, C. Long, Manganese supported on controlled dealumination Y-zeolite for ozone catalytic oxidation of low concentration toluene at low temperature, Chemosphere 271 (2021), 129604.

[81] X. Du, X. Yi, P. Wang, J. Deng, C.-C. Wang, Enhanced photocatalytic Cr (VI) reduction and diclofenac sodium degradation under simulated sunlight irradiation over MIL-100(Fe)/g-C₃N₄ heterojunctions, Chin. J. Catal. 40 (1) (2019) 70–79.

[82] Q. Zhao, X.-H. Yi, C.-C. Wang, P. Wang, W. Zheng, Photocatalytic Cr (VI) reduction over MIL-101(Fe)–NH₂ immobilized on alumina substrate: from batch test to continuous operation, Chem. Eng. J. 429 (2022), 132497.

[83] X.-D. Du, X.-H. Yi, P. Wang, W. Zheng, J. Deng, C.-C. Wang, Robust photocatalytic reduction of Cr(VI) on UiO-66-NH₂(Zr/Hf) metal-organic framework membrane under sunlight irradiation, Chem. Eng. J. 356 (2019) 393–399.

[84] Q. Zhao, C.-C. Wang, P. Wang, Effective norfloxacin elimination via photo-Fenton process over the MIL-101(Fe)-NH₂ immobilized on α-Al₂O₃ sheet, Chin. Chem. Lett. (2022), https://doi.org/10.1016/j.cclet.2022.01.033.

[85] J.-S. Wang, X.-H. Yi, X. Xu, H. Ji, A.M. Alanazi, C.-C. Wang, C. Zhao, Y.V. Kaneti, P. Wang, W. Liu, Eliminating tetracycline antibiotics matrix via photoactivated sulfate radical-based advanced oxidation process over the immobilized MIL-88A: Batch and continuous experiments, Chem. Eng. J. (2022), 133213.

[86] A. Du, H. Fu, P. Wang, C. Zhao, C.-C. Wang, Enhanced catalytic peroxymonosulfate activation for sulfonamide antibiotics degradation over the supported CoSₓ-CuSₓ derived from ZIF-L(Co) immobilized on copper foam, J. Hazard. Mater. 426 (2022), 128134.

[87] L. Peng, X. Gong, X. Wang, Z. Yang, Y. Liu, In situ growth of ZIF-67 on a nickel foam as a three-dimensional heterogeneous catalyst for peroxymonosulfate activation, RSC Adv. 8 (2018) 26377–26382.

[88] N. Li, G. Chen, J. Zhao, B. Yan, Z. Cheng, L. Meng, V. Chen, Self-cleaning PDA/ZIF-6@PP membrane for dye wastewater remediation with peroxymonosulfate and visible light activation, J. Membr. Sci. 591 (2019), 117341.

[89] Y. Wu, W. Ren, Y. Li, J. Gao, X. Yang, J. Yao, Zeolitic Imidazolate Framework-67/Cellulose aerogel for rapid and efficient degradation of organic pollutants, J. Solid State Chem. 291 (2020), 121621.

[90] S. Zhang, M. Zhao, H. Li, C. Hou, M. Du, Facile in situ synthesis of ZIF-67/cellulose hybrid membrane for activating peroxymonosulfate to degrade organic contaminants, Cellulose 28 (6) (2021) 3585–3598.

[91] W. Sun, K. Thummavichai, D. Chen, Y. Lei, H. Pan, T. Song, N. Wang, Y. Zhu, Co-zeolitic imidazolate framework@ cellulose aerogels from sugarcane bagasse for activating peroxymonosulfate to degrade P-nitrophenol, Polymers 13 (5) (2021) 739.

[92] A. Figuerola, D.A. Medina, A.J. Santos-Neto, C.P. Cabello, V. Cerdà, G. T. Palomino, F. Maya, Metal–organic framework mixed-matrix coatings on 3D printed devices, Appl. Mater. Today 16 (2019) 21–27.

[93] D. Liu, P. Jiang, X. Xu, J. Wu, Y. Lu, X. Wang, X. Wang, W. Liu, MOFs decorated sugarcane catalytic filter for water purification, Chem. Eng. J. 431 (2022), 133992.

[94] Y. Lei, W. Sun, S.K. Tiwari, K. Thummavichai, O. Ola, X. Qin, Z. Ma, N. Wang, Y. Zhu, Zn/Co-ZIF reinforced sugarcane bagasse aerogel for highly efficient catalytic activation of peroxymonosulfate, J. Environ. Chem. Eng. 9 (2021), 106885.

[95] D. Liu, J. Yin, H. Tang, H. Wang, S. Liu, T. Huang, S. Fang, K. Zhu, Z. Xie, Fabrication of ZIF-67@PVDF ultrafiltration membrane with improved antifouling and separation performance for dye wastewater treatment via sulfate radical enhancement, Sep. Purif. Technol. 279 (2021), 119755.

[96] Y. Chou, C. Shao, X. Li, C. Su, H. Xu, M. Zhang, P. Zhang, X. Zhang, Y. Liu, BiOCl nanosheets immobilized on electrospun polyacrylonitrile nanofibers with high photocatalytic activity and reusable property, Appl. Surf. Sci. 285 (2013) 509–516.

[97] J. Ding, Y. Bu, Y. Ou, Y. Yu, Q. Zhong, M. Fan, Facile decoration of carbon fibers with Ag nanoparticles for adsorption and photocatalytic reduction of CO₂, Appl. Catal. B Environ. 202 (2017) 314–325.

[98] C.-L. Zhang, S.-H. Yu, Nanoparticles meet electrospinning: recent advances and future prospects, Chem. Soc. Rev. 43 (13) (2014) 4423–4448.

[99] T. Fu, J. Lv, Z. Li, Effect of carbon porosity and cobalt particle size on the catalytic performance of carbon supported cobalt Fischer–Tropsch catalysts, Ind. Eng. Chem. Res. 53 (4) (2014) 1342–1350.

[100] S. Sun, H. Li, Z.J. Xu, Impact of surface area in evaluation of catalyst activity, Joule 2 (6) (2018) 1024–1027.

[101] Z. Li, G. Zhou, H. Dai, M. Yang, Y. Fu, Y. Ying, Y. Li, Biomineralization-mimetic preparation of hybrid membranes with ultra-high loading of pristine metal–organic frameworks grown on silk nanofibers for hazard collection in water, J. Mater. Chem. A 6 (8) (2018) 3402–3413.

[102] P. Munnik, P.E. de Jongh, K.P. de Jong, Recent developments in the synthesis of supported catalysts, Chem. Rev. 115 (14) (2015) 6687–6718.

[103] A.F. Gross, E. Sherman, J.J. Vajo, Aqueous room temperature synthesis of cobalt and zinc sodalite zeolitic imidizolate frameworks, Dalton Trans. 41 (18) (2012) 5458–5460.

[104] J. Li, H. Wang, X. Yuan, J. Zhang, J.W. Chew, Metal-organic framework membranes for wastewater treatment and water regeneration, Coord. Chem. Rev. 404 (2020), 213116.

[105] C. Mack, J. Burgess, J. Duncan, Membrane bioreactors for metal recovery from wastewater: a review, Water SA 30 (4) (2004) 521–532.

[106] X. Zheng, Z.-P. Shen, L. Shi, R. Cheng, D.-H. Yuan, Photocatalytic membrane reactors (PMRs) in water treatment: configurations and influencing factors, Catalysts 7 (8) (2017) 224.

[107] X. Bao, Q. Wu, W. Shi, W. Wang, Z. Zhu, Z. Zhang, R. Zhang, X. Zhang, B. Zhang, Y. Guo, Insights into simultaneous ammonia-selective and anti-fouling mechanism over forward osmosis membrane for resource recovery from domestic wastewater, J. Membr. Sci. 573 (2019) 135–144.

[108] N. Li, Y. Tian, J. Zhao, J. Zhang, L. Kong, J. Zhang, W. Zuo, Static adsorption of protein-polysaccharide hybrids on hydrophilic modified membranes based on atomic layer deposition: anti-fouling performance and mechanism insight, J. Membr. Sci. 548 (2018) 470–480.

[109] S. Lotfikatouli, P. Hadi, M. Yang, H.W. Walker, B.S. Hsiao, C. Gobler, M. Reichel, X. Mao, Enhanced anti-fouling performance in membrane bioreactors using a novel cellulose nanofiber-coated membrane, Sep. Purif. Technol. 275 (2021), 119145.

[110] G. Wang, D. Wang, X. Dong, X. Zhang, H. Ma, Sodium persulfate based PVDF membrane for concurrent advanced oxidation and ultrafiltration of ofloxacin in water, Chem. Eng. J. 315 (2017) 509–515.

[111] Y. Yao, C. Lian, Y. Hu, J. Zhang, M. Gao, Y. Zhang, S. Wang, Heteroatoms doped metal iron–polyvinylidene fluoride (PVDF) membrane for enhancing oxidation of organic contaminants, J. Hazard. Mater. 338 (2017) 265–275.

[112] S. Hong, Y.S. Na, S. Choi, I.T. Song, W.Y. Kim, H. Lee, Non-covalent self-assembly and covalent polymerization co-contribute to polydopamine formation, Adv. Funct. Mater. 22 (22) (2012) 4711–4717.

[113] H. Lee, S.M. Dellatore, W.M. Miller, P.B. Messersmith, Mussel-inspired surface chemistry for multifunctional coatings, Science 318 (5849) (2007) 426–430.

[114] A. Postma, Y. Yan, Y. Wang, A.N. Zelikin, E. Tjipto, F. Caruso, Self-polymerization of dopamine as a versatile and robust technique to prepare polymer capsules, Chem. Mater. 21 (14) (2009) 3042–3044.

[115] K. Wei, A. Armutlulu, Y. Wang, G. Yao, R. Xie, B. Lai, Visible-light-driven removal of atrazine by durable hollow core-shell $TiO_2@LaFeO_3$ heterojunction coupling with peroxymonosulfate via enhanced electron-transfer, Appl. Catal. B Environ. 303 (2022), 120889.

[116] D.-D. Chen, X.-H. Yi, C. Zhao, H. Fu, P. Wang, C.-C. Wang, Polyaniline modified MIL-100(Fe) for enhanced photocatalytic Cr(VI) reduction and tetracycline degradation under white light, Chemosphere 245 (2020), 125659.

[117] Y.-C. Zhou, P. Wang, H. Fu, C. Zhao, C.-C. Wang, Ternary $Ag/Ag_3PO_4/MIL-125-NH_2$ Z-scheme heterojunction for boosted photocatalytic Cr(VI) cleanup under visible light, Chin. Chem. Lett. 31 (10) (2020) 2645–2650.

[118] J.-W. Wang, F.-G. Qiu, P. Wang, C. Ge, C.-C. Wang, Boosted bisphenol A and Cr (VI) cleanup over Z-scheme $WO_3/MIL-100(Fe)$ composites under visible light, J. Clean. Prod. 279 (2021), 123408.

[119] C. Zhao, J. Wang, X. Chen, Z. Wang, H. Ji, L. Chen, W. Liu, C.-C. Wang, Bifunctional $Bi_{12}O_{17}Cl_2/MIL-100(Fe)$ composites toward photocatalytic Cr (VI) sequestration and activation of persulfate for bisphenol A degradation, Sci. Total Environ. 752 (2021) 141901.

[120] D.D. Chen, X.H. Yi, L. Ling, C.C. Wang, P. Wang, Photocatalytic Cr(VI) sequestration and photo-Fenton bisphenol A decomposition over white light responsive PANI/MIL-88A(Fe), Appl. Organomet. Chem. 34 (9) (2020), e5795.

[121] H. Li, C. Zhao, X. Li, H. Fu, Z. Wang, C.-C. Wang, Boosted photocatalytic Cr(VI) reduction over Z-scheme $MIL-53(Fe)/Bi_{12}O_{17}Cl_2$ composites under white light, J. Alloy. Compd. 844 (2020), 156147.

[122] L. Wu, C.-C. Wang, H.-Y. Chu, X.-H. Yi, P. Wang, C. Zhao, H. Fu, Bisphenol A cleanup over MIL-100(Fe)/CoS composites: pivotal role of Fe-S bond in regenerating Fe^{2+} ions for boosted degradation performance, Chemosphere 280 (2021), 130659.

[123] X.-H. Yi, S.-Q. Ma, X.-D. Du, C. Zhao, H. Fu, P. Wang, C.-C. Wang, The facile fabrication of 2D/3D Z-scheme $g-C_3N_4/UiO-66$ heterojunction with enhanced photocatalytic Cr(VI) reduction performance under white light, Chem. Eng. J. 375 (2019), 121944.

[124] Y.-C. Zhou, X.-Y. Xu, P. Wang, H. Fu, C. Zhao, C.-C. Wang, Facile fabrication and enhanced photocatalytic performance of visible light responsive $UiO-66-NH_2/Ag_2CO_3$ composite, Chinese, J. Catal. 40 (12) (2019) 1912–1923.

[125] Y.-X. Li, X. Wang, C.-C. Wang, H. Fu, Y. Liu, P. Wang, C. Zhao, $S-TiO_2/UiO-66-NH_2$ composite for boosted photocatalytic Cr (VI) reduction and bisphenol A degradation under LED visible light, J. Hazard. Mater. 399 (2020), 123085.

[126] X. Wei, C.-C. Wang, Y. Li, P. Wang, Q. Wei, The Z-scheme $NH_2-UiO-66/PTCDA$ composite for enhanced photocatalytic Cr(VI) reduction under low-power LED visible light, Chemosphere 280 (2021), 130734.

[127] C. Zhao, Y. Li, H. Chu, X. Pan, L. Ling, P. Wang, H. Fu, C.-C. Wang, Z. Wang, Construction of direct Z-scheme $Bi_5O_7I/UiO-66-NH_2$ heterojunction photocatalysts for enhanced degradation of ciprofloxacin: mechanism insight, pathway analysis and toxicity evaluation, J. Hazard. Mater. 419 (2021), 126446.

[128] C. Zhao, Z. Wang, X. Li, X. Yi, H. Chu, X. Chen, C.-C. Wang, Facile fabrication of $BUC-21/Bi_{24}O_{31}Br_{10}$ composites for enhanced photocatalytic Cr (VI) reduction under white light, Chem. Eng. J. 389 (2020), 123431.

[129] X. Wang, Y.-X. Li, X.-H. Yi, C. Zhao, P. Wang, J. Deng, C.-C. Wang, Photocatalytic Cr(VI) elimination over $BUC-21/N-K_2Ti_4O_9$ composites: big differences in performance resulting from small differences in composition,, Chin. J. Catal. 42 (2) (2021) 259–270.

[130] X. Wei, P. Wang, H. Fu, C. Zhao, C.-C. Wang, Boosted photocatalytic elimination toward Cr(VI) and organic pollutants over $BUC-21/Cd_{0.5}Zn_{0.5}S$ under LED visible Light, Mater. Res. Bull. 129 (2020), 110903.

[131] X.H. Yi, F.X. Wang, X.D. Du, P. Wang, C.C. Wang, Facile fabrication of $BUC-21/g-C_3N_4$ composites and their enhanced photocatalytic Cr (VI) reduction performances under simulated sunlight, Appl. Organomet. Chem. 33 (1) (2019), e4621.

[132] X. Wang, W. Liu, H. Fu, X.-H. Yi, P. Wang, C. Zhao, C.-C. Wang, W. Zheng, Simultaneous Cr(VI) reduction and Cr(III) removal of bifunctional MOF/Titanate nanotube composites, Environ. Pollut. 249 (2019) 502–511.

[133] L. Dong, Y. Li, X. Chen, D. Zhang, Y. Guan, ZIF-67 loaded on $Fe_3O_4–MnO_2$ as efficient peroxymonosulfate activator for rapid degradation of carbamazepine, Adv. Mater. Interfaces (2021) 2100178.

[134] J. Cui, T. Liu, Q. Zhang, T. Wang, X. Hou, Rapid microwave synthesis of $Fe_3O_4-PVP@ZIF-67$ as highly effective peroxymonosulfate catalyst for degradation of bisphenol F and its mechanism analysis, Chem. Eng. J. 404 (2021), 126453.

[135] H. Alamgholiloo, B. Hashemzadeh, N.N. Pesyan, A. Sheikhmohammadi, E. Asgari, J. Yeganeh, H. Hashemzadeh, A facile strategy for designing core-shell nanocomposite of $ZIF-67/Fe_3O_4$: a novel insight into ciprofloxacin removal from wastewater, Process Saf. Environ. 147 (2021) 392–404.

[136] B. Li, Y. Li, J. Ren, F. Dai, Y. Zhang, Y. He, P. Song, R. Wang, Hydroxyapatite Coated with Co-Based Metal Organic Framework Nanoparticles as Heterojunctions for Catalytic Degradation of Organics, ACS Appl. Nano Mater. 4 (2021) 9370–9381.

[137] X. Wu, D. Sun, H. Ma, C. Ma, X. Zhang, J. Hao, Activation of peroxymonosulfate by magnetic $CuFe_2O_4@ZIF-67$ composite catalyst for the study on the degradation of methylene blue, Colloids Surf. A Physicochem. Eng. Asp. 637 (2022), 128278.

[138] H. Wan, Y. Yan, C. Guo, Q. Cui, W. Zhang, Synthesis of core-heteroshell structure for ZIF-67/VTM and its efficient activation of peroxymonosulfate in treatment of levofloxacin from an aqueous solution, Environ. Res. 204 (2022), 111986.

[139] Y. Wang, J. Cao, Z. Yang, W. Xiong, Z. Xu, P. Song, M. Jia, S. Sun, Y. Zhang, W. Li, Fabricating iron-cobalt layered double hydroxide derived from metal-organic framework for the activation of peroxymonosulfate towards tetracycline degradation, J. Solid State Chem. 294 (2021), 121857.

[140] J. Gómez-Pastora, S. Dominguez, E. Bringas, M.J. Rivero, I. Ortiz, D.D. Dionysiou, Review and perspectives on the use of magnetic nanophotocatalysts (MNPCs) in water treatment, Chem. Eng. J. 310 (2017) 407–427.

[141] L.P. Lingamdinne, S. Lee, J.-S. Choi, V.R. Lebaka, V.R.P. Durbaka, J.R. Koduru, Potential of the magnetic hollow sphere nanocomposite (graphene oxide-gadolinium oxide) for arsenic removal from real field water and antimicrobial applications, J. Hazard. Mater. 402 (2021), 123882.

[142] M.A. Maksoud, A.M. Elgarahy, C. Farrell, H. Ala'a, D.W. Rooney, A.I. Osman, Insight on water remediation application using magnetic nanomaterials and biosorbents, Coord. Chem. Rev. 403 (2020), 213096.

[143] W. Ma, N. Wang, T. Tong, L. Zhang, K.-Y.A. Lin, X. Han, Y. Du, Nitrogen, phosphorus, and sulfur tri-doped hollow carbon shells derived from ZIF-67@poly (cyclotriphosphazene-co-4, 4'-sulfonyldiphenol) as a robust catalyst of peroxymonosulfate activation for degradation of bisphenol A, Carbon 137 (2018) 291–303.

[144] Y. Sun, Y. Xia, Shape-controlled synthesis of gold and silver nanoparticles, Science 298 (5601) (2002) 2176–2179.

[145] J. Hang, X.-H. Yi, C.-C. Wang, H. Fu, P. Wang, Y. Zhao, Heterogeneous photo-Fenton degradation toward sulfonamide matrix over magnetic Fe_3S_4 derived from MIL-100(Fe), J. Hazard. Mater. 424 (2022), 127415.

[146] W. Ma, N. Wang, Y. Fan, T. Tong, X. Han, Y. Du, Non-radical-dominated catalytic degradation of bisphenol A by ZIF-67 derived nitrogen-doped carbon nanotubes frameworks in the presence of peroxymonosulfate, Chem. Eng. J. 336 (2018) 721–731.

[147] Y. Zhou, J. Jiang, Y. Gao, J. Ma, S.-Y. Pang, J. Li, X.-T. Lu, L.-P. Yuan, Activation of peroxymonosulfate by benzoquinone: a novel nonradical oxidation process, Environ. Sci. Technol. 49 (21) (2015) 12941–12950.

[148] Z. Zhu, C. Ji, L. Zhong, S. Liu, F. Cui, H. Sun, W. Wang, Magnetic Fe-Co crystal doped hierarchical porous carbon fibers for removal of organic pollutants, J. Mater. Chem. A 5 (34) (2017) 18071–18080.

[149] Y. Bao, W.-D. Oh, T.-T. Lim, R. Wang, R.D. Webster, X. Hu, Surface-nucleated heterogeneous growth of zeolitic imidazolate framework–A unique precursor towards catalytic ceramic membranes: synthesis, characterization and organics degradation, Chem. Eng. J. 353 (2018) 69–79.

[150] R. Fu, X. Wu, X. Wang, W. Ma, L. Yuan, L. Gao, K. Huang, S. Feng, Low-temperature hydrothermal fabrication of Fe_3O_4 nanostructured solar selective absorption films, Appl. Surf. Sci. 458 (2018) 629–637.

[151] Y. Chen, J.-F. Li, P.-Y. Liao, Y.-S. Zeng, Z. Wang, Z.-Q. Liu, Cascaded electron transition in $CuWO_4$/CdS/CDs heterostructure accelerating charge separation towards enhanced photocatalytic activity, Chin. Chem. Lett. 31 (2020) 1516–1519.

[152] T. Xu, J. Wang, Y. Cong, S. Jiang, Q. Zhang, H. Zhu, Y. Li, X. Li, Ternary BiOBr/TiO_2/$Ti_3C_2T_x$ MXene nanocomposites with heterojunction structure and improved photocatalysis performance, Chin. Chem. Lett. 31 (2020) 1022–1025.

[153] Z. Yu, L. Qian, T. Zhong, Q. Ran, J. Huang, Y. Hou, F. Li, M. Li, Q. Sun, H. Zhang, Enhanced visible light photocatalytic activity of CdS through controllable self-assembly compositing with ZIF-67, Mol. Catal. 485 (2020), 110797.

[154] M. Kohantorabi, M.R. Gholami, AgPt nanoparticles supported on magnetic graphene oxide nanosheets for catalytic reduction of 4-nitrophenol: studies of kinetics and mechanism, Appl. Organomet. Chem. 31 (11) (2017), e3806.

[155] K.C. Lai, L.Y. Lee, B.Y.Z. Hiew, S. Thangalazhy-Gopakumar, S. Gan, Environmental application of three-dimensional graphene materials as adsorbents for dyes and heavy metals: review on ice-templating method and adsorption mechanisms, J. Environ. Sci. 79 (2019) 174–199.

[156] S.-F. Zhang, H. Li, C. Hou, L.-N. Liu, Y. Wang, M.-K. Zhao, C. Liang, Recyclable ZIF-9@ CA-Fe_3O_4/RGO/cellulose composite membrane as efficient catalysts for activating peroxymonosulfate to degrade methylene blue, Cellulose 27 (6) (2020) 3287–3300.

[157] T. Wang, J. Zhou, W. Wang, Y. Zhu, J. Niu, Ag-single atoms modified $S_{1.66}$-$N_{1.91}$/$TiO_{2−x}$ for photocatalytic activation of peroxymonosulfate for bisphenol A degradation, Chin. Chem. Lett. (2021).

[158] J. Qiu, P. Zhang, M. Ling, S. Li, P. Liu, H. Zhao, S. Zhang, Photocatalytic synthesis of TiO_2 and reduced graphene oxide nanocomposite for lithium ion battery, ACS Appl. Mater. Interfaces 4 (7) (2012) 3636–3642.

[159] A.H.C. Khavar, G. Moussavi, A. Mahjoub, K. Yaghmaeian, V. Srivastava, M. Sillanpää, M. Satari, Novel magnetic Fe_3O_4/rGO@ZnO onion-like microspheres decorated with Ag nanoparticles for the efficient photocatalytic oxidation of metformin: toxicity evaluation and insights into the mechanisms, Catal. Sci. Technol. 9 (20) (2019) 5819–5837.

[160] J. Rodriguez-Chueca, S. Giannakis, M. Marjanovic, M. Kohantorabi, M. R. Gholami, D. Grandjean, L.F. de Alencastro, C. Pulgarin, Solar-assisted bacterial disinfection and removal of contaminants of emerging concern by Fe^{2+}-activated HSO_5^- vs. $S_2O_8^{2−}$ in drinking water, Appl. Catal. B Environ. 248 (2019) 62–72.

[161] M.-P. Zhu, J.-C.E. Yang, X. Duan, D.-D. Zhang, S. Wang, B. Yuan, M.-L. Fu, Interfacial $CoAl_2O_4$ from ZIF-67@γ-Al_2O_3 pellets toward catalytic activation of peroxymonosulfate for metronidazole removal, Chem. Eng. J. 397 (2020), 125339.

[162] Y.-X. Li, H. Fu, P. Wang, C. Zhao, W. Liu, C.-C. Wang, Porous tube-like ZnS derived from rod-like ZIF-L for photocatalytic Cr(VI) reduction and organic pollutants degradation, Environ. Pollut. 256 (2020), 113417.

[163] L. Wu, H. Fu, Q. Wei, Q. Zhao, P. Wang, C.-C. Wang, Porous $Cd_{0.5}Zn_{0.5}S$ nanocages derived from ZIF-8: boosted photocatalytic performances under LED-visible light, Environ. Sci. Pollut. Res. 28 (5) (2021) 5218–5230.

[164] H. Fu, L. Wu, J. Hang, P. Wang, C. Zhao, C.-C. Wang, Room-temperature preparation of MIL-68 and its derivative In_2S_3 for enhanced photocatalytic Cr(VI) reduction and organic pollutant degradation under visible light, J. Alloy. Compd. 837 (2020), 155567.

[165] Y.-X. Li, C.-C. Wang, H. Fu, P. Wang, Marigold-flower-like TiO_2/MIL-125 core−shell composite for enhanced photocatalytic Cr (VI) reduction, J. Environ. Eng. 9 (2021), 105451.

[166] Y.-X. Li, Y.-C. Han, C.-C. Wang, Fabrication strategies and Cr(VI) elimination activities of the MOF-derivatives and their composites, Chem. Eng. J. 405 (2021), 126648.

[167] C. Wang, J. Kim, V. Malgras, J. Na, J. Lin, J. You, M. Zhang, J. Li, Y. Yamauchi, Metal–organic frameworks and their derived materials: emerging catalysts for a sulfate radicals-based advanced oxidation process in water purification, Small 15 (16) (2019) 1900744.

[168] M.A.N. Khan, P.K. Klu, C. Wang, W. Zhang, R. Luo, M. Zhang, J. Qi, X. Sun, L. Wang, J. Li, Metal-organic framework-derived hollow Co_3O_4/carbon as efficient catalyst for peroxymonosulfate activation, Chem. Eng. J. 363 (2019) 234–246.

[169] D. Liu, M. Li, X. Li, F. Ren, P. Sun, L. Zhou, Core-shell Zn/Co MOFs derived Co_3O_4/CNTs as an efficient magnetic heterogeneous catalyst for persulfate activation and oxytetracycline degradation, Chem. Eng. J. 387 (2020) 124008.

[170] J. Zhao, F. Li, H. Wei, H. Ai, L. Gu, J. Chen, L. Zhang, M. Chi, J. Zhai, Superior performance of ZnCoOx/peroxymonosulfate system for organic pollutants removal by enhancing singlet oxygen generation: the effect of oxygen vacancies, Chem. Eng. J. 409 (2021), 128150.

[171] J. Ye, J. Dai, C. Li, Y. Yan, Lawn-like Co_3O_4@N-doped carbon-based catalytic self-cleaning membrane with peroxymonosulfate activation: a highly efficient singlet oxygen dominated process for sulfamethoxazole degradation, Chem. Eng. J. 421 (2021), 127805.

[172] M.-P. Zhu, J.-C.E. Yang, X. Duan, S. Wang, D.D. Sun, B. Yuan, M.-L. Fu, Engineered Co_2AlO_4/$CoAl_2O_4$@Al_2O_3 monolithic catalysts for peroxymonosulfate activation: Co^{3+}/Co^{2+} and ODefect/OLattice ratios dependence and mechanism, Chem. Eng. J. 433 (2022) 128162.

[173] L. Bai, J. Zhang, J. He, H. Zheng, Q. Yang, ZnO–Co_3O_4/N–C cage derived from hollow Zn/Co ZIF for enhanced degradation of Bisphenol A with persulfate, Inorg. Chem. 60 (2021) 3041–13050.

[174] X. Yang, X. Xie, S. Li, W. Zhang, X. Zhang, H. Chai, Y. Huang, The POM@MOF hybrid derived hierarchical hollow Mo/Co bimetal oxides nanocages for efficiently activating peroxymonosulfate to degrade levofloxacin, J. Hazard. Mater. 419 (2021), 126360.

[175] L. Bai, Z. Guan, S. Li, S. Zhang, Q. Huang, Z. Li, Nest-like Co_3O_4 and PdO_x/Co_3O_4 synthesized via metal organic framework with cyclodextrin for catalytic removal of Bisphenol A by persulfate, Sep. Purif. Technol. 255 (2021), 117718.

[176] X.-L. Chen, F. Li, M. Zhang, B. Liu, H. Chen, H. Wang, Highly dispersed and stabilized Co_3O_4/C anchored on porous biochar for bisphenol A degradation by sulfate radical advanced oxidation process, Sci. Total Environ. 777 (2021), 145794.

[177] X. Fang, L. Gan, L. Wang, H. Gong, L. Xu, Y. Wu, H. Lu, S. Han, J. Cui, C. Xia, Enhanced degradation of bisphenol A by mixed ZIF derived CoZn oxide encapsulated N-doped carbon via peroxymonosulfate activation: the importance of N doping amount, J. Hazard. Mater. 419 (2021), 126363.

[178] L. Zou, X. Zhu, L. Lu, Y. Xu, B. Chen, Bimetal organic framework/graphene oxide derived magnetic porous composite catalyst for peroxymonosulfate activation in fast organic pollutant degradation, J. Hazard. Mater. 419 (2021), 126427.

[179] N. Lu, H. Lin, G. Li, J. Wang, Q. Han, F. Liu, ZIF-67 derived nanofibrous catalytic membranes for ultrafast removal of antibiotics under flow-through filtration via non-radical dominated pathway, J. Membr. Sci. 639 (2021), 119782.

[180] L. Bai, J. He, L. Liu, Z. Guan, G. Wang, Tunable synthesis of cage-like Co_3O_4/N–C composite and nest-like Co_3O_4 for oxidative degradation of Bisphenol A, J. Solid State Chem. 304 (2021), 122550.

[181] Y. Liu, H. Zou, H. Ma, J. Ko, W. Sun, K. Andrew Lin, S. Zhan, H. Wang, Highly efficient activation of peroxymonosulfate by MOF-derived CoP/CoO_x heterostructured nanoparticles for the degradation of tetracycline, Chem. Eng. J. 430 (2022), 132816.

[182] Y. Chen, X. Bai, Y. Ji, T. Shen, Reduced graphene oxide-supported hollow Co_3O_4@N-doped porous carbon as peroxymonosulfate activator for sulfamethoxazole degradation, Chem. Eng. J. 430 (2022), 132951.

[183] J. Ye, D. Yang, J. Dai, C. Li, Y. Yan, Y. Wang, Strongly coupled cobalt/oxygen co-doped porous g-C_3N_4 heterostructure with abundant oxygen vacancies modulated the peroxymonosulfate activation pathway, Chem. Eng. J. 431 (2022), 133972.

[184] S. Zhang, X. Ren, X. Zhou, H. Gao, X. Wang, J. Huang, X. Xu, Hierarchical multi-active component yolk-shell nanoreactors as highly active peroxymonosulfate activator for ciprofloxacin degradation, J. Colloid Interface Sci. 605 (2022) 766–778.

[185] S. Wu, C. Yang, Y. Lin, J.J. Cheng, Efficient degradation of tetracycline by singlet oxygen-dominated peroxymonosulfate activation with magnetic nitrogen-doped porous carbon, J. Environ. Sci. 115 (2022) 330–340.

[186] J. Ye, D. Yang, J. Dai, C. Li, Y. Yan, Confinement of ultrafine Co_3O_4 nanoparticles in nitrogen-doped graphene-supported macroscopic microspheres for ultrafast catalytic oxidation: role of oxygen vacancy and ultrasmall size effect, Sep. Purif. Technol. 281 (2022), 119963.

[187] H. Li, J. Tian, Z. Zhu, F. Cui, Y.-A. Zhu, X. Duan, S. Wang, Magnetic nitrogen-doped nanocarbons for enhanced metal-free catalytic oxidation: integrated experimental and theoretical investigations for mechanism and application, Chem. Eng. J. 354 (2018) 507–516.

[188] Y. Liu, X. Chen, Y. Yang, Y. Feng, D. Wu, S. Mao, Activation of persulfate with metal–organic framework-derived nitrogen-doped porous Co@C nanoboxes for highly efficient p-Chloroaniline removal, Chem. Eng. J. 358 (2019) 408–418.

[189] M. Zhang, R. Luo, C. Wang, W. Zhang, X. Yan, X. Sun, L. Wang, J. Li, Confined pyrolysis of metal–organic frameworks to N-doped hierarchical carbon for non-radical dominated advanced oxidation processes, J. Mater. Chem. A 7 (20) (2019) 12547–12555.

[190] S. Zhang, H. Gao, X. Xu, R. Cao, H. Yang, X. Xu, J. Li, MOF-derived CoN/NC@SiO_2 yolk-shell nanoreactor with dual active sites for highly efficient catalytic advanced oxidation processes, Chem. Eng. J. 381 (2020), 122670.

[191] X. Li, X. Yan, X. Hu, R. Feng, M. Zhou, L. Wang, Hollow Cu-Co/N-doped carbon spheres derived from ZIFs as an efficient catalyst for peroxymonosulfate activation, Chem. Eng. J. 397 (2020), 125533.

[192] Y. Zhou, Y. Zhang, X. Hu, Novel zero-valent Co–Fe encapsulated in nitrogen-doped porous carbon nanocomposites derived from $CoFe_2O_4$@ ZIF-67 for boosting 4-chlorophenol removal via coupling peroxymonosulfate, J. Colloid Interface Sci. 575 (2020) 206–219.

[193] X. Li, X. Yan, X. Hu, R. Feng, M. Zhou, Yolk-shell ZIFs@SiO_2 and its derived carbon composite as robust catalyst for peroxymonosulfate activation, J. Environ. Manag. 262 (2020), 110299.

[194] J. Cao, Z. Yang, W. Xiong, Y. Zhou, Y. Wu, M. Jia, S. Sun, C. Zhou, Y. Zhang, R. Zhong, Peroxymonosulfate activation of magnetic Co nanoparticles relative to an N-doped porous carbon under confinement: Boosting stability and performance, Sep. Purif. Technol. 250 (2020), 117237.

[195] J. Ye, C. Li, Y. Yan, Core-shell ZIF-67/ZIF-8-derived sea urchin-like cobalt/nitrogen Co-doped carbon nanotube hollow frameworks for ultrahigh adsorption and catalytic activities, J. Taiwan Inst. Chem. Eng. 112 (2020) 202–211.

[196] H. Dai, W. Zhou, W. Wang, Co/N co-doped carbonaceous polyhedron as efficient peroxymonosulfate activator for degradation of organic pollutants: role of cobalt, Chem. Eng. J. 417 (2021), 127921.

[197] N. Liu, N. Lu, H. Yu, S. Chen, X. Quan, Degradation of aqueous bisphenol A in the CoCN/Vis/PMS system: catalyst design, reaction kinetic and mechanism analysis, Chem. Eng. J. 407 (2021), 127228.

[198] Y. Xue, N.N. Pham, G. Nam, J. Choi, Y.-Y. Ahn, H. Lee, J. Jung, S.-G. Lee, J. Lee, Persulfate activation by ZIF-67-derived cobalt/nitrogen-doped carbon composites: Kinetics and mechanisms dependent on persulfate precursor, Chem. Eng. J. 408 (2021), 127305.

[199] M. Zhang, C. Xiao, C. Zhang, J. Qi, C. Wang, X. Sun, L. Wang, Q. Xu, J. Li, Large-scale synthesis of biomass@MOF-derived porous carbon/cobalt nanofiber for environmental remediation by advanced oxidation processes, ACS EST Eng. 1 (2) (2020) 249–260.

[200] Y. Gao, Y. Zhu, Z. Chen, C. Hu, Nitrogen-coordinated cobalt embedded in a hollow carbon polyhedron for superior catalytic oxidation of organic contaminants with peroxymonosulfate, ACS EST Eng. 1 (1) (2020) 76–85.

[201] X. Yu, L. Wang, X. Wang, H. Liu, Z. Wang, Y. Huang, G. Shan, W. Wang, L. Zhu, Enhanced nonradical catalytic oxidation by encapsulating cobalt into nitrogen doped graphene: highlight on interfacial interactions, J. Mater. Chem. A 9 (11) (2021) 7198–7207.

[202] T. Zhang, Q. Ma, M. Zhou, C. Li, J. Sun, W. Shi, S. Ai, Degradation of methylene blue by a heterogeneous Fenton reaction catalyzed by FeCo$_2$O$_4$-NC nanocomposites derived from ZIFs, Powder Technol. 383 (2021) 212–219.

[203] Y. Zhou, X. Hu, Y. Zhang, X. Chen, H. Zhao, Q. Fu, F. Xu, Y. Gao, Enhanced oxidative degradation of 4-chlorophenol via peroxymonosulfate activated by Co$_3$Fe$_7$ and Co^0 embedded in N-doped porous carbons: pivotal role of nitrogen-vacancy, Appl. Surf. Sci. 566 (2021), 150657.

[204] D.D. Tuan, E. Kwon, S. Phattarapattamawong, B.X. Thanh, T.C. Khiem, G. Lisak, H. Wang, K.-Y.A. Lin, Nitrogen-containing carbon hollow nanocube-confined cobalt nanoparticle as a magnetic and efficient catalyst for activating monopersulfate to degrade a UV filter in water, J. Environ. Chem. Eng. 10 (2022), 106989.

[205] X. Zhang, X. Yan, X. Hu, R. Feng, M. Zhou, L. Wang, Efficient removal of organic pollutants by a Co/N/S-doped yolk-shell carbon catalyst via peroxymonosulfate activation, J. Hazard. Mater. 421 (2022), 126726.

[206] H. Dai, W. Zhou, W. Wang, Z. Liu, Unveiling the role of cobalt species in the Co/N-C catalysts-induced peroxymonosulfate activation process, J. Hazard. Mater. 426 (2022), 127784.

[207] Z. Wang, X. Wang, L. Wang, Y. Wei, Z. Zhao, K. Du, D. Chen, X. Li, C. Zhou, G. Liu, Y. Luo, ZIF-67-derived Co@N-PC anchored on tracheid skeleton from sawdust with micro/nano composite structures for boosted methylene blue degradation, Sep. Purif. Technol. 278 (2021) 119489.

[208] Y. Long, S. Li, P. Yang, X. Chen, W. Liu, X. Zhan, C. Xue, D. Liu, W. Huang, Synthesis of ZIF-67 derived honeycomb porous Co/NC catalyst for AO7 degradation via activation of peroxymonosulfate, Sep. Purif. Technol. 286 (2022) 120470.

[209] J. Xie, L. Chen, X. Luo, L. Huang, S. Li, X. Gong, Degradation of tetracycline hydrochloride through efficient peroxymonosulfate activation by B, N co-doped porous carbon materials derived from metal-organic frameworks: nonradical pathway mechanism, Sep. Purif. Technol. 281 (2022) 119887.

[210] Z. Wu, Z. Xiong, R. Liu, C. He, Y. Liu, Z. Pan, G. Yao, B. Lai, Pivotal roles of N-doped carbon shell and hollow structure in nanoreactor with spatial confined Co species in peroxymonosulfate activation: obstructing metal leaching and enhancing catalytic stability, J. Hazard. Mater. 427 (2022), 128204.

[211] C. Zhu, F. Liu, C. Ling, H. Jiang, H. Wu, A. Li, Growth of graphene-supported hollow cobalt sulfide nanocrystals via MOF-templated ligand exchange as surface-bound radical sinks for highly efficient bisphenol A degradation, Appl. Catal. B Environ. 242 (2019) 238–248.

[212] R.R. Salunkhe, Y.V. Kaneti, Y. Yamauchi, Metal–organic framework-derived nanoporous metal oxides toward supercapacitor applications: progress and prospects, ACS Nano 11 (6) (2017) 5293–5308.

[213] J. Hu, M. Chen, X. Fang, L. Wu, Fabrication and application of inorganic hollow spheres, Chem. Soc. Rev. 40 (11) (2011) 5472–5491.

[214] R. Bai, W. Yan, Y. Xiao, S. Wang, X. Tian, J. Li, X. Xiao, X. Lu, F. Zhao, Acceleration of peroxymonosulfate decomposition by a magnetic MoS$_2$/CuFe$_2$O$_4$ heterogeneous catalyst for rapid degradation of fluoxetine, Chem. Eng. J. 397 (2020), 125501.

[215] R. Yin, W. Guo, H. Wang, J. Du, X. Zhou, Q. Wu, H. Zheng, J. Chang, N. Ren, Selective degradation of sulfonamide antibiotics by peroxymonosulfate alone: direct oxidation and nonradical mechanisms, Chem. Eng. J. 334 (2018) 2539–2546.

[216] X. Chen, W.-D. Oh, T.-T. Lim, Graphene-and CNTs-based carbocatalysts in persulfates activation: material design and catalytic mechanisms, Chem. Eng. J. 354 (2018) 941–976.

[217] C. Schweitzer, R. Schmidt, Physical mechanisms of generation and deactivation of singlet oxygen, Chem. Rev. 103 (5) (2003) 1685–1758.

[218] H. Wang, S. Jiang, S. Chen, D. Li, X. Zhang, W. Shao, X. Sun, J. Xie, Z. Zhao, Q. Zhang, Enhanced singlet oxygen generation in oxidized graphitic carbon nitride for organic synthesis, Adv. Mater. 28 (32) (2016) 6940–6945.

[219] L. Wu, Y. Yu, Q. Zhang, J. Hong, J. Wang, Y. She, A novel magnetic heterogeneous catalyst oxygen-defective CoFe$_2$O$_{4-x}$ for activating peroxymonosulfate, Appl. Surf. Sci. 480 (2019) 717–726.

[220] P.-H. Li, Z.-Y. Song, M. Yang, S.-H. Chen, X.-Y. Xiao, W. Duan, L.-N. Li, X.-J. Huang, Electrons in oxygen vacancies and oxygen atoms activated by Ce^{3+}/Ce^{4+} promote high-sensitive electrochemical detection of Pb(II) over ce-doped α-MoO$_3$ catalysts, Anal. Chem. 92 (24) (2020) 16089–16096.

[221] J. Wang, T. Liao, Z. Wei, J. Sun, J. Guo, Z. Sun, Heteroatom-doping of non-noble metal-based catalysts for electrocatalytic hydrogen evolution: an electronic structure tuning strategy, Small Methods 5 (4) (2021) 2000988.

[222] G. Fang, J. Zhou, Y. Cai, S. Liu, X. Tan, A. Pan, S. Liang, Metal–organic framework-templated two-dimensional hybrid bimetallic metal oxides with enhanced lithium/sodium storage capability, J. Mater. Chem. A 5 (27) (2017) 13983–13993.

[223] T. Ling, P. Da, X. Zheng, B. Ge, Z. Hu, M. Wu, X.-W. Du, W.-B. Hu, M. Jaroniec, S.-Z. Qiao, Atomic-level structure engineering of metal oxides for high-rate oxygen intercalation pseudocapacitance, Sci. Adv. 4 (10) (2018) eaau6261.

[224] W. Ren, C. Cheng, P. Shao, X. Luo, H. Zhang, S. Wang, X. Duan, Origins of electron-transfer regime in persulfate-based nonradical oxidation processes, Environ. Sci. 56 (2022) 78–97.

[225] X. Duan, H. Sun, Z. Shao, S. Wang, Nonradical reactions in environmental remediation processes: uncertainty and challenges, Appl. Catal. B Environ. 224 (2018) 973–982.

[226] Y. Zhao, X. Yuan, X. Li, L. Jiang, H. Wang, Burgeoning prospects of biochar and its composite in persulfate-advanced oxidation process, J. Hazard. Mater. 409 (2021), 124893.

[227] Y.-Y. Ahn, H. Bae, H.-I. Kim, S.-H. Kim, J.-H. Kim, S.-G. Lee, J. Lee, Surface-loaded metal nanoparticles for peroxymonosulfate activation: efficiency and mechanism reconnaissance, Appl. Catal. B Environ. 241 (2019) 561–569.

[228] S. Zhu, X. Huang, F. Ma, L. Wang, X. Duan, S. Wang, Catalytic removal of aqueous contaminants on N-doped graphitic biochars: inherent roles of adsorption and nonradical mechanisms, Environ. Sci. Technol. 52 (15) (2018) 8649–8658.

[229] J. Du, J. Bao, Y. Liu, H. Ling, H. Zheng, S.H. Kim, D.D. Dionysiou, Efficient activation of peroxymonosulfate by magnetic Mn-MGO for degradation of bisphenol A, J. Hazard. Mater. 320 (2016) 150–159.

[230] X. Duan, Z. Ao, L. Zhou, H. Sun, G. Wang, S. Wang, Occurrence of radical and nonradical pathways from carbocatalysts for aqueous and nonaqueous catalytic oxidation, Appl. Catal. B Environ. 188 (2016) 98–105.

[231] H. Lee, H.-i Kim, S. Weon, W. Choi, Y.S. Hwang, J. Seo, C. Lee, J.-H. Kim, Activation of persulfates by graphitized nanodiamonds for removal of organic compounds, Environ. Sci. Technol. 50 (18) (2016) 10134–10142.

[232] S. Yanan, X. Xing, Q. Yue, B. Gao, Y. Li, Nitrogen-doped carbon nanotubes encapsulating Fe/Zn nanoparticles as a persulfate activator for sulfamethoxazole degradation: role of encapsulated bimetallic nanoparticles and nonradical reaction, Environ. Sci. Nano 7 (5) (2020) 1444–1453.

[233] Y. Zhao, X. Yuan, X. Li, L. Jiang, H. Wang, Burgeoning prospects of biochar and its composite in persulfate-advanced oxidation process, J. Hazard. Mater. 409 (2021), 124893.

[234] X. Xu, J. Qin, Y. Wei, S. Ye, J. Shen, Y. Yao, B. Ding, Y. Shu, G. He, H. Chen, Heterogeneous activation of persulfate by NiFe$_{2-x}$Co$_x$O$_4$-RGO for oxidative degradation of bisphenol A in water, Chem. Eng. J. 365 (2019) 259–269.

[235] Y. Shang, X. Duan, S. Wang, Q. Yue, B. Gao, X. Xu, Carbon-based single atom catalyst: synthesis, characterization, DFT calculations, Chin. Chem. Lett. 33 (2) (2022) 663–673.

[236] J. Peng, Y. He, C. Zhou, S. Su, B. Lai, The carbon nanotubes-based materials and their applications for organic pollutant removal: a critical review, Chin. Chem. Lett. 32 (2021) 1626–1636.

[237] W. Huang, S. Xiao, H. Zhong, M. Yan, X. Yang, Activation of persulfate by carbonaceous materials: a review, Chem. Eng. J. 418 (2021), 129297.

[238] X. Cheng, H. Guo, Y. Zhang, X. Wu, Y. Liu, Non-photochemical production of singlet oxygen via activation of persulfate by carbon nanotubes, Water Res. 113 (2017) 80–88.

[239] J.-C.E. Yang, M.-P. Zhu, D.D. Dionysiou, B. Yuan, M.-L. Fu, Interplay of bicarbonate and the oxygen-containing groups of carbon nanotubes dominated the metal-free activation of peroxymonosulfate, Chem. Eng. J. 430 (2022), 133102.

[240] X. Duan, H. Sun, Y. Wang, J. Kang, S. Wang, N-doping-induced nonradical reaction on single-walled carbon nanotubes for catalytic phenol oxidation, ACS Catal. 5 (2) (2015) 553–559.

[241] Z. Wang, S. Xiao, Z. Zhu, X. Long, X. Zheng, X. Lu, S. Yang, Cobalt-embedded nitrogen doped carbon nanotubes: a bifunctional catalyst for oxygen electrode reactions in a wide pH range, ACS Appl. Mater. Interfaces 7 (7) (2015) 4048–4055.

[242] Y. Yao, C. Lian, G. Wu, Y. Hu, F. Wei, M. Yu, S. Wang, Synthesis of "sea urchin"-like carbon nanotubes/porous carbon superstructures derived from waste biomass for treatment of various contaminants, Appl. Catal. B Environ. 219 (2017) 563–571.

[243] X. Duan, Z. Ao, H. Sun, L. Zhou, G. Wang, S. Wang, Insights into N-doping in single-walled carbon nanotubes for enhanced activation of superoxides: a mechanistic study, Chem. Commun. 51 (83) (2015) 15249–15252.

[244] C. Galeano, C. Baldizzone, H. Bongard, B. Spliethoff, C. Weidenthaler, J.C. Meier, K.J. Mayrhofer, F. Schüth, Carbon-based yolk–shell materials for fuel cell applications, Adv. Funct. Mater. 24 (2) (2014) 220–232.

[245] M.B. Gawande, A. Goswami, T. Asefa, H. Guo, A.V. Biradar, D.-L. Peng, R. Zboril, R.S. Varma, Core–shell nanoparticles: synthesis and applications in catalysis and electrocatalysis, Chem. Soc. Rev. 44 (21) (2015) 7540–7590.

[246] H. Tian, F. Huang, Y. Zhu, S. Liu, Y. Han, M. Jaroniec, Q. Yang, H. Liu, G.Q.M. Lu, J. Liu, The development of yolk–shell-structured Pd&ZnO@Carbon submicroreactors with high selectivity and stability, Adv. Funct. Mater. 28 (32) (2018) 1801737.

[247] Q. Yue, J. Li, Y. Zhang, X. Cheng, X. Chen, P. Pan, J. Su, A.A. Elzatahry, A. Alghamdi, Y. Deng, Plasmolysis-inspired nanoengineering of functional yolk–shell microspheres with magnetic core and mesoporous silica shell, J. Am. Chem. Soc. 139 (43) (2017) 15486–15493.

[248] K. Luo, Y. Pang, Q. Yang, D. Wang, X. Li, L. Wang, M. Lei, J. Liu, Enhanced ciprofloxacin removal by sludge-derived biochar: effect of humic acid, Chemosphere 231 (2019) 495–501.

[249] T. Zeng, X. Zhang, S. Wang, H. Niu, Y. Cai, Spatial confinement of a Co$_3$O$_4$ catalyst in hollow metal–organic frameworks as a nanoreactor for improved

degradation of organic pollutants, Environ. Sci. Technol. 49 (4) (2015) 2350–2357.

[250] T. Chen, Z. Zhang, B. Cheng, R. Chen, Y. Hu, L. Ma, G. Zhu, J. Liu, Z. Jin, Self-templated formation of interlaced carbon nanotubes threaded hollow Co_3S_4 nanoboxes for high-rate and heat-resistant lithium–sulfur batteries, J. Am. Chem. Soc. 139 (36) (2017) 12710–12715.

[251] Y. Guo, J. Tang, H. Qian, Z. Wang, Y. Yamauchi, One-pot synthesis of zeolitic imidazolate framework 67-derived hollow Co_3S_4@MoS_2 heterostructures as efficient bifunctional catalysts, Chem. Mater. 29 (13) (2017) 5566–5573.

[252] Q. Zhou, L. Liu, Z. Huang, L. Yi, X. Wang, G. Cao, Co_3S_4@polyaniline nanotubes as high-performance anode materials for sodium ion batteries, J. Mater. Chem. A 4 (15) (2016) 5505–5516.

[253] Y. Liu, H. Wang, X. Yuan, Y. Wu, H. Wang, Y.Z. Tan, J.W. Chew, Roles of sulfur-edge sites, metal-edge sites, terrace sites, and defects in metal sulfides for photocatalysis, Chem. Catal. 1 (2021) 44–68.

[254] Z.-F. Huang, J. Song, K. Li, M. Tahir, Y.-T. Wang, L. Pan, L. Wang, X. Zhang, J.-J. Zou, Hollow cobalt-based bimetallic sulfide polyhedra for efficient all-pH-value electrochemical and photocatalytic hydrogen evolution, J. Am. Chem. Soc. 138 (4) (2016) 1359–1365.

[255] Y. Gu, Y. Xu, Y. Wang, Graphene-wrapped CoS nanoparticles for high-capacity lithium-ion storage, ACS Appl. Mater. Interfaces 5 (3) (2013) 801–806.

[256] H. Sun, Y. Wang, S. Liu, L. Ge, L. Wang, Z. Zhu, S. Wang, Facile synthesis of nitrogen doped reduced graphene oxide as a superior metal-free catalyst for oxidation, Chem. Commun. 49 (2013) 9914–9916.

[257] Y. Zhao, Q. Pang, Y. Meng, Y. Gao, C. Wang, B. Liu, Y. Wei, F. Du, G. Chen, Self-assembled CoS nanoflowers wrapped in reduced graphene oxides as the high-performance anode materials for sodium-ion batteries, Chem. Eur. J. 23 (53) (2017) 13150–13157.

[258] X. Wang, Y. Qin, L. Zhu, H. Tang, Nitrogen-doped reduced graphene oxide as a bifunctional material for removing bisphenols: synergistic effect between adsorption and catalysis, Environ. Sci. Technol. 49 (11) (2015) 6855–6864.

[259] C. Wang, P. Shi, X. Cai, Q. Xu, X. Zhou, X. Zhou, D. Yang, J. Fan, Y. Min, H. Ge, Synergistic effect of Co_3O_4 nanoparticles and graphene as catalysts for peroxymonosulfate-based orange II degradation with high oxidant utilization efficiency, J. Phys. Chem. C 120 (1) (2016) 336–344.